

H²⁰¹⁹-SPACE

5th INTERNATIONAL CONFERENCE
ON RESEARCH, TECHNOLOGY AND EDUCATION OF SPACE

**Selected papers of
5th International Conference on Research,
Technology and Education of Space**

February 27-28, 2019, Budapest, Hungary
at Budapest University of Technology and Economics

Organized by
Federated Innovation and Knowledge Centre of
Budapest University of Technology and Economics
and
Hungarian Astronautical Society

Editors
László Bacsárdi and Kálmán Kovács

MANT 2019

Selected papers of the 5th International Conference on Research, Technology and Education of Space (H-SPACE2018)

February 27-28, 2019, Budapest, Hungary

Building 'K' and Building 'I'

Budapest University of Technology and Economics

Műegyetem rkp. 3., Budapest, H-1111, Hungary

BME building 'I', Hall IB 026

Magyar tudósok krt. 2., Budapest, H-1117 Hungary

Organizing and Editorial Board

Chair: Dr. Kálmán Kovács

Co-Chair: Dr. László Bacsárdi

Members:

Prof. József Ádám

Dr. Tibor Bálint

Ferenc Horvai

Dr. Lóránt Földváry

Prof. János Lichtenberger

Prof. László Pap

Prof. Gábor Stépán,

Dr. Szabolcs Rózsa

Honorable Patrons:

Prof. Iván Almár, Prof. János Józsa, Prof. László Jakab

Created by the support of BME VIK, BME EIT and MANT.

Editors: László Bacsárdi and Kálmán Kovács

Publisher (Kiadó):

Hungarian Astronautical Society (MANT, Magyar Asztronautikai Társaság)

1044 Budapest, Ipari park u. 10.

www.mant.hu

Budapest, 2019

Responsible publisher: Dr. Attila Hirn, Secretary General

This proceedings contains the papers as it was submitted by their authors. We have not edited their text or corrected misspellings.

© All rights reserved

ISBN 978-963-7367-19-9

WELCOME from the Organizing Committee

In 2019, the annual International Conference on Research, Technology and Education of Space has been held the 5th time. The host was the BME Space Forum operated by the Federated Innovation and Knowledge Centre (EIT) of the Faculty of Electrical Engineering and Informatics at the Budapest University of Technology and Economics (BME) – in cooperation with the Hungarian Astronautical Society (MANT), which is the oldest space association in Hungary.

The Federated Innovation and Knowledge Centre (BME EIT) was created at the Faculty of Electrical Engineering and Informatics of Budapest University of Technology and Economics (BME) in 2009 to stimulate the research and development activity and to assist the exploitation of research achievements at the Faculty. Currently, BME EIT operates the BME Space Forum which mission is to harmonize and coordinate the activity of departments at BME participating in space activities by a common vision and strategy, to recognize the joint human and technical resources and amazing achievements, to make internal and external knowledge transfer more efficient, and to utilize opportunities lying in synergies granted by joint capabilities and unified representation. The common aim of BME Space Forum members is to become the bridge between academic research and production, service application, and to participate all phases of research/development/innovation and application processes of space activity. Currently, 13 Departments of 4 BME Faculties participate voluntarily in the activities of Space Forum.

The Hungarian Astronautical Society (MANT in Hungarian) is a civil organization in Hungary that gathers space researchers, users of space technology and everyone who is interested in the interdisciplinary and state-of-the-art uses and research of outer space. The society was established in 1956 in Budapest, and it is the only Hungarian member of the International Astronautical Federation (IAF) since 1959. The aim of MANT is to raise public awareness about space activity and space applications. The society also provides an opportunity for space enthusiasts to meet, exchange ideas and work together. MANT, through its members from various fields of science, organizes conferences, youth forums, summer space camps, issues periodicals, releases media material and holds lectures about space research and connected scientific fields.

The organization of the H-SPACE conference series started in 2015, at a time of growing opportunities arising from ESA recently granting membership to Hungary and the need for a joint presentation of space activities pursued at BME. The selection of the date of the event pays tribute to the successful deployment to orbit and mission of the first Hungarian satellite, the Masat-1, which has been launched on February 13, 2012.

This year people all over the world celebrate the greatest “small step for a man”, the 50th anniversary of the step of the first men onto the lunar surface. Humanity have explored the possibilities of life on other planets from that time, but from a very long time ago the essential conditions for life on Earth. Regarding to this, topic of this year’s conference is “Special focus on water and environment”. The agenda of the conference addressed scientific, technological and educational issues of space research and space activities.

The conference was open for both local and international professionals and provides an opportunity to showcase Hungarian scientific, technological, educational and outreach activities, related to space. Due to the generous support of our partners, the conference had no registration fee. The conference had five main sections: Science and Technology I-III and Education and Outreach I and II from which Science and Technology III and Education and Outreach II will be a poster session with 14 great presentation. We celebrated the 5th edition of the H-SPACE conference series with a special poster session which started right after the keynote presentation, held by Prof. János Józsa, the rector of the Budapest University of Technology and Economics.

To celebrate the 50th anniversary of the Moon landing, we started the conference with a special roundtable discussion: From Moon landing to Mars landing (in Hungarian). Participants of the discussions were Iván Almár (Honorary President, Hungarian Astronautical Society) and András Sik (Vice President, Hungarian Astronautical Society), and it was moderated by Előd Both (President, Hungarian Astronautical Society).

The Organizing Committee has internationally recognized members: Prof. József Ádám, Dr. Tibor Bálint, Ferenc Horvai, Prof. János Lichtenberger, Dr. Lóránt Földváry, Prof. László Pap, Prof. Gábor Stépán, Dr. Szabolcs Rózsa We are grateful for their contributions to the success of the conference.

We published a book of abstracts for the conference. During the conference, we had 2 keynote lecture and 34 technical presentations (20 oral presentations and 14 poster presentations) from which 13 authors have submitted a full paper. These papers are included in this proceedings.



Dr. Kálmán Kovács
chair
Director of EIT BME



Dr. László Bacsárdi
co-chair
Vice President of MANT

Final Conference Program

February 27-28, 2019
Budapest, Hungary

In this list, the affiliation of the first author is listed.

February 27, Wednesday

Location: Building K, first floor, Saloon room

Műgyetem rakpart 3., Budapest, H-1111, Building K, first floor, "Díszterem"

14:00 Greetings

László Bacsárdi, Vice President of MANT, co-chair of the Organizing Committee

14:05 Discussion: From Moon landing to Mars landing (*in Hungarian*)

Participants:

Iván Almár, Honorary President, Hungarian Astronautical Society

András Sik, Vice President, Hungarian Astronautical Society

Moderator:

Előd Both, President, Hungarian Astronautical Society

Session Chair: Kálmán Kovács

15:00 Opening ceremony

János Józsa, Rector, Budapest University of Technology and Economics

Orsolya Ferencz, Ministerial Commissioner, Ministry of Foreign Affairs and Trade

Előd Both, President, Hungarian Astronautical Society

Kálmán Kovács, President, BME Space Forum

15:15 Keynote presentation

On the Hydrologic Impacts of Climate Change

János Józsa, Rector, Budapest University of Technology and Economics

15:40 One minute madness (Session Science and Technology III and Education and Outreach II)

Poster authors presents their work in 1 minute

16:00 Poster session with coffee break

16:45-18:30: Technical presentations – Session Science and Technology I

Radio interferometry for the study of Jupiter's icy moons

Sándor Frey

Konkoly Observatory, MTA Research Centre for Astronomy and Earth Sciences, Hungary

Determination of 3D surface deformation for the 2018 Oaxaca earthquake using INSAR

Gergely László and Lóránt Földváry

Institute of Geoinformatics, Alba Regia Technical Faculty, Óbuda University, Hungary

ESA perspective on lunar surface exploration

Mátyás Hazadi

European Space Agency, The Netherlands

Satellite Fading Classification with Artificial Intelligence for 5G

Boldizsár Márton and László Csurgai-Horváth

Department of Broadband Infocommunications and Electromagnetic Theory, BME, Hungary

Investigation of stochastic disturbances in satellite connected terrestrial millimetre wave wireless mesh network

János Bitó

Department of Broadband Infocommunications and Electromagnetic Theory, BME, Hungary

Quantum Tracking a Dataset – a New Application of Quantum Cryptography

Máté Galambos and László Bacsárdi

Dennis Gabor College, Hungary

The RADCUBE project and beyond - Cosmic Radiation Monitoring CubeSat mission

Dorottya Milánkovich, Zoltán Kovács, Gábor Marosy and Balázs Zábori

C3S Ltd., Hungary

February 28, 2019, Thursday

Location: Building I, ground floor, IB.026.

Magyar tudósok krt. 2., Budapest, H-1117, Building I, ground floor

9:00 Welcome coffee

Session Chair: László Csurgai-Horváth

9:45 Keynote presentation

Recent dosimeter developments for human spaceflight at the Centre for Energy Research, Hungarian Academy of Sciences

Attila Hirn, Centre for Energy Research, Hungarian Academy of Sciences, Hungary

10:05-11:35 Technical presentations – Session Science and Technology II

UV Spectrophotometric Time Series Analysis of the Herbig Ae Star HD 163296

Gerard M. Williger, Anna Vankó, Péter Ábrahám, Carol A. Grady and Ágnes Kóspál
University of Louisville, KY, USA

Studying the MART tomography approach under severe weather conditions

Yuxiang Yan, Wusheng Hu, Juni Ildikó and Szabolcs Rózsa
School of Transportation, Southeast University in China, China

Transmission rates of lightning discharges into whistlers

Dávid Koronczay, János Lichtenberger and Orsolya Ferencz
Eötvös University, Hungary

Exploitation of Sentinel-1 SAR data for studying geodynamic, tropospheric and ionospheric processes

István Bozsó, Eszter Szűcs, László Bányai and Viktor Wesztergom
Geodetic and Geophysical Institute, MTA Research Centre for Astronomy and Earth Sciences,
Hungary

A wide swath of Sentinel-based deformation monitoring applications in Hungary

Péter Farkas, Gyula Grenerczy and Sándor Frey
Geo-Sentinel Ltd., Hungary

Developing Balloon-Borne Payload for Remote Sensing Applications

Zsófia Bodó and Bence Góczán
Simonyi Károly College for Advance Studies, BME, Hungary

11:35- 11:50 Break

11:50-11:55: Opening of the Education and Outreach Session

László Jakab, Dean, Faculty of Electrical Engineering and Informatics, BME

11:55-13:40: Technical presentations – Session Education and Outreach I

CoderDojo and the emergence of informal space tech education ecosystems

Radu Ticiu, Andrea Magyar and Virgiliu Pop

CoderDojo Timisoara, Romania

The Watermill-Project for Secondary Schools

Carmen Adina Oancea and Otilia Bogdana Lastun

Colegiul National “Octavian Goga” Sibiu, Romania

Inspiring the Next Generation in the Hungarian Space Camp

Dorottya Milánkovich and László Bacsárdi

Hungarian Astronautical Society, Hungary

The technology of CanSats, which can involve secondary school students in space

András Illyés, Levente Dudás and András Gschwindt

Budapest University of Technology and Economics, Hungary

The popularization of space exploration amongst high school students

Ténia Kovács, Annamária Komáromi and Andrea Király

Eötvös Loránd University, Hungary

The MarsQuake Program for Hungarian High School Students

Márta Kiszely and György Hudoba

Geodetic and Geophysical Institute, MTA Research Centre for Astronomy and Earth Sciences, Hungary

Space weather and Arduino meteo station

Mária Pető

Székely Mikó High School Sf. Gheorghe, Romania

13:40 Closing remarks

Poster presentations (Session Science and Technology III; Session Education and Outreach II, February 27 and February 28)

Building the First Hungarian Free-space Quantum Communication Device

Máté Galambos, László Baczárdi, Zoltán Belső, Eszter Gerhátné Udvary, Győző Gódor, Sándor Imre, Zsolt Kis, István Koller, János Kornis, Zsolt Papp and Viktor Zsolczai
Budapest University of Technology and Economics, Hungary

Detection of Tsunamis based on Ionospheric Satellite Signals

Gergely Mindler, Márk György Fék and Bence Szendi
Hungary

Educational Aspects of Developing a High Altitude Balloon Platform

Zsófia Bodó and Bence Góczán
Simonyi Károly College for Advance Studies, BME, Hungary

Estimating 3D Rain Fields with Satellite Beacon Measurements

Bernard Adjei-Frimpong and László Csurgai-Horváth
Department of Broadband Infocommunications and Electromagnetic Theory, BME, Hungary

Evaluation of plasma properties from ground measurements for radiation belts modeling

Lilla Juhász, Yoshiharu Omura, János Lichtenberger and Reinhard H. Friedel
Eötvös Loránd University, Hungary

Neutron transport simulations in lunar surface regolith

Szabolcs Nagy and Dávid Lucsányi
Puli Space Technologies Ltd., Hungary

Popularizing space-related activities in the Z-generation

Ákos Gyenge and Donát Takács
BME Cosmos Society, Budapest University of Technology and Economics, Hungary

Simulated Mars Rover Model Competition – 2018 and 2019 back to the MARS

Attila Sipos and Pál Gábor Vizi
magyarokamarson.hu, Hungary

Simulating the effects of solar particle radiation on serum immunoglobulin N-GLYCANS by capillary electrophoresis analysis

András Guttman, Máté Szarka, Szabolcs Szilasi, Dániel Sárközy, Boglárka Dönczö and István Rajta
Horváth Csaba Laboratory of Bioseparation Sciences, University of Debrecen, Hungary

Small steps towards strengthening the competitiveness in space research and technology - Space-related Education Initiative for Hungary

Andrea Strádi, László Baczárdi, András Ordasi, András Illyés, Zsófia Bodó and Dániel Szendrei
Hungarian Astronautical Society, Hungary

Streaming Swarms as Inter-Station and Interplanetary Transfer Pipes

Pál Gábor Vizi

Wigner Research Centre for Physics, HAS, Hungary, Hungary

Thermal simulations and analysis of a lunar surface payload

Bars Palfi, Dávid Lucsányi and Csaba Jeger

Puli Space Technologies Ltd., Hungary

UltimaSpace Experiments on the ISS

Flórián Vámosi and Péter Pósa Mihály Táncsics Grammar School of Kaposvár

Hungary

Why Astrophotography is the Best Promotion for Space Exploration and Astronomy?

Péter Feltóti, László Francsics and Flórián Vámosi

Hungarian Astrophotographers' Association, Hungary

Content

We have published a separate book of abstracts which contains all of the abstracts accepted for the conference. During the conference, we had 2 keynote lectures and 34 technical presentations from which 13 authors have submitted a full paper. These papers are included in this proceedings as it was submitted by their authors. We have not edited their text or corrected misspellings.

Bernard Adjei-Frimpong and László Csurgai-Horváth, *“Estimating 3D Rain Fields with Satellite Beacon Measurements”*

HSPACE2019-FP-3

Gergely László and Lóránt Földvály, *“Determination of 3D surface deformation for the 2018 Oaxaca earthquake using InSAR”*

HSPACE2019-FP-18

Márta Kiszely and György Hudoba, *“The MarsQuake Program for Hungarian High School Students”*

HSPACE2019-FP-22

Gergely Mindler, Márk György Fék and Bence Szendi, *“Detection of Tsunamis based on Ionospheric Satellite Signals”*

HSPACE2019-FP-23

Máté Galambos and László Bacsárdi, *“Quantum Tracking a Dataset – a New Application of Quantum Cryptography”*

HSPACE2019-FP-25

István Bozsó, Eszter Szűcs, László Bányai and Viktor Wesztergom, *“Exploitation of Sentinel-1 SAR data for studying geodynamic, tropospheric and ionospheric processes”*

HSPACE2019-FP-28

János Z. Bitó, *“Investigation of stochastic disturbances in satellite connected terrestrial millimetre wave wireless mesh network”*

HSPACE2019-FP-29

Ténia Kovács, Annamária Komáromi and Andrea Király, *“The popularization of space exploration amongst high school students”*

HSPACE2019-FP-30

Boldizsár Márton and László Csurgai-Horváth, “*Satellite Fading Classification with Artificial Intelligence for 5G*”

HSPACE2019-FP-31

Flórián Vámosi and Péter Pósa, “*UltimaSpace Experiments on the ISS*”

HSPACE2019-FP-32

Zsófia Bodó and Bence Góczán, “*Developing Balloon-Borne Payload for Remote Sensing Applications*”

HSPACE2019-FP-33

András Illyés, Levente Dudás and András Gschwindt, “*The technology of CanSats, which can involve secondary school students in space*”

HSPACE2019-FP-39

Zsófia Bodó and Bence Góczán, “*Educational Aspects of Developing a High Altitude Balloon Platform*”

HSPACE2019-FP-40

Estimating 3D Rain Fields with Satellite Beacon Measurements

Bernard Adjei-Frimpong

Budapest University of Technology and Economics
Department of Broadband Infocommunications and
Electromagnetic Theory, (BME-HVT)
Budapest, Hungary
bernard.frimpong@hvt.bme.hu

Laszlo Csurgai-Horvath

Budapest University of Technology and Economics
Department of Broadband Infocommunications and
Electromagnetic Theory, (BME-HVT)
Budapest, Hungary
laszlo.csurgai@hvt.bme.hu

Abstract—In the Department of Broadband Infocommunications and Electromagnetic Theory (HVT) at Budapest University of Technology and Economics, we participate in the Alphasat scientific experimentation program, where propagation and communication measurement activities take place. The propagation measurement is carried out in Ka/Q frequency bands to determine the atmospheric impact on radio wave propagation and the estimation of different statistical distributions, while the communication experiment in the Q/V band is used for diversity and Adaptive Coding and Modulation (ACM) studies. The wave propagation from the Alphasat were measured and discussed from a practical point of view, taking advantage of the availability of measurements from various instruments. The results showed that predictions can be calculated with reasonable accuracy, provided that some practical considerations are taken into account.

In view of this, we are proposing a novel idea based on signal beacon method to be used in satellite propagation measurement to estimate rain field dimensions and the shape of the cloud. Alphasat and other communication satellites are equipped with beacon transmitters with unmodulated signals for technological measurements. By receiving these signals from the satellite at three different geographical locations, we obtain the attenuation and the measurement is used to calculate rain intensity along the radio path, and from this, we can estimate the shape of the clouds in three dimensional state. This work is part of an ongoing activity, to calculate the shape of the clouds using satellite beacon signal measurements and constructing the image in 3D models of the rain fields by selection of three different attenuation events to determine the rain fields. Upon calculation we determine the interaction of geometrical links of the representations in the rain field in 3D model.

Keywords—rainCell; millimeter wave; radiowave; propagation

I. INTRODUCTION

Evolution of new telecommunication system for 5G systems are being developed in order to provide effective multimedia

applications to the end-user in the coming years. These applications require high data rates, large bandwidths which are available only for frequencies higher than 10 GHz. However, systems operating at these high frequencies suffer from severe atmospheric impairment such as attenuation and scintillation, which cannot be overcome by static propagation margins due to technology limitations [1]. However, increasing demand for large bandwidth is now moving toward the employment of high operational frequencies. Some advantages from using these higher frequencies in the millimeter wave range is smaller and lighter terminals, reduced channel congestion, limited interference issues, while the drawbacks come from the increasing effects induced by atmospheric constituents, mainly by rain, on electromagnetic waves [2].

There are different methods that is employed to study satellite wave propagation, this include radar, radiometer and signal beacon method. This signal beacon method is one of the most important, reliable and inexpensive method in comparison with the other methods. Satellite beacon has a reference signal with a fixed frequency and power, and without modulation that is sent usually by satellites. This signal usually has its own specific transponder with telemetry satellite signal. Satellite beacon receiver has to locate the beacon signals and measure its power level.

The description of the horizontal structure of rain fields is very complex, due to its high space-time variability. This explains the empirical-statistical nature of most studies performed, where research groups have developed rain-cell models from weather-radar data. The area inside which the rain rate $R \geq \tau$, τ being a rain rate threshold is known as the rain cell. The continuous cells, along the contour that bounds it, the rain rate is equal to the threshold value τ . A rain-cell characterization can be done using only a limited number of parameters. It is quite simple and less sophisticated in techniques, thereby reducing the computation time and the storage space necessary for extracting model parameters from the radar observations. In most studies, the mathematical representation of rain cells is based on stochastic approach, which describes rain cells as randomly generated entities that behave similarly in a statistical sense to the observed rain cells[3].

In this paper we have proposed the signal beacon method by extension determine the shape of the rain cloud through a rain cellular representation. In this process, the choice of this

model is highly applicable, because it accounts for the rain cell shape and the rain rate horizontal distribution within the cells. Rain cell shape can be used to describe an equivalent ellipse, whose parameters are the major axis, the minor axis, and the orientation angle. The rain rate horizontal distribution within the cells, have been divided into two different rain cell population groups: the stratiform cells, characterized by a slow decay of the rain rate from its maximum, and convective cells, which generates a cloudy area that can produce heavy rain with intensities higher than 10 mm/h [4].

The rationale of this proposal is that, in the absence of expensive equipment using the beacon signal, we can have applied the model based on the receivers at three different locations to determine the shape of rain cloud structure in a 3D state.

The organization of this paper is as follows. Section II, gives general overview of the satellite beacon, the measurement and the models for the prediction of the shape of the cloud. Section III describes cloud formation from the propagation in the millimeter wave and, the method applied to predict the shape. It also analyzes the prediction results of the proposed method, and section IV describes the cloud shape in the three dimensional state. Finally, section V concludes the paper.

II. SATELLITE BEACON AND MEASUREMENT SYSTEM

A. Satellite beacon

A device with low power transmission for the purpose up-link power control, telemetry and research is called satellite beacon. These signals are generally unmodulated but it can also be modulated. The attraction of satellite beacons for propagation research is their constant signal strength [5]. The main purpose of the radio beacon is making it easier to locate and also receive signals from the satellite above the horizon. However, some natural phenomena occur in the propagation path between the satellite and the ground station. These phenomena include cloud, rain, water vapor, dust, atmospheric gases, oxygen molecules and fog existing in different layers of the atmosphere, including troposphere and ionosphere which causes impairment on the availability and quality of satellite links during service period. To measure the attenuation due to rain all that is required is to determine the beacon signal strength. The measurements from the beacon and their weather data are central for research to be conducted. The beacon signals often unmodulated continues wave carrier signals, are transmitted by the satellites for station keeping and antenna steering purposes (see Table 1). Some beacons also carry small amounts of information such as telemetry data. These signals are ideal for measuring propagation effects due to their constant transmit signal level [6]-[7].

Table 1 List of some communication satellite's beacon

Name of satellite	Frequency [MHz] and polarization
Eutelsat 133	11200H,12501H
Astra 2F	11112H,11127V
NSS 10	37030V,41995H
Intelsat 23	39500V,11700H
Inmarsat-3F2	39506R
Telstar 12V	11700V,11770.1H
Galaxy 19	11700H,12198V

Fluctuations in received signal strength can therefore be contributed to propagation phenomena. The purpose of a beacon receiver is thus to measure the received signal power and to store the values detected. Keeping a large coverage

requirement results in lower transmit Effective Isotropic Radiated Power (EIRP) whereas a smaller coverage leads to insufficient diversity. In Table 1 is a set of 6 communication satellites have been identified across Europe trading-off the climatic, geographic and demographic diversity. From the position of any of these satellites, three different events can be selected by the receiver station at three different points and the beacon signals received.

At BME-HVT we have a ground station for measurement activities with Alphasat. Our beacon receiver located at the premises of BME-HVT is installed 120m on top of the main BME-HVT building at N47.48 latitudes and E19.06 longitudes, with no interference from any object. The beacon receiver station is split into outdoor (ODU) and indoor units (IDU) respectively and includes High Performance Antennas providing 27dB fade margin.

B. Measurement

Since we do not have three different receiver stations, in order to demonstrate the method we select three successive rain events, where attenuations were high and typical. These events used to represent three location points. The receiver station collects the received power with 1/sec rate, and we also have the meteorological data with 1/min for that period. From the data obtained we depict the received power signal for the beacon and also determine the rainfall rate and the attenuation. The months of April, May and July 2016 were a rainy period and that is, where higher rain events were also observed. Since the higher frequencies are more intensively affected by the rain, the attenuation is very high as well.

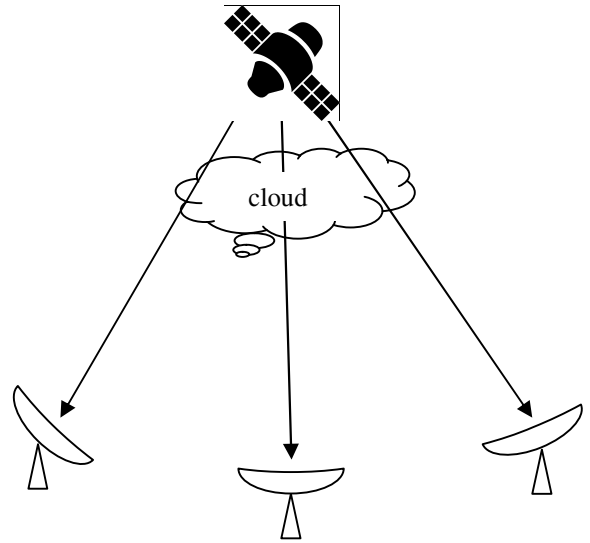


Figure 1 General architecture of the measurement scenario

The time series of this attenuation provides the most relevant information for us to proceed with our calculation to determine the shape of the cloud. Figure 1 represents the general architecture of the measurement scenario to determine the cloud shape.

III. IDENTIFICATION OF RAIN EVENTS

A. Cloud formation

According to the World Meteorological Organization (WMO), cloud is primarily a hydrometeor, consisting of a visible aggregate of minute particles of liquid water or ice, or both, suspended in the free air and usually not touching the Earth's surface. Thus, cloud is the visible manifestation of ongoing atmospheric processes. It is important to understand cloud and its formation because there are two main scales on which these

processes occur. First, clouds consist of many tiny droplets resulting from the condensation of water vapor (gaseous state) into liquid water or ice (solid state). They form when the air is cooled to its dew point. This is considered its condensation or saturation point. The second, is collision and coalescence process which creates larger rain droplets [8]. The fall velocity of larger droplets is greater than smaller drops. Faster droplets are likely to collide with slower droplets in their path. However, not all droplets necessarily collide, since many of the smaller drops may follow the stream lines around the larger ones. It is not guaranteed that colliding droplets will coalesce with one another as the droplets may bounce off a layer of air trapped between the two. Alternatively, the resulting drop could become unstable and breakup. If the cushion of air is squeezed out from between the drops before rebound can occur, the two surfaces make physical contact and coalescence will occur. Figure 2 show a cycle of formation and the shape of a cloud.

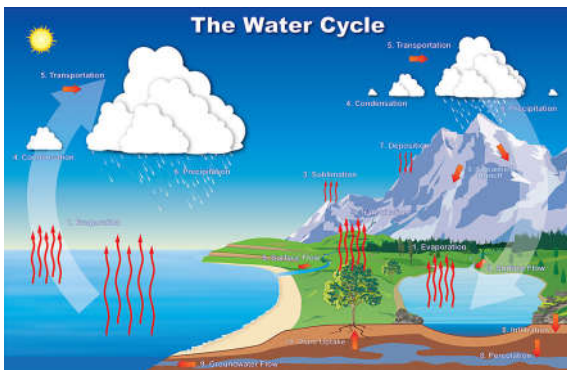


Figure 2. The shape of a clouds, with hydrological cycle and moisture in the atmosphere (graphic courtesy of NOAA's NWS jet stream program)

B. The impact of rain

The impact of rain increases when the rain rate, the frequency and the effective path length increases. Polarization also significantly impacts on rain as since it is one of the major causes of attenuation of propagation signals. The level of the rain rate has a significant effect on the propagated signal during a rainy period, as the raindrop increase in number. This increase may raise the interaction probability between the incident wave and the raindrops, due to the absorption, scattering, and diffraction of the propagated signals which also increases. When the rain rate increase the communication link becomes unreliable and unstable, meaning the effect is more severe in high rainfall rates and greater rainfall intensities. The impact of frequency bands is significant on the attenuation produced during the occurrence of rain. This means at higher frequency the wavelength become smaller and approach the size of the raindrop. The Average Raindrop Size (ARS) or the average width (diameter) of the raindrop is around 1.67 mm [9]; while the wavelength of 10 to 100 GHz ranges between 30 mm to 3 mm. So, a significant interchange of energy will occur between the propagated mm-wave and the raindrops. Such an interaction will result in significant attenuation of the propagated signal. Thus, when the frequency bands become higher, the rain attenuation level of the propagated signal will increase. Between the transmitter and receiver is the effective path length which affect the propagation of mm-waves during rainfall [10], since it is not uniformly distributed along the radio path length. Therefore, the effective path length is not like the actual path length. It is calculated based on rainfall distribution. As a result, accurate rain attenuation is calculated as a function of the effective path length. When the effective

path length increases, the rainfall may cover a longer area between the transmitter and receiver which will produce attenuation [11]; it can also be noted that the total rain attenuation is directly proportional to the effective communication path length.

C. Event selection

It is known that the rain statistics are dependent on the local climatic conditions. This generates the requirement of having usually multiple receive stations that can be scattered over spatially diversified areas. For the actual study in the absence of more receiver stations we have selected three sequential events considering that they belong to the same precipitation field. We calculated the average rain rate and the average wind speed for each event by applying concurrent meteorological measurements. In order to determine horizontal size of the cloud we multiply the rain event duration (sec) with the average wind speed (m/s) during this event. From the rain height we can observe the rate at which rain decays significantly across, showing the vertical dimensions of the cloud.

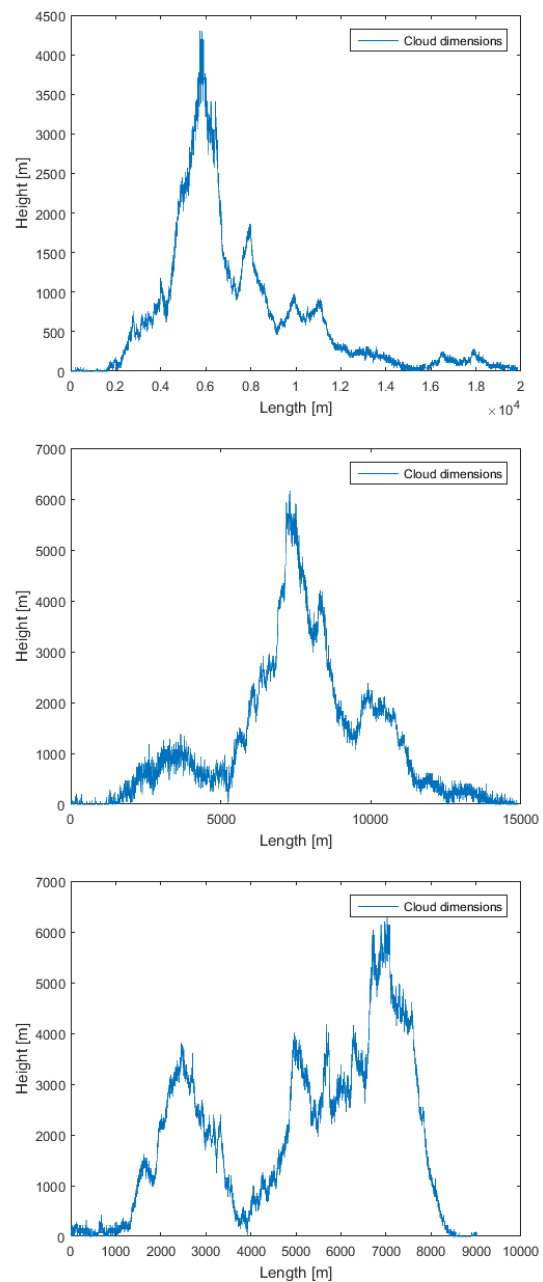


Figure 3. Dimension of the clouds from event 1-3 respectively

In Figure 3 we can see the representation of the cloud from the selection of event 1 to 3 in their respective orders. The rate of decay gives an encouraging view of the cloud in each dimensions.

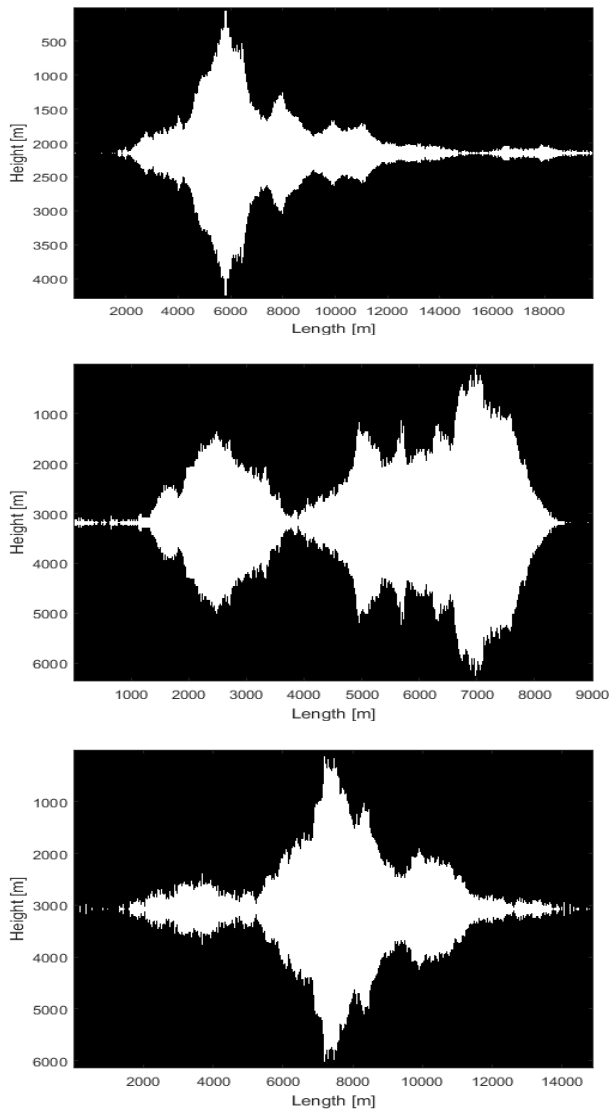


Figure 4. Shape of the clouds from event 1-3 respectively

Figure 4 depicts the shape of the cloud that is obtained from each of the rain event that was selected during the rain activities. Because from that we got the dimension, hence, we produce its corresponding images considering a symmetrical vertical structure. This images displayed gives a shaped view of the cloud respectively from event 1 to 3. It creates the bases for developing the 3D model.

IV. 3D VISUALIZATION OF THE CLOUD

From the framework of this idea we present the results of this study, which is the shape of cloud in three dimensional state. The three rain events produced images of the cloud based on the dimensions from the events. The cloud is viewed from the upper end while the source events are applied as centered and arranged at 120 degrees for the visualization. In Figure 5 we subsequently produce 3D model of the shape of the cloud as shown below.

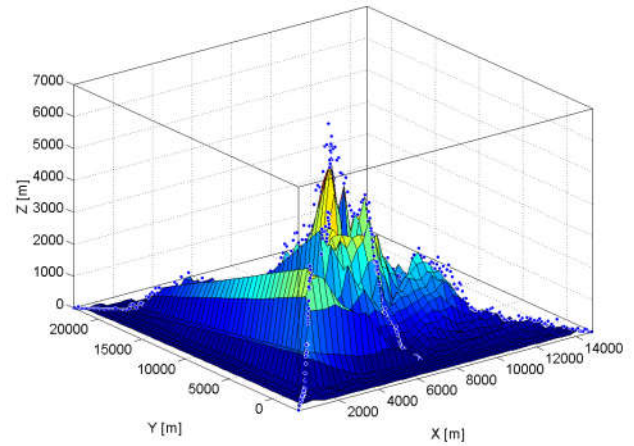


Figure 5. Three dimensional representation of the cloud

CONCLUSION

In this work we have presented results which has established how characterize and determine the shape of the cloud from the rain fields at our receiver station at BME-HVT. The novel approaches here were based on beacon signal method rather than the weather-radar observations of the climatic region in Budapest. The 3D models show a representation of the cloud; these work is part of an ongoing process of characterization of rain fields effects on millimeter-wave communication systems. Rain identification and modeling are two of the building blocks in this research which help determine the shape of the cloud at given instance. Moreover, further work may include growth and decay trends of rain cells to enhance their dynamics state of finding the more accurate shape of the cloud.

REFERENCES

- [1] L. Feral, et al., "Large-scale modeling of rain fields from a rain cell deterministic Model", *Radio Science*, VOL. 41, RS2010, doi:10.1029/2005RS003312, 2006
- [2] H. Sizun, *Radio Wave Propagation for Telecommunication Applications*. Paris, France: Springer, 2005, p. 414.
- [3] C. Capsoni, F. Fedi and A. Paraboni, "A comprehensive meteorologically oriented methodology for the prediction of wave propagation parameters in telecommunication applications beyond 10 GHz", *Radio Science*, vol. 22 (3), pp. 387-393, May-June 1987;
- [4] L. Feral, H. Sauvageot, L. Castanet and J. Lemorton, "HYCELL A New Hybrid Model of the Rain Horizontal Distribution for Propagation Studies:
- [5] Kikkert C. J., Bowthorpe B. and Allen G. "Satellite Beacon Receiver Improvement Using Digital Processing Techniques". *The Fourth International Symposium on Signal Processing and its Applications (ISSPA96)*, pp.517-520, August 1996.
- [6] L. Féral, F. Mesnard, H. Sauvageot, L. Castanet, J. Lemorton: "Rain cells shape and orientation distribution in South-West of France", *Phys. Chem. Earth (B)*, Vol. 25 n° 10-12, pp. 1073-1078, 2000 Excell model
- [7] Capsoni C., Fedi F., Magistroni C., Pawlina A., Paraboni A.: "Data and theory for a new model of the horizontal structure of rain cells for propagation applications", *Radio Science*, Vol. 22, 1987, pp. 395-404.
- [8] Wallace, J. M. and Hobbs, P. V. (2006). *Atmospheric Science: An Introductory Survey*. Academic Press, Burlington.
- [9] A. Tokay, P. G. Bashor, E. Habib, and T. Kasparis, "Raindrop size distribution measurements in tropical cyclones," *Monthly Weather Rev.*, vol. 136, no. 5, pp. 1669-1685, 2008
- [10] *ElvaLink, PPC-1000 Gigabit Ethernet MM-wave Link*. [Online]. Available: <http://www.elva-1.com>
- [11] A. G. Alkholidi and K. S. Altowij, "Free space optical communications Theory and practices," in *Contemporary Issues in Wireless Communications*. Rijeka, Croatia: InTech, 2014.

Determination of 3D surface deformation for the 2018 Oaxaca earthquake using InSAR

G. László

Institute of Geoinformatics, Alba Regia Technical Faculty,
Óbuda University
Székesfehérvár, Hungary
laszlo.gergely@amk.uni-obuda.hu

L. Földvály

Institute of Geoinformatics, Alba Regia Technical Faculty,
Óbuda University
Székesfehérvár, Hungary
Geodetic and Geophysical Institute, RCAES, HAS
Sopron, Hungary
foldvary.lorant@amk.uni-obuda.hu

Abstract—SAR images acquired along descending and ascending orbits has a view of a surface deformation from a different angle. Accordingly, the surface deformation they show are affected by foreshortening and related projection errors. By combination of two deformation models, 3D deformation can efficiently be modelled. In this study, reconstruction of the surface motions due to the 2018 Oaxaca earthquake is performed, with the joint use of a Sentinel-1A deformation model taken on a descending orbit and a Sentinel-1B deformation model taken along an ascending orbit.

Keywords—InSAR, Sentinel-1, ascending/descending orbit, deformation analysis, 3D modelling

I. INTRODUCTION

The basic concept of the dedicated joint Copernicus program of European Space Agency (ESA) and European Union (EU) is to provide continuous monitoring programmes over timescales of decades [1]. The Sentinel missions of the Copernicus program are designed for routine observations of operational GMES (Global Monitoring and Environmental Security) services [2]. Among the 6 Sentinel mission, Sentinel-1 satellites are providing radar imaging for land and ocean services. Accordingly, Sentinel-1 images enable determination of surface deformation over large region even with some cm amplitude over short and long timescales as well.

Volcanic and seismic events are often accompanied by measurable surface deformations over large area within the time frame of some days. As it was already shown by [3], pre-, co- and post-seismic deformations can efficiently be determined depending only on the timing of the images with respect to the event. The timing of the images is, however, haphazard, cannot be planned or controlled. Thus, the densification of images by the extension of the Sentinel-1 satellite mission with additional satellites is highly justified.

Meanwhile, the expansion of the mission with new satellites is valuable only if the different satellites provides equivalently useful result with similar accuracy at the same spatial resolution. As in 2018, Sentinel-1 mission contains two satellites: 1A and 1B [2], while two more satellites, 1C and 1D are already contracted for an unknown date of launch [4]. The repeat cycle of a Sentinel-1A satellite is 12 days, which has already been reduced to 6 days by the launch of Sentinel-1B satellite, which

is an identical twin of Sentinel-1A with 6 days delay in its orbit. As demonstrated by [5], successful combination of Sentinel-1A and Sentinel-1B images can be achieved.

In this paper we investigate whether the results achieved by of Sentinel-1A and Sentinel-1B images can also serve to provide appropriate base of spatial modelling of an event. First, independent processing of the same event is performed using images acquired from a descending (Sentinel-1A) and from an ascending (Sentinel-1B) orbits. Subsequently, the two models are combined to differentiate horizontal and vertical motions.

II. THE TEST EVENT

The test event is the deformation caused by the earthquake at 23:39:39 UTC of 16 February, 2018 in Oaxaca, Mexico with a magnitude of 7.2 M_w, which has resulted in an intense shake over a huge region of South Mexico, c.f. Fig. 1 [6]. The hypocenter of the event is at $\phi = 16.386$ and $\lambda = -97.979$ (with an accuracy of ± 4.3 km) with a depth of $22.0 \text{ km} \pm 1.8 \text{ km}$ [6].



Figure 1. Shake map (intensity) of the Oaxaca 2018 event [6]

The focal mechanism shows a normal slip with a dip angle of the nodal planes of 12° (NP1) [and 78° (NP2), c.f. the beach ball model of the event on Fig. 2. The direction of the slip is completely downward (rake of NP1 is 91° , rake of NP2 is 90°), along the Middle America Trench, where the strike angle of NP1 is 297° , and of NP2 116° [6].

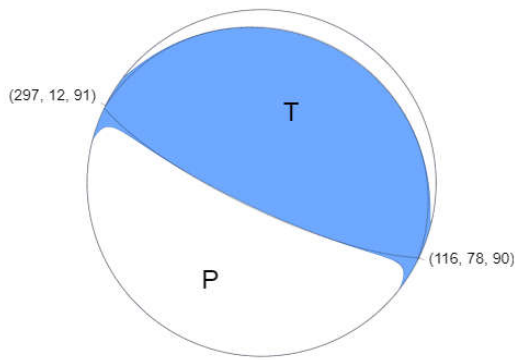


Figure 2. The beach ball model of the Oaxaca 2018 event [6]

This event can be clearly separated from other related events: there have been no relevant pre-shocks (the largest one has occurred 2 days before the main event with an M4.4 magnitude). The post shocks contain two notable events: there has been a quake approximately an hour after the main shock (at 00:36:52 UTC of 17 February with a magnitude of 5.8 M_w and depth of 3.5 km), and another one two days later (at 06:56:58 UTC of 19 February with a magnitude of 5.9 M_w). Even though the effect of these post-seismic events on surface displacement cannot be separated from the main event, they are negligible, as the seismic moment of the main event has is $7.996 \cdot 10^{19}$ Nm, while for the post shocks is only $5.817 \cdot 10^{17}$ Nm and $8.329 \cdot 10^{17}$, respectively for 17 and 19 February events. It means that due to the post shocks the seismic moment (practically related to ground motions) became less than 2% of that of the main shock, so surface deformations are dominated by the main shock. The same can be understood when the released energy of the main shock and of the two largest post shocks are compared: the energy released by these events are $3.98 \cdot 10^{15}$ J, $3.16 \cdot 10^{13}$ J and $4.47 \cdot 10^{13}$ J, respectively, so the energy released by the post-shocks is less than 2% of that of the main shock.

III. INTERFEROGRAMM AND SURFACE DEFORMATION MODEL

Surface deformation of the event has been determined independently for Sentinel-1A and Sentinel-1B images. Images have been downloaded from the Copernicus Open Access Hub [7], where images on 27 January and 20 February for Sentinel-1A, and on 5 February and 17 February for Sentinel-1B have been found to be useful. Even though the time span is notably different, presumably differences in the deformation can be regarded mainly to the pre-seismic deformations, in which case the difference of starting at 27 January or at 5 February may be relevant, and partially can be regarded to the post-seismic differences, as the effect of the 19 February post-shock event is excluded from the Sentinel-1B, but included in the Sentinel-1A image.

Using these images, processing was performed by using the Sentinel-1 Toolbox of the Sentinel Application Platform (SNAP) [8]. The processing (including co-registration of the images, formation of the interferograms, deburst of the images, removal of the topographic phase, the Goldstein phase filtering, phase unwrapping, determination of the phase displacement, georeferencing and removal of the ellipsoidal correction) is done routinely, the sequence is detailed in [9].

The resulted phase maps are shown on Fig. 3 and Fig. 4. The structure of the deformation is visually similar, though differences in the detailed pattern can be recognized. Fig. 5 shows the difference phase maps; according to this image, a displacement of the center of the location of the maximal deformation is obvious.

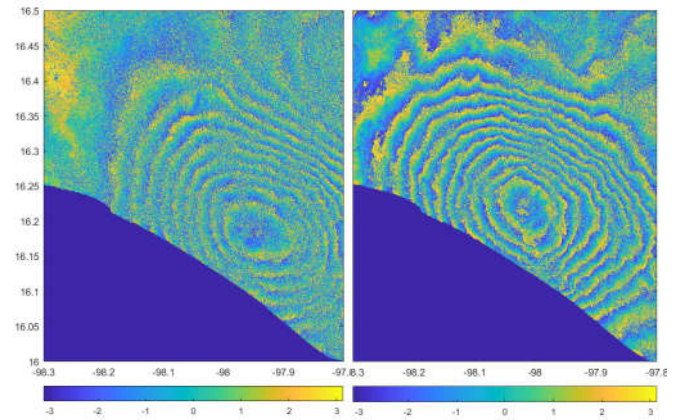


Figure 3-4. Georeferenced Sentinel-1A and 1B phase map

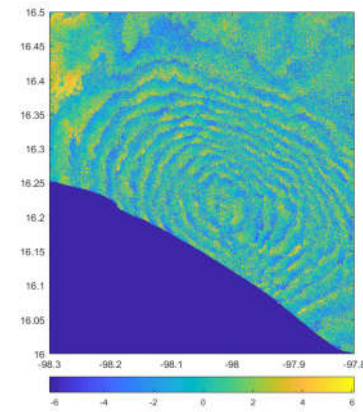


Figure 5. The difference phase map

The corresponding deformations have been determined by the Snaphu software [8]; these are displayed by Fig. 6 and Fig. 7, and their difference is on Fig. 8. The deformations on Fig. 6 and Fig. 7 are relevantly different. In fact, they refer to deformations along Line-Of-Sight (LOS) of the beam emitted by the satellite.

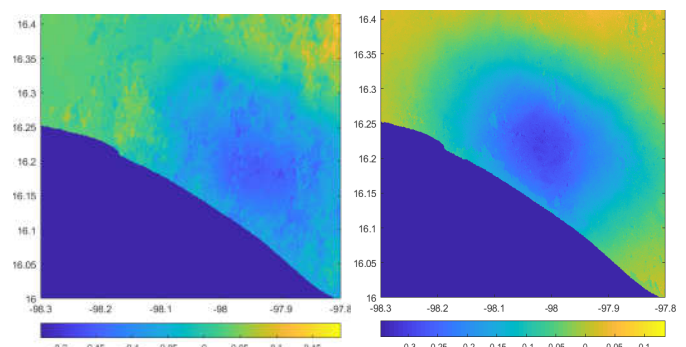


Figure 6-7. Deformation derived from Sentinel-1A and Sentinel-1B images. Unit: [m]

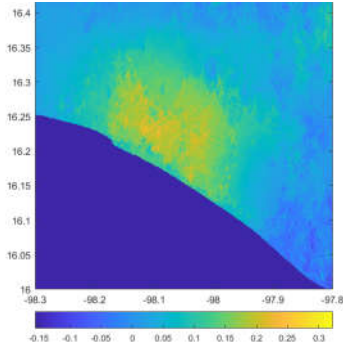


Figure 8. Deformation differences. Unit: [m]

For illustration of the differences: on Fig. 8, the range of height variation is 6.07 cm (with maximal depth of -22.55 cm), while on Fig. 7 it is 9.61 cm (with maximal depth of -34.69 cm). The range of the difference image is 6.33 cm, which is in the order of the magnitude of the observed deformations.

Beyond the range of subsidence, also the affected area by the deformation are different. According to rough estimates, the subsidence occurs over an area of $98 \cdot 10^3 \text{ km}^2$ and $139 \cdot 10^3 \text{ km}^2$, respectively for Sentinel-1A and Sentinel-1B, so the affected area seems to be 1.4 times larger for Sentinel-1B observation. Accordingly, volume of subsidence is $3.9 \cdot 10^8 \text{ km}^3$ and $11.7 \cdot 10^8 \text{ km}^3$, which means 3.3 times more volume for the Sentinel-1B observation, in accordance with the detected larger height variations.

By visual test of Fig. 3, Fig. 4, Fig. 6 and Fig. 7, the center of the subsidence has been observed to be located at $\phi = -97.95^\circ$ and $\lambda = 16.31^\circ$ for the Sentinel-1A image, while at $\phi = -98.02^\circ$ and $\lambda = 16.28^\circ$ for the Sentinel-1B image. This means approximately a displacement of 3.9 km and 1.8 km in Northing and Easting directions, respectively.

In order to analyze the spectral behavior of the deformation models, 1D Fourier-spectrum of each rows (referring to a certain longitude) and columns (so referring to a latitude) of the deformation model derived by Sentinel-1A and Sentinel-1B has been determined. The Fourier-spectra have differed by each longitude/latitude, so for visualization, an average spectrum is provided by longitude on Fig. 9 (meaning that the spectra derived for the different longitudes are averaged) and by latitude on Fig. 10 (averaged by latitude). Both figures apply logarithmic scales on both axes – logarithmic scale along the ordinate axis emphasizes the order of magnitude of the amplitude, while the logarithmic scale along the abscissa axis emphasize the relevance of the long frequencies.

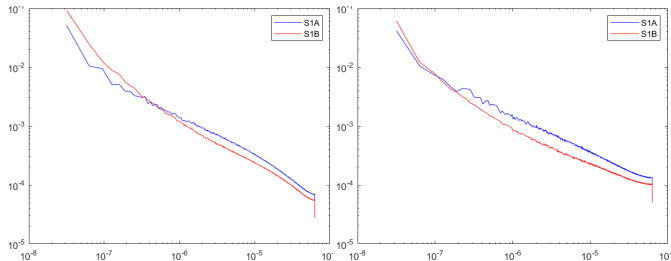


Figure 9-10. Average of the FFT derived for each longitude and latitude.

Fig. 9 and Fig. 10 suggest that Sentinel-1B deformation model has more signal on low frequencies, but much smoother on high frequencies. Basically, it means that the larger signal content of Sentinel-1B model is contributed by the large scale features, but the surface of the subsidence is much smoother. As a consequence, it can be concluded that the single orbit interferometric SAR phase maps deliver inhomogeneous, distorted estimate of surface deformations.

IV. MODELLING OF THE 3D CO-SEISMIC SURFACE DISPLACEMENTS

Displacements on Fig. 6 and Fig. 7 are the projections of the real 3D surface deformation onto the LOS directions of the actual orbits. During determining the interferograms, it is essential to choose as short as possible baselines in order to minimize the stereoscopic effect and the speckle geometrical decorrelations. When 3D deformations are demanded to be determined, it is important that two deformation models should be in notably different geometry, thus images taken along ascending and descending orbits are chosen, consequently, the angles of projection of data acquisition are relevantly different, thus 3D determination similarly to the bundle adjustment of stereophotogrammetry becomes possible.

A method of amplitude matching for determining 3D deformation has been developed by [10], this method makes use of the offsets observed in range and azimuthal for achieving the 3D information. This has been further developed by [11], where the offset in range has been eliminated, and rather the offset information in azimuth and in LOS has been applied. In the present study, the use purely on LOS is proposed as it is the direct measure of the surface deformation.

The incident angle, i.e. the angle between nadir and the LOS is noted by θ , and the azimuth of the satellite's track by α . The direction of the **LOS** vector is then

$$\mathbf{LOS} = \begin{bmatrix} \cos\theta \\ \cos\left(\alpha - \frac{\pi}{2}\right) \sin\theta \\ \sin\left(\alpha - \frac{\pi}{2}\right) \sin\theta \end{bmatrix} \quad (1).$$

The observed deformation along the LOS, Δ_{LOS} is then the projection of the actual deformation vector, \mathbf{r} , which is

$$\mathbf{r} = \begin{bmatrix} r_U \\ r_N \\ r_E \end{bmatrix} \quad (2),$$

therefore

$$\Delta_{LOS} = \mathbf{r} \cdot \frac{\mathbf{LOS}}{|\mathbf{LOS}|} =$$

$$\cos\theta r_U + \cos\left(\alpha - \frac{\pi}{2}\right) \sin\theta r_N + \sin\left(\alpha - \frac{\pi}{2}\right) \sin\theta r_E \quad (3).$$

Accordingly, the following linear system of equations can be defined:

$$\begin{aligned}
& \begin{bmatrix} \Delta_{LOS}(A) \\ \Delta_{LOS}(D) \end{bmatrix} + \begin{bmatrix} v(A) \\ v(D) \end{bmatrix} = \\
& = \begin{bmatrix} \cos\theta(A) & \cos\left(\alpha(A) - \frac{\pi}{2}\right)\sin\theta(A) & \sin\left(\alpha(A) - \frac{\pi}{2}\right)\sin\theta(A) \\ \cos\theta(D) & \cos\left(\alpha(D) - \frac{\pi}{2}\right)\sin\theta(D) & \sin\left(\alpha(D) - \frac{\pi}{2}\right)\sin\theta(D) \end{bmatrix} \\
& = \begin{bmatrix} r_U \\ r_N \\ r_E \end{bmatrix}
\end{aligned} \tag{4}$$

in which equation variables referring to the geometry of the ascending and the descending orbit are noted by (A) and (D), respectively. Equation (4) in short notation reads:

$$\Delta + \mathbf{v} = \mathbf{A} \cdot \mathbf{r} \tag{5}$$

This leads to an ill-conditioned, irregular, inhomogeneous systems of linear equations, which can efficiently be solved by minimizing the least squares of the corrections and inverting the normal matrix by Singular Value Decomposition. Equation (3) can be solved by Least Squares Adjustment as

$$\mathbf{r} = (\mathbf{A}' \cdot \mathbf{A})^{-1} \cdot (\mathbf{A}' \cdot \Delta) \tag{6}$$

The adjustment is performed pixel-wise. The azimuth, α and the incident angle, θ , i.e. angles for the orientation of the beam used for taking the images, can be retrieved from the metadata of the images, while the deformation along the LOS, Δ_{LOS} is taken from each deformation models, c.f. Fig. 6 and Fig. 7. Then the 3 components of the deformation can be determined by (6). The results are shown on Fig. 11, Fig. 12 and Fig. 13.

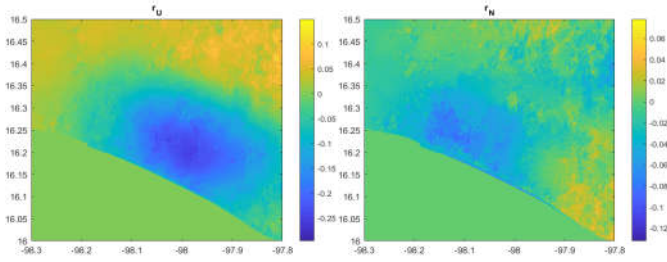


Figure 11-12. Upward and Northward co-seismic motion of the Oaxaca earthquake, 2018.

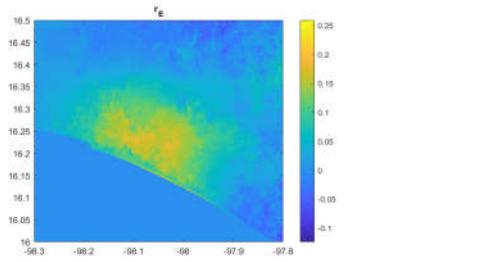


Figure 13. Eastward co-seismic motion of the Oaxaca earthquake, 2018.

V. DISCUSSIONS AND CONCLUSIONS

As the 2018 Oaxaca earthquake is a quite recent event, no solutions of related deformation analysis has been published so far in the printed literature, though online solutions are available

[12],[13]. These studies both has determined the deformation using Sentinel-1B images, resulting in deformation along LOS. Their results are very similar to our Fig. 7, and the deformations were interpreted purely on this information. According to the analyses before, in case of Fig. 7, the range of height variation is 9.61 cm with a maximal depth of -34.69 cm, the affected area by the subsidence is $139 \cdot 10^3 \text{ km}^2$, and the volume of subsided mass is $11.7 \cdot 10^8 \text{ km}^3$. The location of maximal deformation was identified to be at $\phi = -98.02^\circ$ and $\lambda = 16.28^\circ$.

Similar information for the 3D deformation analysis is derived. The range of height variation is 7.70 cm with a maximal depth of -29.62 cm, the affected area by the subsidence is $123 \cdot 10^3 \text{ km}^2$, the volume of subsided mass is $8.5 \cdot 10^8 \text{ km}^3$, and the location of maximal deformation was identified to be at $\phi = -97.98^\circ$ and $\lambda = 16.20^\circ$. Accordingly, the interpretation of LOS motions as vertical motions yields an overestimation of the actual deformation to 1.2 times larger. This is in line with the rough estimation, as the main component of Δ_{LOS} is $\cos\theta r_U$, c.f. equation (3), and the coincident angles of the acquired images range are in the $[32.1^\circ \text{ } 36.5^\circ]$ interval.

Note that Δ_{LOS} deformation component only along two lines are available, it means that the resolved deformation vector, \mathbf{r} is only that component of the actual 3D vector, which lies in the plane stretched by $\mathbf{LOS}(A)$ and $\mathbf{LOS}(D)$ vectors (c.f. Fig. 14). The actual deformation, however, might have a perpendicular component as well, whereabouts no information contained in the observed deformations along LOS vectors.

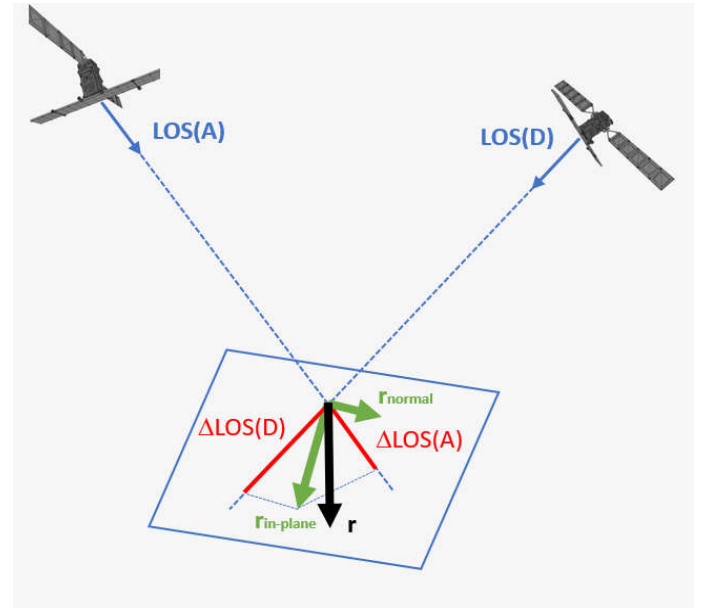


Figure 14. Sketch of deformation observation. The actual deformation, \mathbf{r} is projected onto the vectors defined by LOS vectors; along them the observed deformation is Δ_{LOS} . The observation vector can be decomposed into two components (green vectors): one lies in the plane defined by the LOS vectors (blue trapeze), while the other is perpendicular to this plane. The observed Δ_{LOS} deformations are only affected by the in-plane component.

As this vector component is perpendicular to observation plane, it is directed to

$$\mathbf{v}_{pr} = \mathbf{LOS}(A) \times \mathbf{LOS}(D) = \begin{bmatrix} \cos\left(\alpha(A) - \frac{\pi}{2}\right) \sin\theta(A) \cdot \sin\left(\alpha(D) - \frac{\pi}{2}\right) \sin\theta(D) - \cos\left(\alpha(D) - \frac{\pi}{2}\right) \sin\theta(D) \cdot \sin\left(\alpha(A) - \frac{\pi}{2}\right) \sin\theta(A) \\ \sin\left(\alpha(A) - \frac{\pi}{2}\right) \sin\theta(A) \cdot \cos\theta(D) - \sin\left(\alpha(D) - \frac{\pi}{2}\right) \sin\theta(D) \cdot \cos\theta(A) \\ \cos\theta(A) \cdot \cos\left(\alpha(D) - \frac{\pi}{2}\right) \sin\theta(D) - \cos\theta(D) \cdot \cos\left(\alpha(A) - \frac{\pi}{2}\right) \sin\theta(A) \end{bmatrix} \quad (7).$$

Considering the actual angles of the images taken in this case, the unit vector perpendicular to the plane of observations is approximately

$$\mathbf{v}_{pr} = \begin{bmatrix} 0.1431 \\ 0.8573 \\ 0.4945 \end{bmatrix} \quad (8).$$

Accordingly, 1 cm deformation along the undetected perpendicular component affects the Up, North, East components by 1.4 mm, 8.6 mm and 4.9 mm, respectively. It means that the estimated vertical component is the most reliable, while the horizontal motion is notably affected by this perpendicular component. As the perpendicular component of the deformation influences the North component more (57.3%) than the East component (33.1%), the azimuth is influenced relevantly by the perpendicular component. Considering the central part of the deformation area, Northward deformations are typically -8 cm, while eastward deformations are modelled by 20 cm, the typical value of the azimuth angle in the present situation is $\alpha = 180^\circ - \arctan(|E|/|N|) = 180^\circ - \arctan(|20\text{cm}/|-8\text{cm}|) = 111,80^\circ$. Accordingly, by 1 cm deformation the azimuth, $\alpha = 180^\circ - \arctan(|E+\Delta E|/|N+\Delta N|) = 180^\circ - \arctan(|20\text{cm}+4.9\text{mm}/|-8\text{cm}+8.6\text{mm}|) = 109,21^\circ$ differs from the present situation slightly, by $\Delta\alpha = 2,59^\circ$. However, by 5 cm deformation it is $99,36^\circ$ resulting in $\Delta\alpha = 12,44^\circ$ difference, and by 10 cm deformation the azimuth is $+88,62^\circ$, which differs relevantly, by $\Delta\alpha = 23,18^\circ$. Therefore, in case a relevant perpendicular component exists, it should be apparent in visual test of the horizontal vectors. For the visual test, horizontal motions are displayed by vectors on Fig. 15. The vector field coincides nicely with the tectonic structures, also they are reliable consequences of the focal mechanism, c.f. the surface section of the first nodal plane according to Fig. 2.

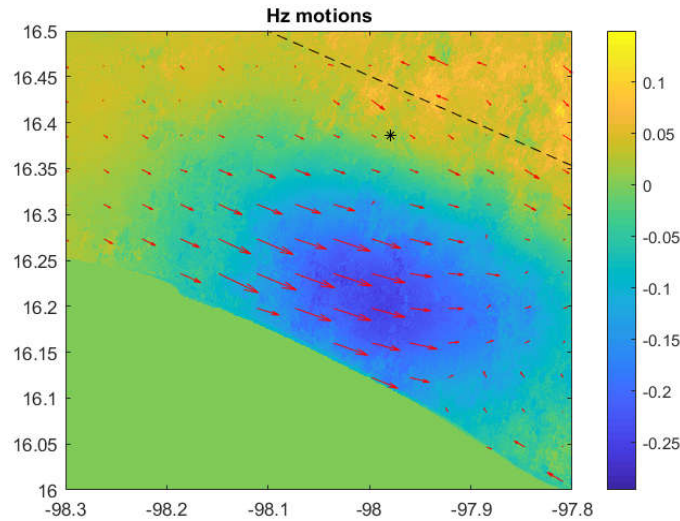


Figure 15. Horizontal motion vectors of the Oaxaca earthquake, 2018. The black asterisk shows the epicenter, while the first nodal plane is shown by dashed black line.

Summarily, even though the used images alone cannot provide full recover of the 3D deformations, as the horizontal components seem to be reliable according to seismological consideration, the undetermined component may not be too large. Accordingly, the estimated components are rather realistic. Note, however, that in the lack of reliable independent information on the deformation of the Oaxaca event, no adequate validation of the derived 3D deformations could be performed. Also, simple geometrical considerations for the present orientation of image acquisition have found the rate of LOS and vertical deformations to be about 1.2 is reliable. Accordingly, the combination of two LOS deformation models derived from images taken along a descending and an ascending orbit can be considered to provide realistic results.

REFERENCES

- [1] M. Berger, J. Moreno, J. A. Johannessen, P. F. Levelt, R. F. Hanssen, "ESA's sentinel missions in support of Earth system science", *Remote Sensing of Environment*, 2012.
- [2] Sentinel-1, *ESA's radar observatory mission for GMES operational services*, ESA Special Publication (SP-1322/1), 2012.
- [3] G. László, L. Földváry: "Application of Sentinel-1 data for determination of surface deformation due to volcanic and seismic events", *17th edition International Technical-Scientific Conference Modern Technologies for the 3rd Millennium*, 55-60, ISBN 978-88-87729-49-8.
- [4] Ch. Rossi, "Decolla La Space Economy Italiana", *AirPress*, 15.12.2015, retrieved on 06.09.2018, link: <http://www.airpressonline.it/8562/decolla-la-space-economy-italiana/>

- [5] G. László, L. Földváry, “Combined use of Sentinel-1A and Sentinel-1B data for determination of post-seismic vertical surface deformation - a case study: Perugia, 2016”, *Proceedings of the 12th International Symposium on Applied Informatics and Related Areas (AIS 2017)*, Székesfehérvár November 9, 2017, pp. 61-65, ISBN: 978-963-449-032-6, 2017.
- [6] USGS, “M 7.2 - 3km S of San Pedro Jicayan, Mexico earthquake information”, *USGS homepage*, retrieved on 06.09.2018, link: <https://earthquake.usgs.gov/earthquakes/eventpage/us2000d3km#executive>
- [7] Sentinel Data Hub, *Copernicus Open Access Hub*, retrieved 06.09.2018, link: <https://scihub.copernicus.eu/dhus/#/home>
- [8] Sentinel-1 Toolbox of the Sentinel Application Platform (SNAP), *Science Toolbox Exploitation Platform (STEP)*; retrieved on 06.09.2018, link: <http://step.esa.int/main/toolboxes/snap/>
- [9] G. László, L. Földváry, “Determination of the surface deformation during the eruption of the Sakurajima volcano in February, 2016”, *Proceedings of the 11th International Symposium on Applied Informatics and Related Areas (AIS 2016)*, Székesfehérvár November 11, 2016, pp. 74-78, ISBN: 978-615-5460-92-0, 2016
- [10] Michel R, Avouac J. Measuring near field coseismic displacements from SAR images: Application to the Landers earthquake. *Geophys Res Lett*, 26: 3017–3020, 1999
- [11] Hu, J., Li, Z. W., Zhu, J. J., Ren, X. C., Ding, X. L.: Inferring three-dimensional surface displacement field by combining SAR interferometric phase and amplitude information of ascending and descending orbits, *Science China Earth Sciences*, 53:4, 550–560, 2010
- [12] InSAR map of deformation due to M7.2 Oaxaca Earthquake, last retrieved on 16 January, 2019, link: <https://disasters.nasa.gov/oaxaca-mexico-earthquake-2018/insar-map-deformation-due-m72-oaxaca-earthquake>
- [13] Surface Deformation related to Oaxaca Earthquake, last retrieved on 16 January, 2019, link: <https://disasters.nasa.gov/oaxaca-mexico-earthquake-2018/surface-deformation-related-oaxaca-earthquake>

The MarsQuake Program for Hungarian High School Students

Márta Kiszely

MTA CSFK Geodetic and Geophysical Institute
Budapest, Hungary
kiszely.marta@csfk.mta.hu

György Hudoba

Alba Regia Technical Faculty, Óbuda University
Székesfehérvár, Hungary
hudoba.gyorgy@amk.uni-obuda.hu

The MarsQuake project is intended to provide a set of teaching resources and classroom activities that will use the latest data and images sent back from the NASA InSight mission to Mars. The British Geological Survey, the National Space Academy and the Durham University together published a background science booklet for this project aimed at 11–18 year-olds students. The publications contained different activities include modeling and locating meteorite impacts known as 'marsquakes'. To start this MarsQuake project the translation of this book for Hungarian students was prepared in 2018.

marsquakes, earthquakes, seismology

I. INTRODUCTION

The "MarsQuake" program was launched in Hungary as part of the "Seismology in School" initiative, which aims to reach secondary school students and create interest in earthquakes and astronomy. An educational publication was published in 2018, which is an edited translation of the "MarsQuakes – Seismology on another planet" booklet [1] [2]. We held several educational presentations and wrote article [3] in Hungary. We would like to open a new perspective on scientific knowledge in the field of earth sciences for Hungarian students.

II. SEISMOLOGY IN SCHOOL

The "Seismology in School" initiative was launched in 2016 as an educational program of the Kövesligethy Radó Seismological Observatory. This educational program in Europe dates back to 1995. An abundance of English resources is available on this topic for students. Now several articles and videos has been translated and published on a Hungarian website (<http://suliszeizmo.hu>). A school seismograph has been purchased. Schools can also buy this semi-professional tool that was specifically designed for them. It is easy to assemble, its operating mechanism is visible, and it is easy to learn how to handle the user program of the instrument. The goal is to give students a high degree of interest in seismology and let them manage their own instrument. Observing earthquakes with their own school instrument gives the students a "wow" experience. The students can see a real natural phenomenon in real time! They will learn how science works (Fig. 1).

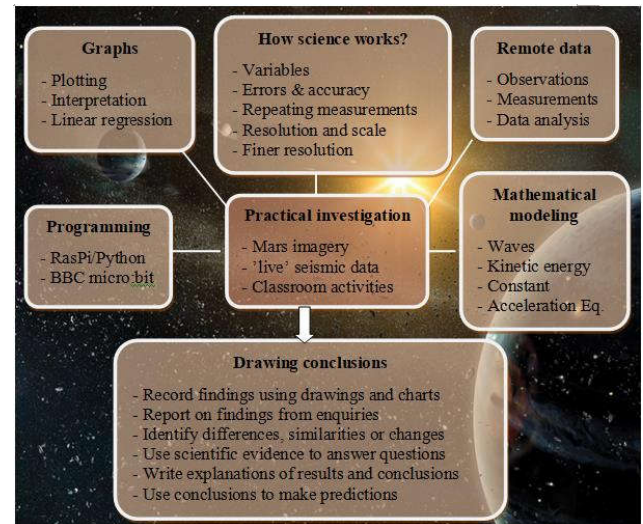


Fig. 1. The students will learn how science works

III. THE INSIGHT MISSION AND THE SEIS INSTRUMENT

NASA's InSight (Interior Exploration using Seismic Investigations, Geodesy and Heat Transport) Mars lander carries a seismometer, SEIS (Seismic Experiment for Interior Structure). It sits still, directly on the surface of the Red Planet, and waits to detect seismic vibrations that make it to its location. The vast majority of earthquakes on Earth are connected to plate tectonics. However, plate tectonics is not existing on the Mars, so we expect 100 times smaller seismic activity on the Mars than that of Earth. The seismic waves can be produced mainly by meteorite impacts. InSight's primary objective will be to uncover how a rocky body in space forms and evolves to become a planet, and determine the size, composition, physical state (liquid/solid) of the Martian core.

The SEIS seismometer consists of a total of six seismic sensors that record the vibrations of the Martian soil in three directions in space (up–down, north–south and east–west) and at two different frequency ranges (VBB covering 0.01–10 Hertz and SP covering 0.1–50 Hertz). The seismic waves will be excited by marsquakes, meteorite impacts, and even surface vibrations generated by activity in Mars' atmosphere and by weather phenomena such as dust storms.

IV. STARTING THE MARSQUAKE “MARSRENGÉSEK” PROGRAM

The MarsQuake education project is a UK Space Agency-funded initiative led by the British Geological Survey with partners from the National Space Academy, University of Leicester and University of Bristol. The project developed a set of classroom activities and learning resources to support the mission. The program is complex. On the one hand, the Mars high resolution image management program should be known (HiView) so as the program for displaying and processing signals registered by the InSight SEIS instrument (jAmaSeis). The types of seismic waves should be recognized and users must be familiar about many other astronomical and seismological topics.

The „MarsQuakes” program is available in the following areas in Hungarian:

A. Two websites:

- MTA CSFK GGI: <http://suliszeizmo.hu>
- Terkán Lajos Public Observatory: <http://telapo.datatrans.hu/mars>

These websites contain details from the MarsQuakes book, the history of Mars research, interesting facts about Mars, and seismological knowledge.

B. Publication

The MarsQuakes – Seismology on another planet “Marsrengések – Szeizmológia más bolygókon” is downloadable from these websites. This booklet contains the InSight mission overview, comparison of the Earth and Mars planets, knowledge about plate tectonics and seismology. It contains different student activities including modeling and locating meteorite impacts known as 'marsquakes'. It will be shown to the students how to look at seismic data using simple spreadsheets, semi-professional analysis software and simple computer programs, which they could write themselves.

C. Open Facebook group

This „Marsrengések – kiből lesz marskutató?” facebook group (Marsquakes – who will be a Mars discoverer?) ”is updated regularly with news about InSight.

D. Scientific lectures and presentations

- Galileo Webcast: György Hudoba: Mars targeted! http://www.galileowebcast.hu/live/live_20181015.html
- Skeptics XXIV. National Conference: Márta Kiszely: Marsquakes - who will be a Mars discoverer? (<https://www.youtube.com/watch?v=sV19m8okRV8&list=PLeNxi-TyRAb61fbR10F9-IAQRhgTnaZkH&index=3>)

E. Scientific lectures and presentations

- Participation in popular scientific events (Earth Science "Whirlabout" in the Hungarian Natural History Museum (2018))
- Participation in Budapest the Capital of Sciences 2018

So far, there are about 25 candidates to MarsQuakes program, including one astronomical circle. Anyone can join to this program, regardless of where they live. Currently there are applicants from Balatonfüred, Budapest, Dombóvár, Érsekújvár (Slovakia), Gödöllő, Gyál, Kerepes, Mátészalka, Sásd, Sopron, Szeged, Székesfehérvár and Szigetszentmiklós.

V. THE ACTIVITY AND THE EXPERIENCES OF THE MARSQUAKE PROGRAM IN HUNGARY

The member of the MarsQuake program has to show great tenacity, as they must install two programs on their computer, with menu items in English. These are the high-resolution Mars image processing HiView and the school seismograph data processing jAmaSeis programs. In addition, they had to familiarize themselves with the websites that publish the parameters of the actual earthquakes. Due to the age-specific characteristics of the candidates, the easiest way to keep in touch with each other is through our facebook group. The members of facebook group will find the latest news and photos posted on the latest InSight program in Hungarian (<https://twitter.com/NASAINsight>) and see the questions and results of others. We want to know the activity of the applicants and to prepare them for analyzing the SEIS data sent back from Mars with different tasks. The members of marsquake group have been received two challenges (with a longer deadline). In addition, they had to constantly monitoring the latest earthquakes with the help of the jAmaSeis program.

- CRATER CHALLENGE 2018: The task was to complete the first student experiment, which is included in the annex of MarsQuakes – Seismology on another planet "Marsrengések – Szeizmológia más bolygókon". Meteor hits has to be modeled on a surface of flour and cocoa powder and observed its features. Thereafter the size of a real Mars crater has to be determined using the HiView program.
- SURFACE WAVES ON MARS: During this task, a young Mars researcher has to learn the characteristics of the surface waves and has to perform a computational task.



Fig. 2. The Coolstarz astronomy circle in Mátészalka

Half of the applicants are currently active. The others are likely to follow the results of InSight. The most successful is the astronomical circles of Móricz Zsigmond Greek Catholic Secondary School in Mátészalka, headed by Erzsébet Kardis

Bardócné, and the physics circle of Lánzos Kornél High School headed by of Sándor Újvári in Székesfehérvár (Fig. 2).

One of the solutions of CRATER CHALLENGE 2018 is shown in Fig. 3. Szabó Bence modeled the meteor impacts on a surface of flour and cocoa powder. The patterns of impact crater can be investigated. The ejecta and rays thrown up from the impact event could be seen and measured.

Fig. 4. shows the results of one crater dimension measurement. The students had to choose a crater from the “New crater Excel 2007-2013.xlsx” list, and download its image from the webpage (<https://www.uahirise.org/>) as a compressed bitmap file (JP2) and open with HiView program, and measure the diameter of crater in pixels. The real size of the crater can be calculated knowing the image scale.

Fig. 5 shows the result of an earthquake epicenter determination with jAmaSeis program, recognizing and using the of P and S seismic waves on different seismic stations.



Fig. 3. The pupils and physics teacher of Lánzos Kornél High School



Fig. 4. Bence Szabó's (Gödöllő) solution of modelling crater impacts

According to our experience, those who worked in a team with the guidance of a teacher were more successful and learned to use the programs more easily than those who worked alone.

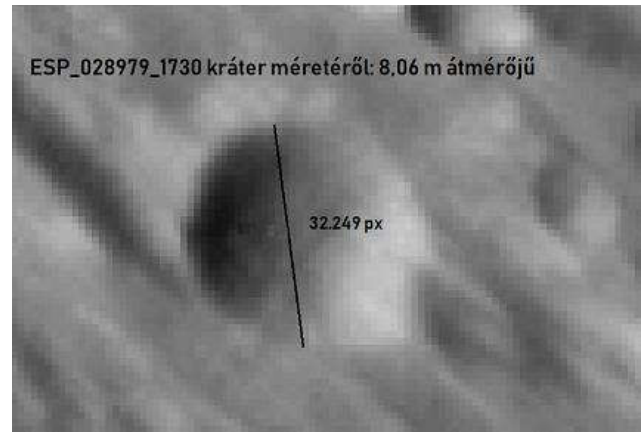


Fig. 5. Bence Szabó's solution of CRATER CHALLENGE 2018

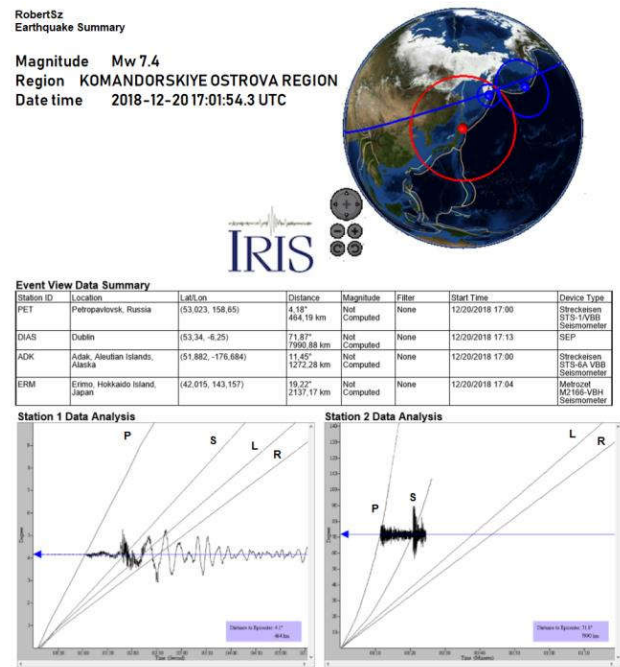


Fig. 6. Róbert Szerencsi's (Kerepes) defined an earthquake epicenter with the P and S waves on four different station

ACKNOWLEDGMENT

We would like to thank Paul Denton (British Geological Survey) who authorized the “MarsQuakes – Seismology on another planet” book edition and publication in Hungarian.

REFERENCES

- [1] P. Denton, J. P. Stevenson, and A. McMurray “MarsQuakes – Seismology on another planet” Nottingham: British Geological Survey: ISBN 978-0-85272-866-6. (2017)
- [2] [3] M. Kiszely (translated.) “Marsregések – Szeizmológia más bolygókon” MTA CSFK GGI: ISBN 978-963-8381-39-2, pp 73 (2018)
- [3] Márta Kiszely “A Vörös Bolygó megfúrása – Meteorbecsapódások marsregésekkel” Élet és Tudomány, 73, 22 678-680. (2018)

Detection of Tsunamis based on Ionospheric Satellite Signals

Gergely Mindler, Bence Szendi, Mark Gyorgy Fek

Independent Research

Budapest, Hungary

mindler.gergely@gmail.com, szendi.bence@gmail.com, mark.fek@gmail.com

Abstract—We detect tsunamis based on ionospheric satellite signals. The measurement of changes in the ionosphere are based on total electron content (TEC) values. The TEC values are calculated from the GPS satellites' L1 and L2, P1 and P2 signals. The TEC values are smoothed by a Kalman filter. According to historical data, the curves of the TEC values show a characteristic change when a tsunami occurs. In the current phase, we present a novel method of calculating TEC curves and we apply it on data from early 2000s.

Keywords—*tsunami detection; total electron content; GPS L1, L2, P1, P2 signals; Kalman filtering*

I. INTRODUCTION

Tsunamis have been one of the natural hazards that presented a constant threat to humanity throughout history. Tsunamis can be caused by earthquakes, landslides, volcanic activity and typhoons. Tsunamis can be characterized by the following physical quantities:

- Starting point
- Main amplitude
- Velocity
- Main direction of propagation

Current tsunami warning systems are based on earthquake warning systems. These systems have several shortcomings:

- They cannot detect all tsunamis
- They cannot detect tsunamis in time
- They cannot detect the amplitude and velocity of the tsunamis
- The amplitude of the tsunami is undetectable on the open ocean

[1] showed that tsunami genesis can be accurately modeled using high-precision GPS positioning near coastal regions.

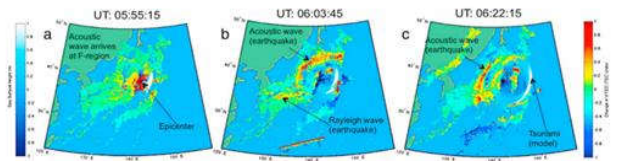


Fig. 1. The Tohoku-Oki tsunami (generated by the 2011 Japanese earthquake on the 11th of March, magnitude 9.0). Ground-based GPS ionospheric data will show earthquake generated (b) Rayleigh, (a and b) acoustic, and (c) gravity waves in the ionosphere. Source: [2].

Fig. 1 shows the Tohoku-Oki tsunami. Ground-based GPS ionospheric data indicates the presence of the tsunami.

The authors of [3] showed (see Fig. 2) that a real-time global Total Electron Content (TEC) monitoring network is able to detect the acoustic and gravity waves generated by the earthquake and tsunami.

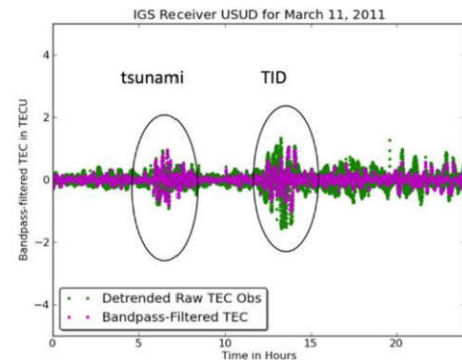


Fig. 2. The Measured and band-pass filtered TEC disturbances at Usuda (USUD) on March 11, 2011. The earthquake and tsunami-generated acoustic and gravity waves are shown around 6:00 UT and subsequent TIDs commencing about 5 hours later. Source: [3].

In this paper we present our approach to tsunami detection that is built upon the above results. In Section II, we explain how TEC measurements can be used to measure the changes of the ionosphere. In Section III we describe the objectives and planned milestones of our project. In Section IV we summarize how we calculate real-time TEC data. In Section V, we present our results on TEC calculation.

II. TOTAL ELECTRON CONTENT

The ionosphere can be characterized by Total Electron Content (TEC) values, measured using GPS signals. The TEC is defined as the number of free electrons between a receiver and satellite, within a tube with a one square meter cross sectional area.

Our research is based on GPS signal data provided by NASA. The data are collected by a network of ground-based satellite tracking stations, acting as receivers. The GPS data can be accessed publicly.

The TEC values are influenced by the position of the Sun and the latitude of the station. Natural factors, such as sunspot activity, lunar eclipses, thunderstorms and tsunamis, as well as man made factors, such as nuclear tests create disturbances in the TEC values.

III. OUR APPROACH

A. Objectives

Our goal is to calculate the TEC values in real-time, and to find the most suitable method to detect the presence and characteristics of tsunamis using the calculated TEC data. We will compare cross correlation, clustering, anomaly detection, and deep learning algorithms to evaluate their effectiveness for tsunami detection.

B. Milestones

Our project has the following milestones:

1. Real-time TEC calculation: we implement a method capable of calculating the TEC values from real time data. Our goal is to be able to calculate the TEC values within 10 minutes of delay. This would allow us to detect the appearance of tsunamis soon after the event has occurred.

2. Processing data from different sources: as a first step, we process historical GPS data provided by NASA, using the RINEX 2.0 and 2.1 format. In the second phase, we will also process RINEX 3.X files, allowing us to extend our research to the currently used satellites. In the third phase, we will process data from the Galileo, Glonass and other satellite networks.

3. Tsunami detection in a single station: we will detect the presence and characteristics of tsunamis using data from a single ground-based station.

4. Combining data from multiple stations: we determine tsunami location, amplitude and travelling direction based on multiple detections from different stations.

A. Calculation of Combined TEC Values

The TEC values can be calculated from the propagation delay of satellite signals (see Fig. 3). In case of GPS satellites, the L_1 , L_2 , P_1 , and P_2 signals can be used to measure the propagation delay, where:

- L_1 and L_2 are the data carrier waves of satellites
- P_1 and P_2 are the pseudorange measurements on L_1 and L_2 , respectively

We calculate TEC_P using the pseudorange observations P_1 , P_2 , the following way:

$$TEC_P = 9.52 \times (P_2 - P_1) \quad (2)$$

We also calculate TEC_ϕ using carrier phase observations L_1 , L_2 :

$$TEC_\phi = 9.52 \times (\phi_2 - \phi_1) \quad (3)$$

where ϕ_1 and ϕ_2 are the carrier phase observations on L_1 and L_2 respectively in distance units.

An interesting characteristic of the TEC values calculated above is that TEC_ϕ is very precise but ambiguous, while TEC_P is less precise but unambiguous. We can combine these two to obtain the precise and unambiguous TEC_{comb} , the combined TEC value, as the weighted average of TEC_ϕ and TEC_P based on a time frame. We calculate the TEC values in every 30 secs, when a satellite is in range of the station.

B. Mapping between Slanted and Vertical TEC values

The calculation above gives us the slanted TEC value, measured along the propagation path of the signal from the satellite to the receiver. We can calculate the vertical TEC value of the ionosphere using trigonometric equations, as shown in Fig. 3. The ionosphere is modeled as a single layer having a thickness of h from the ground to its highest point. Signals from the satellite enter the ionosphere at the pierce point. The signal suffers propagation delay due to the total electron content along its path in the ionosphere. The I_{slant}^i , the slanted TEC value is calculated from this propagation delay. The $I_{vertical}^i$, the vertical TEC value at the pierce point can be calculated using a trigonometric relationship between R_E , the Earth radius, h , the height of the ionosphere, I_{slant}^i , the slanted TEC value, θ_{el} , the elevation angle, and the χ angle of the signal propagation path relative to the vertical.

IV. CALCULATION OF THE TOTAL ELECTRON CONTENT OF THE IONOSPHERE

The unit of TEC is 1 TECU, defined by .

$$1 \text{ TECU} = 10^{16} \text{ electron} / \text{m}^2 \quad (1)$$

We follow the method of [4] to calculate the TEC values. The main steps the method will be presented below.

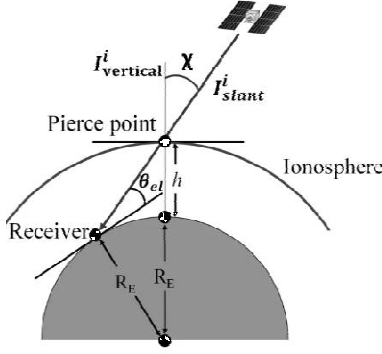


Fig. 3. GPS based calculation of the ionospheric TEC. Source: [5].

The trigonometric formula for calculating the $M(\theta_{el})$ mapping function is given below:

$$\chi = \arcsin(\cos(\theta_{el}) \times R_E / (R_E + h)) \quad (4)$$

$$M(\theta_{el}) = 1.0 / \cos(\chi) \quad (5)$$

C. Smoothing by Kalman Filter

In the next step of the calculation, we smooth the vertical TEC values using a Kalman filter. The Kalman filter can predict the TEC values using a model of linear dynamic equations. The Kalman filter combines the TEC_{pred} values with the measured TEC_{comb} values to obtain the $TEC_{filtered}$ values in such a way that the combined values tend to be more accurate than those based on a single measurement. As the algorithm is quite complex, we refer to [4] for a detailed description, including parameter values.

The Kalman filtering consist of two distinct steps. In the prediction step, the TEC_{pred} is calculated based on the inner state of the Kalman filter, along with their uncertainties. Once the outcome of the next measurement (necessarily corrupted with some amount of error, including random noise) is observed, these estimates are updated using a weighted average, with more weight being given to estimates with higher certainty. The algorithm is recursive. It can run in real time, using only the present input measurements and the previously calculated state and its uncertainty matrix; no additional past information is required.

In our approach, we run the prediction step of the Kalman filter in every 30 seconds. We run the update step in every 30 seconds, too, but only when a satellite is in range of the station. We chose the closest satellite when multiple satellites are in range.

D. The Main Formula

The calculation of the TEC value in the k^{th} iteration, at t_k , points in time, where k is the number of the iteration, which is summarized by the following formula:

$$I(t_k) = M(\theta_{el}) \times [a_0(t_k) + a_1(t_k) \times d\lambda + a_2(t_k) \times d\phi] + b^r + b^s \quad (5)$$

where $I(t_k)$ is the calculated TEC value, $a_0(t_k)$, $a_1(t_k)$, $a_2(t_k)$ are the elements of the state vector of the Kalman filter. $M(\theta_{el})$ is the mapping function at θ_{el} elevation which transforms the slanted TEC to the vertical TEC, as shown in Fig. 3. The difference between the longitude of a pierce point and the longitude of the mean sun is denoted by $d\lambda$, while $d\phi$ is the difference between the geomagnetic latitude of the pierce point and the geomagnetic latitude of the station. The latter can be calculated from the geodetic latitude by a simple formula [5]. The $d\lambda$ and $d\phi$ can be calculated as described in [5]. We use the algorithm given in [6] for calculating the position of the Sun. The last additive members of the equations are the receiver (b^r) and satellite (b^s) differential delays, representing the hardware delays occurring in the satellite and the receiver. We consider these delays to be constant within a few days. In the current implementation, we ignore b^r , as we consider only 1 station at a time. For b^s we use data available in the IONEX files.

V. RESULTS

In the first phase of the project, we created a TEC calculation algorithm. Fig. 4 below illustrates a sample run of the algorithm.

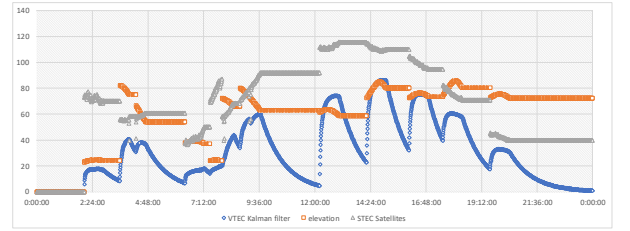


Fig. 4. Output of the TEC calculator for the Madrid station (MADR) on February 2, 2012. The curve with triangles indicates the θ_{el} elevation angle of the satellite. The curve with the squares indicates the slanted TEC_{comb} values, while the curve with the squares indicates the vertical $TEC_{filtered}$ values, i.e. the output of the Kalman filter.

We kept constant the measured slanted TEC_{comb} value, while there was no satellite in range of the station. The Kalman filter produces $TEC_{filtered}$, the smoothed version of the slanted TEC_{comb} curve. It is also scaled by the actual value of the mapping function. We can observe discontinuities in both TEC curves, when the θ_{el} elevation degree was too small. This can be attributed to the imprecision of the TEC_{comb} calculation in case of low elevation angles. In the final version of the algorithm, we will take into account measurements from a lot more satellites, allowing us to drop the data from satellites having a low elevation angle, and providing a continuous and smooth $TEC_{filtered}$ curve. This curve will be the input of the tsunami detection methods.

ACKNOWLEDGMENT

First and foremost, we thank Dr. Attila Komjathy, from NASA Jet Propulsion Laboratory, who recommended us to pursue work on TEC based tsunami detection using GPS signals and provided useful contacts to assist the research, although he may not agree with our approach and the interpretations/conclusions of this paper. We also thank Prof. Richard B. Langley and Heather Nicholson of the University of New Brunswick for their ideas and fruitful discussions on the topic.

REFERENCES

- [1] Song, Y. T., "Detecting tsunami genesis and scales directly from coastal GPS stations", *Geophys. Res. Lett.*, 34, L19602, doi:10.1029/2007GL031681, 2007.
- [2] Galvan, D. A., Komjathy, A., Hickey, M. P., Stephens, P., Snively, J., Tony Song, Y., Butala, M. D., and Mannucci, A. J., "Ionospheric signatures of Tohoku-Oki tsunami of March 11,2011: Model comparisons near the epicenter", *Radio Sci.*, vol.47, no.4, 2012.
- [3] Komjathy, A., Galvan, D. A., Stephens, P., Butala, M. D., Akopian, V., Wilson, B., Verkhoglyadova, O., Mannucci, A. J., and Hickey, M., "Detecting ionospheric TEC perturbations caused by natural hazards using a global network of GPS receivers: The Tohoku case study", *Earth, Planets and Space*, vol.64, no. 12, p24, 2013.
- [4] Komjathy, A., "Global Ionospheric Total Electron Content Mapping Using the Global Positioning System", Ph.D. thesis, University of New Brunswick, 1997.
- [5] Harris, R. B. and Mach, R. G., "The GPSTk: an open source GPS toolkit", in *GPS Solutions*, vol11., no.2, 2007, pp.145-150.
- [6] Werner, L. and Liu, A.: com.ibm.icu.impl.CalendarAstronomer Java class, ICU International Components for Unicode project, http://icu-project.org/~yoshito/jacoco_57.1/com.ibm.icu.impl/CalendarAstronomer.java.html

Quantum Tracking a Dataset

a New Application of Quantum Cryptograph

Máté Galambos

Department of Networked Systems and Services
Budapest University of Technology and Economics
Budapest, Hungary

László Bacsárdi

Department of Networked Systems and Services
Budapest University of Technology and Economics
Budapest, Hungary

Abstract—The goal of position verification is to prove that someone is telling the truth about where they are (using quantum cryptography). Theoretically we could build other cryptographic protocols based on location verification—these protocols fall under the category of location dependent quantum cryptography. One distinguishing feature of current protocols is that they use position as the only credential of a communicating party. This means that they cannot verify who or what this communicating party is or if it is the same party during repeated communication attempts. However in practice we would often like to track something (meaning we would like to repeatedly verify its position—in an environment where a potential attacker has access to its internal components.) This is not possible using current location dependent protocols. In this paper we introduce a new protocol that allows tracking a dataset. Our protocol assumes a position verification scheme that is secure under reasonable assumptions. It then uses large sequences of random qubits called a tracker. The position of the tracker can be repeatedly verified by sacrificing some separable portion of it and feeding it to the location verification protocol. Finally we suggest using some unitary operation to mix the tracker with valuable data. This unitary operation should be chosen in a way that an attacker cannot separate the valuable information from the tracker if she has access to the mixed data. The tracking also requires a sequence of other unitary operations that reveal some of the tracker bits and how to separate them from the rest of the data while keeping the rest sufficiently mixed. Sacrificing the revealed, separable portion of the tracker at each step allows us to perform the location verification.

Keywords—*position verification, quantum cryptography, tracking*

I. INTRODUCTION TO POSITION VERIFICATION

We often judge the trustworthiness of people based on where they are. For example we hand our cash and credit card over to the cashier in shops every day because we assume that only trustworthy people can be behind the cash register. Similarly a military report would be judged very differently if it came from the pentagon than if it came from a rogue state.

However telling where a message originated from is a hard task if we have a distant communication partner.

The goal of position verification is to prove that a communicating party (called the Prover) is at the geographical location where they say they are. This requires several other parties (so called Verifiers) to work together and check, and

the honest Prover to work with them and answer their questions as fast as possible. (Generally we assume that there is a secure channel between the Verifiers—however we do not assume such a channel between the Prover and the Verifiers.)

A reasonable approach to this problem would be to use physics—namely the speed of light—to verify the position of the honest Prover [1]. If one of the Verifiers asks a question from the Prover and the Prover answers it in less than T time with the speed of light, then we can give an upper bound on how far the honest Prover could be from that Verifier.

If we knew the distance from all the Verifiers at the same time we could verify the position of the honest Prover (assuming that the Verifiers surround the Prover in a sufficient configuration.) However the problem arises from making sure that it is indeed the same communicating party (the honest Prover) that answers to all the Verifiers.

We could try to solve this problem by coordinating the Verifiers. If they work together they can formulate their question in a way that the Prover can only calculate the answer (given by some function f) if he or she received the data transmitted by all of them. If the Verifiers time their questions so that their transmitted data arrives at the honest Prover simultaneously, and the required answer can be calculated in a negligibly short time, then the position of the Prover can seemingly be verified as the intersection of spheres whose radius is the distance from each Verifier.

However this approach is flawed. If several Attackers work together positioning themselves near each Verifier, then each Attacker can independently calculate the answer by listening to the question coming from all the Verifiers and sending the answer to one particular Verifier whom they are supposed to trick. The Verifiers have no way of discerning whether the answer came from one single honest Prover who is at the alleged location or from several coordinated attackers.

This means that there is no classical way of performing position verification. Note however that this attack is based on the fact that classical data can be copied arbitrarily many times (each Attacker has to receive a copy of the data transmitted by each Verifier).

This is not the case for quantum information: the so called no cloning theorem [2] [3] states that an unknown qubit (singular unit of smallest quantum information) cannot be copied. This could lead us to naively assume that quantum

location verification is secure. Although this is true against classical attacks [4] [5] we have to account for quantum attacks as well. The problem in the quantum case arises from the fact that even though there is only a single copy of a quantum bit that copy might not be localized in space. The class of attacks exploiting this are called teleportation attacks.

Without going into technical details we only mention that there is a universal teleportation attack [5] [6] that works against every quantum position verification protocol, and in some cases this is the best known attack. However this attack is grossly inefficient: the resources that the Attackers require are exponential as function of the resources required in the honest case. (Resources during the attack mean number of qubits bandwidth and computational capacity—while resources in the honest case mean the number of qubits passed between the honest Prover and Verifiers and therefore bandwidth.)

The consequence of this is that some quantum protocols are thought to be secure under the following conditions: a) the Attackers have bounded resources and b) it is possible to use sufficiently large sequences of qubits in the honest case.

(Note however that at this point there is no proof that there are protocols in which case the universal attack is optimal—it is simply the best *known* attack so far in some cases. However in the following part of the paper we are going to assume that the general conclusion holds: that there is some position verification protocol in which case the all attacks can be prevented if the verification uses sufficiently large amount of qubits and the Attackers have limited resources.)

II. LOCATION DEPENDENT CRYPTOGRAPHY

Several new protocols can be based on position verification. For example if position verification is possible then it is also possible to construct a bit commitment scheme [7] that relies on it, which in turn can serve as the basis for coin tossing between mistrustful parties, digital signature, oblivious transfer and two-party secure computation [7].

However the goal of position verification is nothing more than to authenticate the location of a distant communicating party. In essence it uses the location as the *only* credential of this party—we do not care who sits behind the bullet proof glass at a bank or who sent the order from the Pentagon. The very fact that they can enter these secure locations means they are trustworthy.

This approach may be useful in certain cases however it limits other use cases—like tracking something. In essence tracking would mean that we have to repeatedly verify the location of some object but with position verification nothing ensures that it is the same object whose position we keep verifying.

A notable exception from this can be found in [8]. However that protocol assumes that the tagging device that we are tracking cannot be opened and examined by an attacker. This is a strong restriction which is not necessarily realistic.

III. USING RANDOM DATA AS A TRACKER

This section introduces the concept of tracking random data. In the next section we will expand on the concepts introduced here and examine how to mix some valuable data with the random data and track the mixture of the two.

To track data first we have to fill a quantum memory with random data $|Q\rangle$. This random data is kept secret and it's only known by the Verifiers. It should be sufficiently large to be impervious to a general teleportation attack and it should also be in a state that is protected by the no-cloning theorem against classical attacks.

From now we are going to refer to this random data $|Q\rangle$ as a tracker. We can trace the movements of the tracker by repeatedly splitting it to a bigger and smaller part, and using the smaller $|q'\rangle$ portion to perform the position verification (while keeping the bigger $|Q'\rangle$ portion to serve as the tracker for the next round.)

The details of this process are described below:

Step 1.: The honest Prover who carries the quantum memory announces his or her position, speed and heading. The Verifiers receive this message and calculate how long it would take for a signal that propagates at the speed of light to reach the Prover's position from their location.

Step 2.: The Verifiers coordinate amongst themselves and choose a suitable moment when they issue a question to the Prover. This question takes the form of some unitary operation U , and some additional instructions necessary to perform the position verification. The purpose of this U operation is to split the tracker.

Therefore this U operation must be chosen in a way that performing U on the tracker produces two separable states: one smaller qubit string $|q'\rangle$ (that is still sufficiently long to be resistant to a general teleportation attack) and a longer random qubit string $|Q'\rangle$ (that will serve as the tracker for the next round of the protocol).

$$U|Q\rangle = |Q'\rangle \otimes |q'\rangle \quad (1)$$

There are some further considerations for choosing U : First of all U must produce the two $|Q'\rangle$ and $|q'\rangle$ qubit strings in such a way that they remain protected from attacks. This means that they should be long enough, remain unknown to anyone except the Verifiers and remain in a state that prevents classical attacks.

Secondly U must be an operation that can be performed virtually instantaneously (so that it doesn't interfere with the position verification).

Thirdly $|q'\rangle$ (and therefore U) must be hard to predict. U should be randomly selected from a large number of candidate U_c operations that produce sufficiently different $|q'_c\rangle$ states to ensure security. Naturally the different U operations throughout the different iterations should be chosen independently and with great care. (Remember that $|q'_c\rangle$ depends not just on U_c , but on $|Q\rangle$ as well. Just because U_c candidates produce different $|q'_c\rangle$ states in one particular iteration does not automatically mean that they will produce different ones in the next iteration.)

Fourthly whenever a random choice has to be made the random number generators producing that choice must be cryptographically secure.

And finally, the Verifiers must be able to efficiently update their knowledge about the tracker in light of U .

Step 3.: The Verifiers transmit their question in such a way that the Prover have to know the messages sent by all Verifiers to perform the operation U .

Step 4.: The honest Prover receives the question, performs the operation U . He or she then executes the position verification as instructed, sacrificing $|q'\rangle$ in the process. The Prover then sends an answer to the Verifiers.

Step 5.: The Verifiers receive the answer and verify that the honest Prover is indeed at the position where he or she claims to be.

At this point the protocol can be iterated repeating the steps from step 1 until the entire tracker is used up (meaning that $|Q'\rangle$ becomes too small and therefore it is no longer protected against a general teleportation attack.)

This means that the position of the tracker can only be verified a finite amount of times, and the tracker is progressively used up in the process.

As an additional remark: here we assume that all qubits of $|Q\rangle$ are necessary to compute $|q'\rangle$. This however is not necessarily the case. Using only a subset of the tracker's qubits may reduce the necessary computational power, and therefore the time to perform U . However the drawback of this approach is that it weakens security: if some of the qubits are removed from $|Q\rangle$ and they happen to be the ones that are not required to compute $|q'\rangle$, then the alteration remains undetected during that round of the position verification.

IV. MIXING VALUABLE DATA WITH A TRACKER

As we saw in the previous section the tracker is progressively used up during the repeated verification iterations. This means that valuable data should not be used as a tracker. In this section we are going to introduce the concept of mixing valuable data with a tracker. During the tracking only the tracker will be used up.

In this case before we start the iterations there should be some preparation.

Step 0.1.: The valuable data $|D\rangle$ should be encrypted as $|D'\rangle$ and stored in a quantum memory. The rest of the memory should be filled with random qubits $|R\rangle$. The encryption should be chosen in a way that the encrypted random data $|D'\rangle$ is indistinguishable from random qubits. (Otherwise if there is sufficient pattern in the encrypted valuable data $|D'\rangle$ to distinguish it from the tracker, an attacker might be able to separate the tracker from the valuable data.)

Step 0.2.: The Verifiers should choose a secret V_0 unitary operation that mixes the encrypted valuable data and the tracker.

$$V_0(|D'\rangle \otimes |R\rangle) = |Q\rangle \quad (2)$$

This should be done in a way that only the Verifiers know how to restore the valuable data from $|Q\rangle$.

From here the tracking protocol continues similarly to what has been introduced in section III. The only difference is that U must be chosen in a way that preserves the integrity of the valuable data.

Step 1.: The honest Prover announces his or her position, speed and heading. The Verifiers calculate the response time assuming communication with the speed of light.

Step 2.: The Verifiers coordinate amongst themselves and choose a unitary operation U , and some additional instructions necessary to perform the position verification. The purpose of this U operation is to split some bits of the tracker off from the rest of the data:

$$U|Q\rangle = |Q'\rangle \otimes |q'\rangle \quad (3)$$

U must be chosen in a way that addresses the proper security concerns and speed requirements. (See section III.)

Additionally U must be chosen in a way that the Verifiers are able to compute a unitary operation V^{-1} that makes it possible to restore the encrypted valuable data $|D'\rangle$ from $|Q'\rangle$:

$$V^{-1}|Q'\rangle = |D'\rangle \otimes |R'\rangle \quad (4)$$

where $|R'\rangle$ represents the unused tracker qubits.

Generally this V^{-1} will be different during each iteration and it should be sufficiently hard to guess for an attacker every time.

Step 3.: The Verifiers transmit their question.

Step 4.: The honest Prover receives the question, performs the position verification as instructed, sacrificing $|q'\rangle$ in the process.

Step 5.: The Verifiers receive the answer and verify the position.

The protocol can be iterated repeating the steps from step 1 until the entire tracker is used up, or it becomes necessary to separate the tracker from the valuable data. At that point the Verifiers reveal V^{-1} .

V. CONCLUSIONS

In this paper, we present a method for tracking a dataset. This method is based on position verification and assumes that there exists a position verification scheme that is secure against an attacker with limited capabilities if the number of qubits used for the verification is large enough.

Based on this assumption, we suggest mixing encrypted valuable data with a random tracker. Position verification can be repeatedly performed by splitting off some part of the tracker and performing the position verification with the resulting qubits.

The position can be verified over and over until either the tracker is completely used up or the encrypted valuable data is restored.

REFERENCES

- [1] N. Chandran, V. Goyal, R. Moriarty and R. Ostrovsky, "Position Based Cryptography," in *Advances in Cryptology - CRYPTO 2009*, Heidelberg, 2009.
- [2] W. K. Wootters and W. H. Zurek, "A single quantum cannot be cloned," *Nature*, vol. 299, no. 5886, pp. 802-803, 1982.
- [3] D. Dieks, "Communication by EPR devices," *Phys. Lett. A*, vol. 92, no. 6, pp. 271 - 272, 1982.
- [4] A. Kent, W. J. Munro and T. P. Spiller, "Quantum tagging: Authenticating location via quantum information and relativistic signaling constraints," *Phys. Rev. A*, vol. 84, no. 1, p. 012326, 2011.
- [5] H. Buhrman, N. Chandran, S. Fehr, R. Gelles, V. Goyal, R. Ostrovsky and C. Schaffner, "Position-Based Quantum Cryptography: Impossibility and Constructions," *SIAM J. Comput.*, vol. 43, no. 1, p. 150-178, 2013.
- [6] S. Beigi and R. König, "Simplified instantaneous non-local quantum computation with applications to position-based cryptography," *New J. Phys.*, vol. 13, no. 9, p. 093036, 2011.
- [7] M. Nadeem, "Unconditionally secure commitment in position-based quantum cryptography," *Scientific Reports*, vol. 4, p. 6774, 2014.
- [8] A. Kent, "Quantum tagging for tags containing secret classical data," *Phys. Rev. A*, vol. 84, no. 2, p. 022335, 2011.

Exploitation of Sentinel-1 SAR data for studying geodynamic, tropospheric and ionospheric processes

István Bozsó, Eszter Szűcs, László Bányai, Viktor Wesztergom
 MTA CSFK Geodetic and Geophysical Institute
 Sopron, Hungary
 bozso.istvan@csfk.mta.hu

Abstract—Radar images acquired by space-borne SAR (Synthetic Aperture Radar) instruments have been used extensively by the scientific community for biomass estimation, surface deformation mapping and monitoring, land cover classification, flood mapping in the last twenty years. The availability of SAR scenes, however, was limited until the launch of the Sentinel-1 A and B satellites in 2014 and 2016, that ushered in a new age of SAR remote sensing, thanks to the open access data policy of the Copernicus Earth Observation Program of the EU. Sentinel-1 IWS (Interferometric Wide Swath) SAR acquisitions provide wide area coverage and ensure short revisit times (6 days in Europe, 12+ days outside of Europe). One of the main usages of SAR images is the interferometric processing, that yields so-called interferograms that contain the phase differences between two SAR scenes. The interferometric phase is the combination of different phase terms including surface deformation (if present), atmospheric, ionospheric, topographic, noise. The accurate estimation and separation of these terms allow the analysis of the (geo)physical and geodynamic processes related to the origin of the phase components.

We wish to demonstrate that it is possible to separate the aforementioned phase components and use the resulting phase to study geodynamic and atmospheric phenomena such as landslide evolution (with the help of corner reflectors), large scale surface deformation trends in the Transylvanian Basin, change of water vapour content in the atmosphere and ionospheric electron content variations.

Keywords—InSAR; remote sensing; earth observation; geodynamics; atmosphere monitoring

I. INTRODUCTION

Synthetic Aperture Radar (SAR) images acquired by ground-based instruments, airplanes and satellites can be processed and utilized to carry out different kinds of analysis. The SAR antenna on the platform transmits electromagnetic (EM) microwave signal and detects the returned signal reflected from the target object(s). The product of raw data processing is a focused, so-called Single Look Complex (SLC), image that possesses excellent spatial resolution (20 m × 5 m sized pixels are typical in the case of Low Earth Orbit C-band (5.405 MHz) SAR satellites) and contains the amplitude and phase of the reflected signal using complex numbers.

An interferogram can be formed by subtracting the phase of a so-called slave SLC from a reference (master) SLC

(multiplying the complex pixels of the master SLC with the complex conjugate of the slave pixels). The resulting interferometric phase is a combination of multiple phase terms:

$$\Phi_{\text{IFG}} = \Phi_{\text{defo.}} + \Phi_{\text{atmo.}} + \Phi_{\text{topo.}} + \Phi_{\text{orbit}} + \Phi_{\text{noise}} \quad (1)$$

where

- Φ_{IFG} is the phase of the interferogram,
- $\Phi_{\text{defo.}}$ is the phase caused by surface deformation, that occurred between the two SAR acquisitions, in the Line-of-Sight (LOS) direction,
- $\Phi_{\text{atmo.}}$ is the phase caused by the change in atmospheric microwave propagation speed,
- $\Phi_{\text{topo.}}$ is the phase due to topography,
- Φ_{orbit} is the phase from errors of the orbital state vector,
- Φ_{noise} is noise from residual phase terms, that cannot be modeled.

In order to investigate the underlying physical processes that cause the emergence of different phase terms, the terms themselves have to be separated. This can be done using atmospheric models to calculate $\Phi_{\text{atmo.}}$, low- or high-pass filtering in time and/or space and other methods. Once the separate phase terms are estimated adequately, phase unwrapping [1,2] (i.e. the determination of integer number phase cycles, which added to the wrapped phase yield the continuous unwrapped phase) needs to be carried out.

Let's assume that all the phase terms except $\Phi_{\text{defo.}}$ are eliminated somehow using assumptions or external data sets then the surface displacement can be calculated from the unwrapped deformation phase as follows:

$$d_{\text{defo.}} = (\lambda / 4 \pi) \Phi_{\text{defo., unwrapped}} \quad (2)$$

where λ is the wavelength of the radar wave.

Using multiple interferograms formed from multiple SLC images it is possible to reconstruct the phase deformation history of the area that is covered by the SLC images and calculate the mean LOS deformation velocity of each pixel.

The methods that are related to such kind of processing are collectively called InSAR (interferometric SAR) processing (methods).

In the following section the SAR datasets that were used and the processing strategies employed to derive surface displacement time-series, mean surface velocities, integrated water vapor (IWV) and ionospheric Total Electron Content (TEC) variations will be presented.

II. PROCESSING OF SAR DATASETS AND THE DESCRIPTION OF RESULTS

A. Mapping surface displacement based on natural scatterers

Sentinel-1 offers the determination of deformation data at a far greater level of granularity compared to traditional geodetic techniques. The frequent revisit time of the twin satellites enables the user to capture the dynamics of the ongoing processes. To demonstrate the performance of Sentinel-1 radar interferometry in deformation monitoring some preliminary results related to our lithosphere dynamics project are presented. The project aims for the observation and modeling one of the tectonically most interesting part of the European lithospheric plate, the Carpathian subduction. Several geodynamical processes are ongoing here: active seismicity, volcanism associated with the subduction, significant gas emanations of post volcanic activity and salt tectonics influenced by the increase of heat flow of volcanism and seismicity.

Our first results are based on Sentinel-1 [3] SAR scenes (S1A descending track, 105 scenes, multi-baseline processing) covering 3.5 years, shown in Fig. 1. and Fig. 2., clearly shows the deformation of the largest salt extrusion (Praid). The salt bodies in the southern part of the salt extrusion show motion away from the satellite at rates of 3-4 cm/yr. The deformation of surface salt is governed by the change of its physical parameters (viscosity) which is influenced by local weather conditions (meteoric water, variation of temperature). Detecting tectonically related tiny deformations – shaking due to earthquakes – requires highly reliable scatterers which are lacking especially in northern part of the salt dome, where no phase-stable natural scatterer was identified. Artificial benchmarks (see next section) can remedy this obstacle.

B. Monitoring the displacement time-series of benchmark reflector networks

Several reflector networks were deployed in Hungary to investigate the surface displacements of a certain area of interest where beforehand InSAR measurements have failed to properly estimate surface displacement time series. These networks are made up of 4 or 5 previously mentioned artificial radar reflector benchmarks. Each benchmark contains two reflectors oriented towards the ASC and DSC satellite LOS directions and an adapter for GNSS and leveling measurements. Sentinel-1 A and B [3] ascending and descending SAR acquisitions were processed covering the network, located at a settlement (Dunaszekcső) along the loess banks of the River Danube. A single benchmark with the GNSS receiver can be seen in Fig. 3. The reflectors were located inside the SAR images and their ascending and

descending line-of-sight (LOS) deformation time-series were derived and combined with GNSS measurements using Kalman filtering [4] to estimate 3D surface displacement time-series.

The resulting 3D time-series can be seen in Fig. 4. The deformations are relative to a single reference reflector benchmark (IB1). The 3 moving reflectors (IB2, IB3, IB4) show a very similar deformation pattern. All 3 benchmarks are subsiding and moving eastward with roughly the same vertical deformation rate. The eastward motion almost halts from the start of 2017 for approximately 3 months. This pause in motion can be most likely attributed to the weather of the winter season.

C. Estimation of Integrated Water Vapor maps using InSAR

Several SAR scenes covering the Dunaszekcső network were processed to calculate integrated water vapor values (IWV). For the calculation of IWV values it was assumed that the covered area was not affected by deformation (except for the area affected by landslide movements) and that the contribution of pressure and temperature profile changes to the change in EM wave propagation velocity was negligible.

Since InSAR can only measure differences in surface position, atmospheric EM wave propagation velocity, an additional constraint is needed to calculate the absolute values. In the case of IWV estimation this constraint was provided by the ECMWF ERA-Interim (ERA-I) [5] weather model.

First the average zenith wet delay (ZWD) was calculated at the model grid points, then the ZWD values were projected onto the LOS direction (slant-range) and interpolated to the positions of the SAR pixels. This processing step was carried out for all SAR scene acquisition dates using the ERA-I model. Finally the temporal average of the slant-range wet delay (SWD) values were computed and used as a constraint for the calculation of absolute wet delays at every SAR pixel. The resulting SWD values were projected back into the zenith direction (converting them into ZWD values) and IWV values were estimated using the following equations:

$$ZWD / IWV = 10^{-8} (k_2 - (R_d / R_w)k_1 + (k_3 / T_m)) R_w \quad (3)$$

$$T_m = 70.2 + 0.72 T_s \quad (4)$$

where

- T_s is the surface temperature,
- R_d , R_w , k_1 , k_2 and k_3 are experimental constants [6, 7 8].

Equation (3) was derived by Saastamoinen [9] and (4) by Bevis et al. [10].

The preprocessing of the SAR images was done by the Gamma software [11] and the time-series analysis by the StaMPS software [12] both in the case of reflector deformation monitoring and the IWV estimation.

The estimated IWV values can be seen in Fig. 5. The IWV values mainly contain large wavelength components which are

only disturbed by high frequency components in the case of the first date (Fig. 5.1. - 2016.12.05.). These components may be the result of a turbulent region, that was present in the troposphere when the SAR image was taken.

D. Calculation of slant range ionospheric TEC differences

The Earth's ionosphere is a dispersive medium for EM waves, the propagation delay depends on its frequency. Using two carrier frequencies in GNSS enables to estimate the phase delay. A similar approach can be used for SAR systems by filtering the phase to create interferograms of spectral sub-bands (split-beam technique, Meyer et al. [13], Gomba et al. [14]). Ionospheric phase delay is inversely proportional with frequency, therefore its effect is more pronounced for low-frequency L-band (20 cm wavelength) systems. Based on a previous publication of Wegmüller et al., 2018 [15], where the authors describe a new method for calculating the ionospheric phase from SLC SAR scenes, acquired by the PALSAR-1 satellite, we have carried out calculations described in the article to estimate the ionospheric phase component of the interferogram.

Using the ionospheric phase we derived the TEC change between the two scenes (2009.03.28.–2009.06.28.) as described in Meyer et al., 2006 [13]:

$$\Phi_{\text{iono}} = [(4\pi K) / (cf_0)] \Delta\text{TEC} \quad (5)$$

where

- Φ_{iono} is the ionospheric phase,
- $K = 40,31 \text{ m}^3\text{s}^{-2}$ is a constant,
- c is the speed of light in vacuum,
- f_0 is the radar center frequency (1270 MHz in the case of PALSAR-1) and
- ΔTEC is the slant range TEC change between two SAR scenes.

We applied the processing steps using the Gamma software [11].

The estimated ΔTEC values are presented in Fig. 6. The span of the TEC changes is approximately in the reasonable 1 TECU range ($1 \text{ TECU} = 10^{16} \text{ electron} / \text{m}^2$) from -0.8 to 0.2 TECU. The ΔTEC values appear to be somewhat correlated with topography which may be a deterministic effect, similarly to how the non-dispersive tropospheric phase term can be correlated with topography.

III. DISCUSSION

The previous four examples demonstrate that space-borne SAR interferometry can be used for a wide variety of applications. The main use for Sentinel-1 A and B images is the monitoring and mapping of surface deformation caused by natural and anthropomorphic processes. It is also possible to derive quantities of different atmospheric variables (water vapor, pressure, temperature, electron content) integrated in satellite slant-range and projected the unto to vertical direction.

Although Sentinel-1 SAR images are less sensitive to ionospheric effects than PALSAR-1 scenes, due to the difference in carrier frequencies, the method described in Wegmüller et al., 2018 [15], can be used to reliably estimate the ionospheric phase term caused by TEC changes in the upper atmosphere and provide long-term time-series of vertical TEC changes covering large areas. These additional atmospheric quantities enable the long term analysis of the troposphere–ionosphere system and possibly uncover the nature of their interactions.

ACKNOWLEDGMENT

Contains modified Copernicus Sentinel data 2014-2018, processed by ESA.

This study was supported by the TopoTransylvania - a multidisciplinary Earth science initiative in Central Europe to tackle local and global challenges project (NKFI NN 128629).

REFERENCES

- [1] Goldstein, Richard M., Howard A. Zebker, and Charles L. Werner. "Satellite radar interferometry: Two dimensional phase unwrapping." *Radio science* 23.4 (1988): 713-720.
- [2] Chen, Curtis W., and Howard A. Zebker. "Two-dimensional phase unwrapping with use of statistical models for cost functions in nonlinear optimization." *JOSA A* 18.2 (2001): 338-351.
- [3] Torres, Ramon, et al. "GMES Sentinel-1 mission." *Remote Sensing of Environment* 120 (2012): 9-24.
- [4] Kalman, Rudolph Emil. "A new approach to linear filtering and prediction problems." *Journal of basic Engineering* 82.1 (1960): 35-45.
- [5] Dee, Dick P., et al. "The ERA Interim reanalysis: Configuration and performance of the data assimilation system." *Quarterly Journal of the Royal Meteorological Society* 137.656 (2011): 553-597.
- [6] Smith, Ernest K., and Stanley Weintraub. "The constants in the equation for atmospheric refractive index at radio frequencies." *Proceedings of the IRE* 41.8 (1953): 1035-1037.
- [7] Laurila, S. H. "Statistical analysis of refractive index through the troposphere and the stratosphere." *Bulletin Géodésique (1946-1975)* 92.1 (1969): 139-153.
- [8] Thayer, Gordon D. "An improved equation for the radio refractive index of air." *Radio Science* 9.10 (1974): 803-807.
- [9] Saastamoinen, J. "Atmospheric correction for the troposphere and stratosphere in radio ranging satellites." *The use of Artificial Satellites for Geodesy* 15 (1972): 247-251.
- [10] Bevis, Michael, et al. "GPS meteorology: Remote sensing of atmospheric water vapor using the Global Positioning System." *Journal of Geophysical Research: Atmospheres* 97.D14 (1992): 15787-15801.
- [11] Werner, Charles, et al. "Gamma SAR and interferometric processing software." *Proceedings of the ERS-Envisat Symposium, Gothenburg, Sweden*. Vol. 1620. 2000.
- [12] Hooper, Andrew, et al. "Recent advances in SAR interferometry time series analysis for measuring crustal deformation." *Tectonophysics* 514 (2012): 1-13.
- [13] Meyer, Franz, et al. "The potential of low-frequency SAR systems for mapping ionospheric TEC distributions." *IEEE Geoscience and Remote Sensing Letters* 3.4 (2006): 560-564.
- [14] Gomba, Giorgio, et al. "Toward operational compensation of ionospheric effects in SAR interferograms: The split-spectrum method." *IEEE Transactions on Geoscience and Remote Sensing* 54.3 (2016): 1446-1461.
- [15] Wegmüller, Urs, et al. "Reformulating the Split-Spectrum Method to Facilitate the Estimation and Compensation of the Ionospheric Phase in SAR Interferograms." *Procedia computer science* 138 (2018): 318-325.

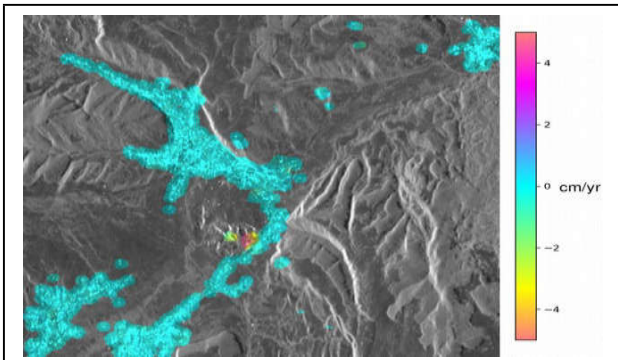


Fig. 1 Mean displacement velocities in radar coordinates, derived from Sentinel-1 SAR scenes, near the settlement of Praid in Transylvania. Significant movements can be discovered at the flanks of the salt dome.

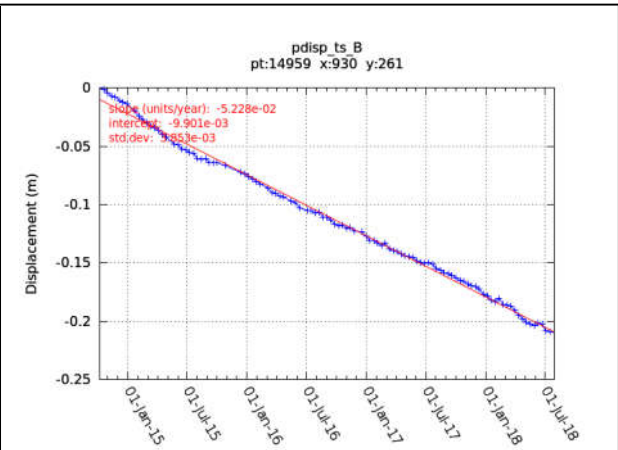


Fig. 2. Line-of-sight deformation time-series of a selected pixel, located on the flank of the Praid salt dome. The deformation is dominated by a linear signal with the mean displacement velocity of -5 cm/yr.



Fig. 3. View of a single reflector benchmark with the GNSS adapter emplaced on the subsiding loess bank, near the settlement of Dunaszekcső with the River Danube in the background.

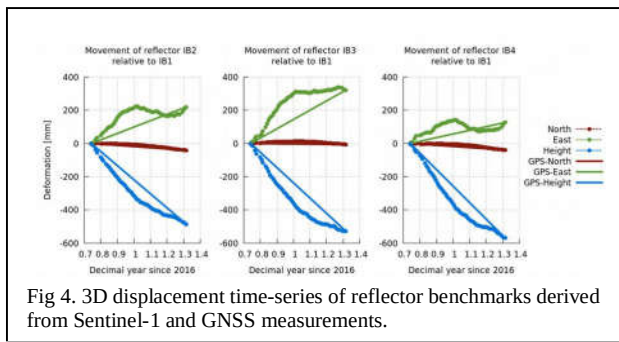


Fig 4. 3D displacement time-series of reflector benchmarks derived from Sentinel-1 and GNSS measurements.

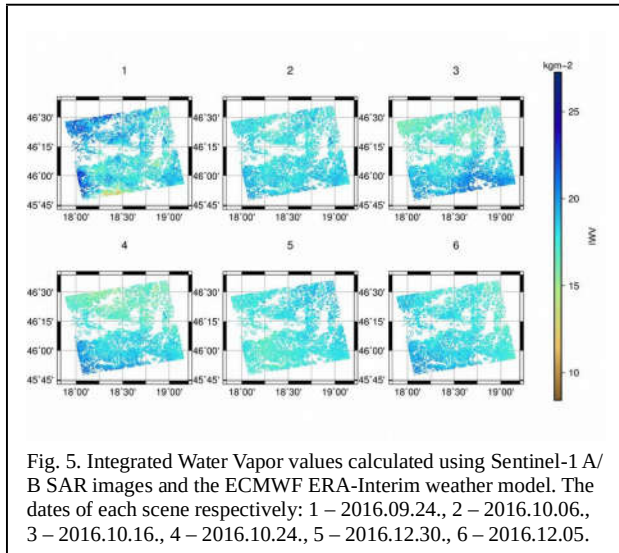


Fig. 5. Integrated Water Vapor values calculated using Sentinel-1 A/B SAR images and the ECMWF ERA-Interim weather model. The dates of each scene respectively: 1 – 2016.09.24., 2 – 2016.10.06., 3 – 2016.10.16., 4 – 2016.10.24., 5 – 2016.12.30., 6 – 2016.12.05.

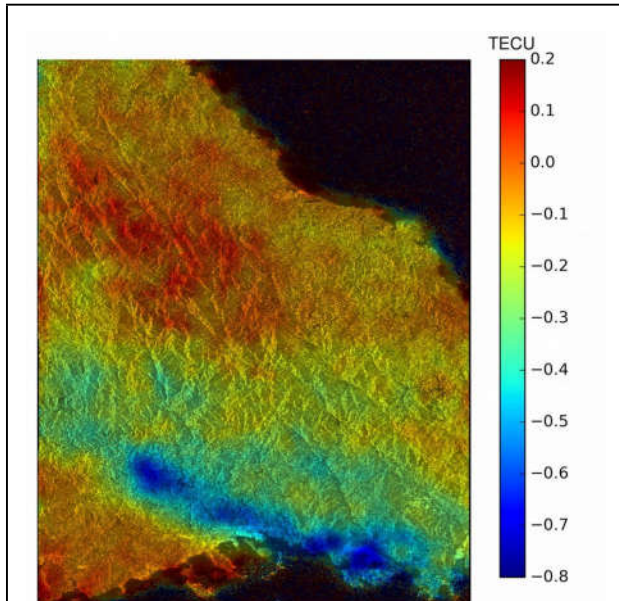


Fig. 6. Total Electron Content (TEC) changes between 2009.03.28. and 2009.06.28. derived from PALSAR-1 images, created above the Yamagochi Prefecture Japan. The TEC changes are relative to the upper left corner of the SAR scene. The TEC change values are in TECU units, 1 TECU = 10¹⁶ electron / m². The grayscale background image is the SAR backscatter intensity image of the 2009.03.28. scene.

Investigation of stochastic disturbances in satellite connected terrestrial millimetre wave wireless mesh network

János Z. Bitó

Department of Broadband Infocommunications and Electromagnetic Theory,
Budapest University of Technology and Economics
Budapest, Hungary
bito@hvt.bme.hu

Abstract—Monitoring network performance makes it possible to give an estimation or prediction on future runoff of the disturbing effects, so that these effects can be eliminated to a certain degree. This study investigates a moving interference source disturbing a terrestrial millimetre wave mesh network of 5G nodes where some of the nodes have also satellite connection. The goal is to investigate prediction possibilities of these disturbing effects, keeping an eye on the fact that it is possible to prepare the network for known disturbances, and with that it is possible to decrease energy consumption of the network.

Keywords— *Satellite links, millimetre wave terrestrial mesh, green communication*

I. INTRODUCTION

The radio spectrum below 6 GHz is almost fully occupied and will be further saturated by increasing number of IoT devices of 5G systems. Cognitive radio (CR), whose first concept was proposed in [1], is one of the most important emerging technologies to solve these problems. The primary users or incumbents in a CR system are the main owners of the spectrum. To avoid interference with the primary system secondary or opportunistic users are utilizing the free or unused resources in the CR environment, taking into consideration that the quality of service of the incumbents cannot be degraded [2]. However, if there are one or more non cooperating interference sources as secondary users of the same radio spectrum the quality of service (QoS) of the primary system cannot be guaranteed without applying appropriate techniques to reduce and/or avoid these disturbances. Such techniques includes interference elimination methods like successive [3, 4] or parallel interference cancellation (SIC or PIC) or other methods keeping the required signal to interference and noise ratio (SINR) for example by power adaptation of the transmitters of the primary system.

The primary system under consideration in this contribution is a satellite connected millimetre wave terrestrial mesh network of access points (nodes) providing broadband content to the users of fifth generation (5G) mobile systems. Satellite

links to the nodes can be used for providing broadband content of global interest cashed by the nodes whereas the terrestrial millimetre wave links distribute instantaneous information of local interest, therefore guarantying low latency for end users.

This contribution deals with a moving interference source as secondary user disturbing a primary system of dense millimetre wave terrestrial mesh network where all or some of the nodes have also satellite connection. This incumbent configuration has high potential in 5G, because the densely deployed nodes are access points (base stations) for broadband services.

Beside backhauling the 5G millimetre wave wireless mesh network can also be obtained as a sensor network. Any kind of stochastic disturbance for example a randomly moving interference source like a non-cooperating secondary user of the same spectrum in the area of the mesh cause SINR degradations at the nodes that are correlated in space and time, therefore theoretically allowing the detection and prediction of the disturbing effect. Using the gathered data (for example SINR values at the mesh receivers) an appropriate method (e.g. AI) for prediction of the influence of the disturbing effect could be applied. With proper prediction of the power of interfering signal it is also possible to decrease energy consumption of the mesh network through transmit power adaptation fulfilling the goal of green communication.

The rest of the paper are organized as follows: Section II describes the concept of investigated primary system detailing the broadband content distribution method applying point-to-multipoint (PtM) communications as in satellite broadcasting as well as point-to-point (PtP) connections building a millimetre wave mesh of 5G nodes simultaneously. Wave propagation assumptions and interference source model description are given in section III, while SINR prediction methods are described in section IV. Sections V introduce preliminary simulation results followed by concluding remarks in section VI.

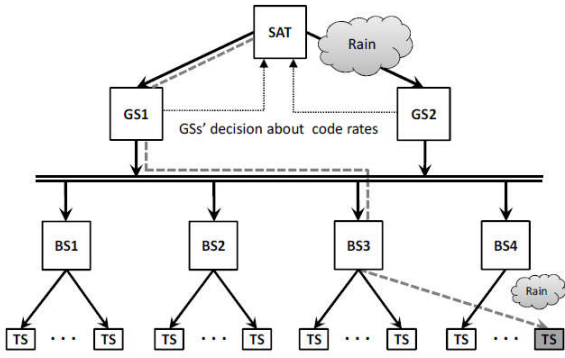


Fig. 1. System architecture of Satellite Backbone Network for BFWA Systems and logical connections in the network in the case of Earth-space link diversity and BFWA diversity [5].

II. SYSTEM CONCEPT

In 5G concept the main goal is to build a smart, scalable and flexible self-organising content delivery system that is capable to combine PtM multicast and broadcast together with PtP unicast, and caching services to provide content to the end users of the data including not only human persons but also IoT devices, machines, vehicles, etc.

The investigated primary system in this contribution consist of two main part, a satellite broadcast component providing broadband multimedia content of common interest through PtM type additional backbone of the second, terrestrial part of the system. The terrestrial part of the investigated primary system consists of PtP connected millimetre wave wireless mesh of access points (nodes) of the 5G system.

The main goal of this contribution is to investigate and predict the influences caused by a non-cooperating terrestrial secondary user stochastically disturbing the primary system.

A. Satellite Broadcast

The concept of the investigated primary system architecture has some similarities with the architecture of broadband fixed wireless access (BFWA) system with satellite backbone network investigated in our previous work [5] and depicted in Fig. 1. The main difference between the two systems is in terrestrial part; instead of the base stations (BS) of a BFWA network some of the access points (nodes) of a 5G millimetre wave wireless terrestrial mesh network are connected to the ground segment of the satellite broadcasting system providing broadband content of common interest.

By large number of users and/or IoT devices of common interest point to multipoint (PtM) broadcasting the same multimedia content, emergency messages and software updates, etc. has the significant advantage compared to the point to point (PtP) delivery system because the enormous reduction in system resource requirements (e.g. occupied spectrum, frequency reuse) due to the absence of interferences between PtP links [6].

It was stated by several players in Next Generation Mobile Network (NGMN) 5G Initiative that broadcast should be considered as an important part of the future 5G networks [7]. In addition to the traditional terrestrial or satellite PtM services like broadcasting television and/or radio (e.g. digital audio

broadcast, DAB) 3GPP already extend the PtM potentiality of 4G LTE by adopting the concept of enhanced Multimedia Broadcast Multicast Service (eMBMS) [8]. PtM broadcast and multicast could also be an important enabler for flexible and cost effective content delivery system in the new 5G radio access and core networks providing not only broadband multimedia services to the end users of common interest, but eMBMS is also foreseen for vehicular and IoT devices as well as for machine type communications.

Services like software or operating system updates of immense number of the same type of IoT devices, live and linear multimedia content such as running commentary of sport events with additional virtual reality content delivery to the massive number of viewer's 5G smartphones implies the advantages of PtM broadcasting, multicasting instead of PtP unicast. In media and entertainment sector the advantage of PtM in contrast to PtP will be further immensely increased when virtual and augmented reality (VR/AR), ultra-high-definition television (UHDTV), 360-degree video content should be provided.

B. Terrestrial millimetre wave wireless mesh

The trend of rapidly growing demand for mobile data continues for many years, therefore it is clear that future mobile networks (such as 5G) in urban areas will have to employ very small cells and much higher frequencies. When radio propagation issues will be overcome at millimeter wavelength frequencies then the available bandwidth could increase by several orders of magnitude, while there are large chunks of millimeter wavelength spectrum parts which could be allocated for cellular use.

Flexible backhauling over a mesh network would provide a very promising and cost efficient candidate for supplying the densely deployed small cell stations (nodes) and connect them to the core network. In our investigated primary system the terrestrial part consists of PtP connected millimetre wave wireless mesh of access points (nodes) of the 5G system.

The main goal is to investigate the reliability (measured by the average ratio of the disconnected nodes) of a millimeter wave backhauling mesh network that is foreseen in 5G systems. Node disconnection can occur due increasing interference level and/or additional attenuation caused for example by precipitation, especially by rain.

In the investigated scenario the non-cooperating opportunistic user are mobile devices that are utilizing the same spectrum as the incumbents and therefore causing interference. The incumbents in the investigated system are the transceivers of a millimetre wave mesh network.

For simplicity reason free space propagation conditions are assumed in a built in (urban) area with line of sight (LOS) conditions between the components of the millimetre wave mesh network considering as incumbent system as depicted in Fig. 2. Also in this figure the random route of the interfering source is depicted with blue line assuming a street model like the Manhattan model.

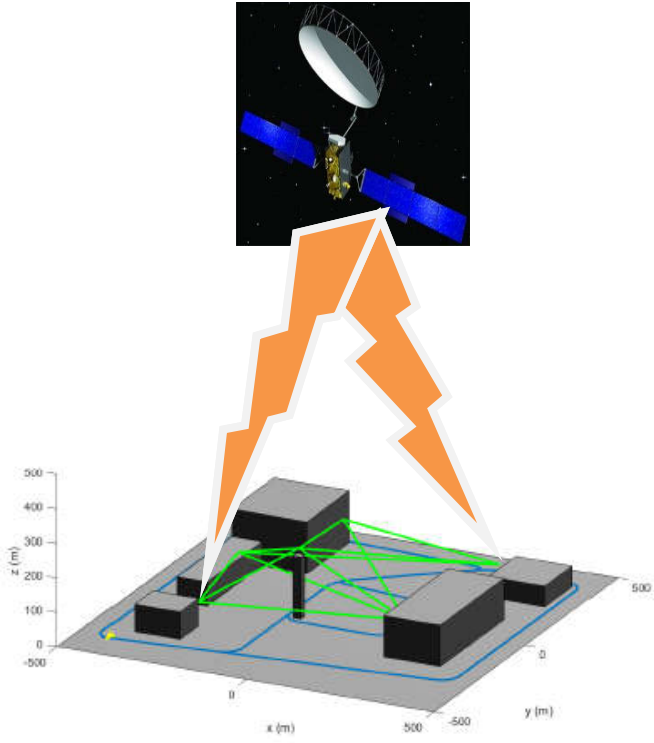


Fig. 2. Satellite PtM broadcasting and terrestrial wireless PtP mesh (green lines) as incumbent primary system and a moving (blue route) interference source as a non-cooperating opportunistic user of the same spectrum in a built in area

III. WAVE PROPAGATION AND INTERFERENCE ASSUMPTIONS

A. Propagation assumptions

Free space propagation is assumed, where the path attenuation can be expressed as the function of path length D , wavelength λ and the transmitter and receiver antenna gains, G_T and G_R :

$$a_{path}^{[dB]} = 20 \log_{10} \frac{4\pi D}{\lambda} - G_T^{[dB]} - G_R^{[dB]} = 32,44 + 20 \cdot \log_{10} f^{[MHz]} + 20 \log_{10} D^{[km]} \quad (1)$$

The interfering radio sources are taken into account with their contribution to the local received radio power as unwanted sources at each nodes of the terrestrial part of the primary system. If their frequency range is the same or close to the frequency band of the desired signal, they appear as disturbing sources. The reason of the degradation is based on the applied system structure: all of the transmitters are operating on the same frequency. In the investigated system the primary transmitters are low power devices with small service area. Because the incumbent's radio system is designed with the knowledge of the exact transmitter locations, this system can be optimized for low interference conditions over the desired service area. For such topology by using (1) the attenuation over any path or the received power at any location can be calculated and the ratio of the desired and the interfering signal powers results the signal to interference ratio map of the service area of the investigated system. The quality of service for the incumbents is determined by the SINR at the receiver location.

The desired signal power P_S can be determined for the terrestrial point to point LOS connections with (2), where P_T is the power of the transmitter given in [dBm] to which the incumbent receiver is actually connected:

$$P_S^{[dBm]} = P_T + G_T^{[dB]} + G_R^{[dB]} - 20 \cdot \log_{10} \frac{4\pi D^{[m]}}{\lambda^{[m]}}, \quad (2)$$

where G_T and G_R are the antenna gains of the transmitter and receiver respectively, D is the PtP link length of the terrestrial wireless mesh, and λ is the wavelength.

B. Interference source model assumptions

Constant transmit power of the moving interference source is assumed, however, the interfering power P_{IN} at the receivers of the incumbent system will be varying in time due to the movement of their source, therefore signal-to-interference ratio (SIR) is also time varying:

$$SIR^{[dB]} = P_S^{[dBm]} - P_{IN}^{[dBm]} \quad (3)$$

Constant seed of the moving interference source are also assumed following a random street route in a built in area as depicted in Fig. 2. For simplicity reason omnidirectional antenna and constant radiated power level of the moving interferer are considered. Because – also for simplicity – multipath propagation is not taken into account the moving interferer will cause interference for a receiver of the incumbent millimetre wave mesh network if LOS exists between them. Supposing a receiver of the incumbent system at the coordinates (x_S, y_S) and an instantaneous position of the moving interference source $(x_{IN}(t), y_{IN}(t))$, the instantaneous distance can be simply calculated as

$$D(t) = \sqrt{(x_S - x_{IN}(t))^2 + (y_S - y_{IN}(t))^2}. \quad (4)$$

Due to the movement, the level of the received interference power will also vary and depends on the instantaneous distance $D(t)$ between the current position of the opportunistic non-cooperating user as interference source and the receiver nodes of the terrestrial part of the primary system. Because the free space loss condition is assumed, the time variant $A(t)$ attenuation of the interfering signal will be proportional to the square of the distance $D(t)$ given in (4) according the last term in eq. (1):

$$A(t) \sim [(x_S - x_{IN}(t))^2 + (y_S - y_{IN}(t))^2]. \quad (5)$$

By constant velocity of the interference source $x_{IN}(t)$ and $y_{IN}(t)$ are linear function of time t and therefore the received interference power $P_{IN}(t)$ follows also a quadratic function in time.

Figure 3 shows the opportunistic non-cooperating user as moving interference source at $t=200$ min stopped causing very high interference to the closest receiver node of the incumbent terrestrial millimetre wave wireless mesh system. Dotted red line shows the interfering LOS link. The resulting SINR will be therefore very low (about -2 dB by this example).

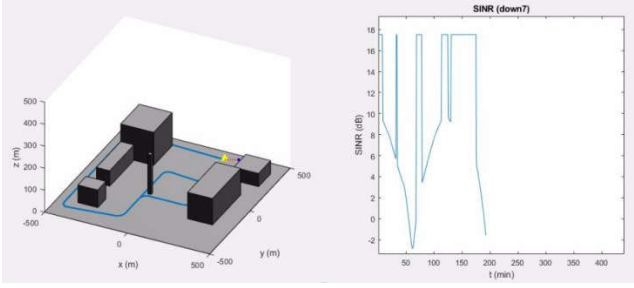


Fig. 3. Snapshot of moving interference route and the variation of the SINR of the receiver installed on building located at the right upper corner.

IV. SINR PREDICTION BY EXTRAPOLATION

The right part of Fig. 2 shows the time function of SINR at the receiver installed on building located at the right upper corner. During non line of sight (NLOS) conditions between the between the actual position of the opportunistic non-cooperating user as interference source and the receiver of the investigated node of the terrestrial part of the primary system the SINR will have its maximum value (about 17.5 dB) because no interfering signal is received. This can be observed for example in the time interval from about 130 min to 175 min . However, as LOS conditions exists along the route of the moving interference source and the incumbent receiver as it can be observed from Fig. 3 there are intervals where the SINR increasing or decreasing following quadratic functions as a consequence of eq. (5). The SINR for example decreasing in the time interval from about 30 min to 60 min , and increasing in the time interval from about 75 min to 110 min following different quadratic functions in each time interval. The differences of the quadratic functions for the individual time intervals are the consequence of constant velocity of the moving interference source and the changing angle between the LOS direction and the movement direction along the route causing different but linear time variation of instantaneous position of the moving interference source $x_{IN}(t)$ and $y_{IN}(t)$ applied in interfering signal calculation according (5).

The quadratic behaviour of the SINR variation will be utilised for prediction of the next SINR value applying polynomial extrapolation based on the measured SINR values.

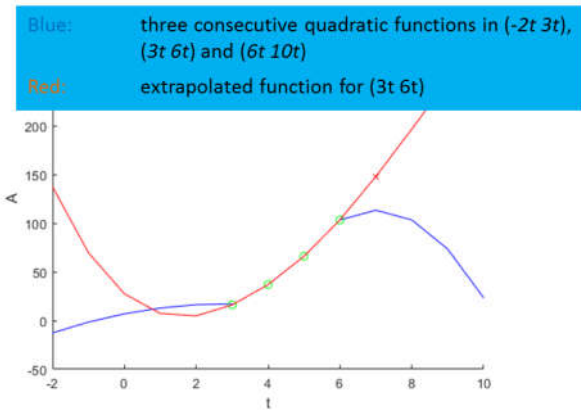


Fig. 4. Quadratic functions (blue curves) and PCHIP extrapolation (red curve).

The Piecewise Cubic Hermite Interpolating Polynomial (PCHIP) method is applied for prediction of SINR at the next time step from the previously measured value by extrapolation. For demonstration the applied prediction method Fig. 4 shows three quadratic functions over three consecutive time intervals $(-2t \ 3t)$, $(3t \ 6t)$ and $(6t \ 10t)$ and the PCHIP extrapolated values for the middle time period $(3t \ 6t)$.

V. SIMULATION RESULTS

Figure 5 presents simulation results for an interference source moving randomly with constant velocity along a built in area street mesh model. The time variation of the simulated and the predicted interference level (in dBm) at the receiver of the investigated node of the terrestrial part of the primary system installed on building located at the right upper corner in Fig 2 and 3 are depicted with green and red curves respectively. Good match of the prediction and the simulated values can be observed during LOS, however, during the transition between LOS and NLOS conditions the prediction overestimates. This is because the quick change in the time function that cannot be predicted correctly by the applied PCHIP method.

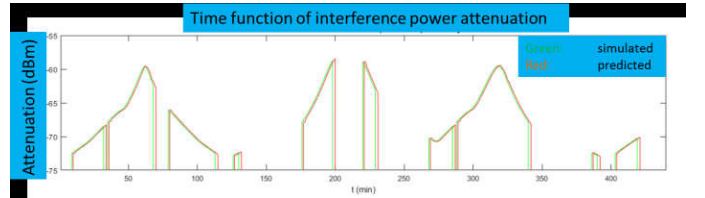


Fig. 5. Simulated (green) and predicted (red) interference level at the receiver installed on building located at the right upper corner caused by randomly moving interference source.

VI. CONCLUSION AND FUTURE WORK

As primary system a smart, scalable and flexible self-organising content delivery system that is capable to combine PtM multicast and broadcast together with PtP unicast, and caching services to provide broadband content to the end users was investigated composed by satellite broadcasting PtM backbone and a terrestrial millimetre wave wireless mesh network of 5G nodes. The terrestrial part of the investigated system, i.e. the millimetre wave wireless mesh network can also be exploited as a sensor network for signals stochastically disturbing the primary system. Any kind of stochastic disturbance for example a randomly moving interference source like a non-cooperating secondary user of the same spectrum in the area of the mesh cause SINR degradations at the nodes that are correlated in space and time, therefore theoretically allowing the detection and prediction of the disturbing effect.

Defining an SINR threshold for incumbents of the primary systems where above this level their quality of service (QoS) is ensured, cognitive channel utilization can be foreseen without degrading the quality of the primary system. Our system presumes that the exact system topology is known by the incumbent users. This can be ensured by local intelligence, or the existence of a central entity, e.g. a cognitive manager (CM). An approach using this theory was published in [2] for rural cognitive radio environment.

Using the gathered data of the terrestrial part of the primary system (for example SINR values at the mesh receivers) an appropriate method (e.g. AI) for prediction of the influence of the disturbing effect could be applied. With proper prediction of the power of interfering signal it is also possible to decrease energy consumption of the mesh network through transmit power adaptation fulfilling the goal of green communication.

ACKNOWLEDGMENT

Thanks for Csaba Berky (bcsaba@sch.bme.hu), MSc student of Budapest University of Technology and Economics how provides some figures and simulation results of this contribution.

REFERENCES

- [1] J. Mitola and G. Q. Maguire: "Cognitive radio: Making software radios more personal", *IEEE Personal Communications*, 6(4):13-18, August 1999.
- [2] L. Csurgai, J. Bitó, P. Bakki, G. Goldschmidt: "Mobility control in cognitive radio system", *FuNEMs 2012*, 04-06 July 2012, Berlin, Germany, Paper #33.
- [3] J. J. Gimenez, D. Gomez-Barquero, J. Morgade, E. Stare, "Wideband Broadcasting: A Power-Efficient Approach to 5G Broadcasting", *IEEE Communications Magazine*, vol. 56, no. 3, pp. 119-125, Mar 2018.
- [4] J. Montalban et al., "Multimedia Multicast Services in 5G Networks: Subgrouping and Non-Orthogonal Multiple Access Techniques", *IEEE Communications Magazine*, vol. 56, no. 3, pp. 91-95, Mar 2018.
- [5] P. Kántor, G. Tóth, Á. Drozdy, J. Z. Bitó. "Diversity Investigation of Satellite Backbone Network for BFWA Systems", *International Workshop on Satellite and Space Communications*, October 2009, DOI: 10.1109/IWSSC.2009.5286371
- [6] D. Gomez-Barquero, D. Navratil, S. Appleby, M. Stagg, "Point-to-Multipoint Communication Enablers for the Fifth Generation of Wireless Systems", *IEEE Communications Standards Magazine*, vol. 2, no. 1, pp. 53-59, Mar 2018.
- [7] NGMN 5G Initiative, "5G White Paper," White Paper, Feb. 2015.
- [8] J. Huschke and M.-A. Phan, "An Overview of the Cellular Broadcasting Technology eMBMS in LTE," in *Next Generation Mobile Broadcasting*, pp. 223-252, March 2013.

The popularization of space exploration amongst high school students

Ténia Kovács¹, Annamária Komáromi^{2,3}, Andrea Király^{1,3}

¹ELTE Eötvös Loránd University, Budapest, Hungary

²Balassi Bálint Secondary Grammar School, Budapest, Hungary

³MTA-ELTE Physics Education Research Group, Budapest, Hungary

kovacs.tenia@gmail.com, annamarcsi1015@gmail.com, andrea.kiraly.elte@gmail.com

Abstract—Space industry made possible for us to explore our universe by leaving the atmosphere of the Earth. It gives us great opportunities and challenges. Recruitment and motivation of the students can not be started too early, and of course we also need some appropriate methods to keep up their interest. Many people believe, that the best time to pass through the most knowledge to the students could be the secondary school age. At this age, students already have the basic knowledge in physics and mathematics that makes them able to understand more complex problems. In space research there are many areas, topics (e.g. astronomical facts, space exploration history, the ongoing projects in space research, future research plans and challenges) that are of great interest, and which are excellent for raising the interest and motivation of high school students for science courses. After a short overview of the topics and some existing programs, we will present a self-made program for secondary school students that promotes the space research for them. The tasks also fit the subject of physics, mathematics and geography. This unconventional class is interactive by involving and activating students. We have already presented the program in three different classes in a secondary school in Budapest with great success. We share experiences and analysis about the results with the audience.

Keywords— Education, Space research, Storyline method

I. INTRODUCTION

We need space researchers! The school is one of the most suitable places where teachers can motivate students in this direction. Numerous space agencies and foundations try to make people aware of importance of space exploration. For example, the NASA and the ESA pay a great deal of attention to the popularization of STEM and the space exploration both in school lessons and free time activities on their webpage.

Physics teachers also try to find new ways individually in popularizing space science and space exploration among secondary school students. Some good examples worth mentioning, such as M. Pető [1][2] who built line tracking, firefighting, life-saving robots and minisatellites and participated in CanSat competitions with her students. A. Komáromi [3][4] demonstrated some space applications in teaching thermodynamics and modeled a heat shield, which has also been shown in the Science of Stage Europe festival (a

regular biannual event with a motto: "From teachers for teachers"). Cs. Fülöp and Zs. Horváth [5] carried out an out-of-school project with their students on the topic of the brightness of stars. Or Zs. Horváth [6] designed a lesson about exoplanets and the habitable zones of stars.

Our self-made program has been inspired by all of the above.

II. THE STORYLINE METHOD

The didactical path of our project is based on the Storyline method which was developed by Steve Bell and Sallie Harkness in Scotland [7][8]. The point of this approach is that there are no lessons, the children can learn with fun but guided to develop the ability to solve more complex problems and to communicate with each other in a better way. The speciality of this method is that the teachers create a background story for the course which is based on the subject of the class and the students solve the exercises in that given situation. Storyline is a teaching method involving students to help learning a subject matter. It is basically a series of questions leading through the storyline. Students create characters for the story thus adding their feelings and attitudes to it. This will make them interested in the learning subject. Their interest motivates them to do research on the subject and thus internalize the learning process. They are encouraged to apply their analytical skills and creativity for the storyline. This method is relevant to one important statement of Marisa Michelini, who is a significant expert of the PER (Physics Education Research) "that it is necessary to create knowledge of a subject which is not static and definitive, but in progressive and continuous evolution" [9]. Based on this we have created our special physics lesson.

The backstory of our project was the popular post-apocalyptic theme. The year is 2800 and 80 % of humanity gone extinct. The Earth became inhabitable due to several natural disasters. The students are the last space researchers in the world with the task to find a new livable planet. They are the members of Post-Apocalyptic Space Agency (PASA).

III. PARTICIPANTS, PRE- AND POST-TEST

Our project was performed in the Balassi Bálint Secondary Grammar School in three different classes with a total of 75 students between the ages of 12-17. From the three classes that were participating in the project two of them were learning physics on a basic level (9th and 10th grades) and one group (the 7th grade) hadn't specialized yet.

The lesson started with a survey. Here some demographic data were collected and some questions (pre-test) about space exploration were asked from students. The questions were:

- 1) Which 3 words come to mind about space exploration?
- 2) What sciences do you think are related to space exploration?
- 3) What difficulties might astronauts encounter during the long journey?
- 4) What is a multi-stage rocket?

At the end of the program they filled out the same survey (post-test) which they got at the beginning of the lesson, so we could measure and evaluate the effect of the program. The Table I shows the exact time table of this special physics lesson.

IV. THE PROJECT (PASA)

After the survey (pre-test) the class was divided into 5 groups. Every group could select a theme in keeping with their interest from the predefined ones. These themes fitted to either physics and mathematics or any other space-related topic. It was clearly perceived that the formation of the groups was the easiest for the youngest students. After the description of the task the students became greatly excited; moreover, they laughed at the fact that they were the last hopes of humanity.

For every group the first exercise was the literature research where the students got the materials about their topics. These documents (Fig.1) contained questions to help them understand the topic, as well as a brief introduction to the exercise. Of course, they could use every aid they could find including their mobile phones with internet access. Thereafter they had to present their findings to the class. There were no limitations about the topics, they had a free hand with the content of their presentations.

TABLE I

Time schedule	
Time	Activity
5 min	Pre-test
5 min	Description of the task and select groups
15 min	Groupwork
15 min	Presentations
5 min	Post-test



Fig. 1 The starter kit of the PASA project: handouts of the different groups, badges, pre- and post-tests.

The groups of students were built around the following predefined topics: The first group, named Tatuin, was based on geographic knowledge. In this section the students could read about the aurora borealis and the environmental conditions of Earth. The Ikarus and Redbull groups dealt with questions in connection with mathematics and physics. They could learn about how solar cells work, the evolution of rockets and a story about Elon Musk's Tesla in space. The Ironman and Hamburger groups relied on the children's creativity. These groups were created so that the children who were not interested in STEM could also join the program. These topics were about articles related to the preservation of mental and physical health in space or how food is different in a space environment. In general, the experience was that every student was able to choose a group they liked so they could be an active participant in the lesson.

The special physics lesson had a starter kit. The starter kit contained handouts for the research groups. The handouts included articles, exercises and questions. Every student got a blank badge on which they could write their names. These materials were emblazoned with the Post-Apocalyptic Space Agency brand (Fig.1).

For example, the IKARUS group got two documents. In Document-I the students could read about the history and evolution of solar cells, and the difference between the photovoltaic effect and the photo-electric effect was defined and highlighted here. Document-I finished with three questions referring to the energy support of the satellites, the operation and history of solar cells used onboard on satellites.

The students could find the answer for the first question in the handout, but it did not contain the remaining answers. Therefore, they had to use the internet to answer these questions.

Document-II contained an exercise from NASA's website. The students could learn about the efficiency of the solar cells and they could use their mathematics knowledge, especially their geometry knowledge. They got 3 different geometric shapes for the solar cells and they had to calculate the areas, the perimeters and the efficiencies of the solar cells (Fig.2).

In general, this group was popular for students who liked mathematics and physics. They solved the exercises very well and quickly. Our goal with this group was to show how mathematics is used in space research and to develop their web search habits.

V. RESULTS

The results were formulated based on the development in students; awareness and knowledge between the pre- and post-surveys, as well as the experiences during the class including student presentations.

Some interesting answers from students:

"It was good to practice teamwork and public speaking"

"It's unusual, but interesting. We could do it more often"

"I am not interested in this topic, but it sparked my interest a bit"

As mentioned above, one of the questions in the survey was about how many disciplines related to space exploration the students know. In the diagram, (Fig.3) blue marks the pre-lesson survey and orange indicates the post-lesson survey results.

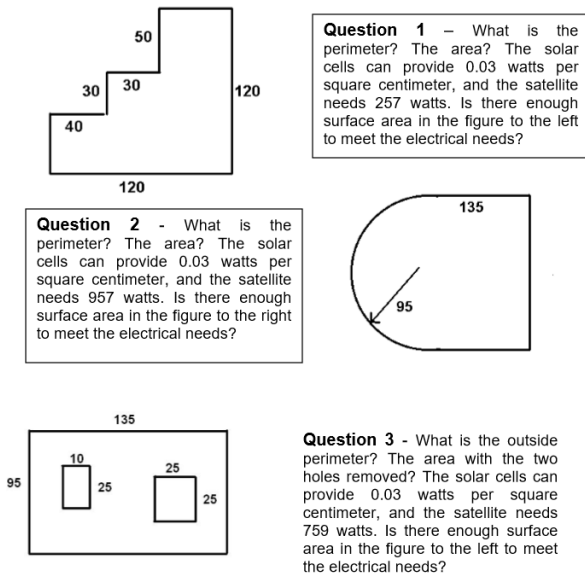


Fig. 2 The different shapes of solar panels (Ikarus group). Source: <http://image.gsfc.nasa.gov/poetry>

It is worth noting that the last question (What is multi-stage rocket?) was the most difficult one. In the pre-test, 41% didn't answer this question, but after the lesson this number decreased by 52% compared to the previous result.

A question was put to the students in group Hamburger about long-term food storage and preservation in space to see how creative they could be. To my great surprise one of the 15 groups (in the three classes) referred to the fact that we are in 2800, and because of the technological development we should be able to print food by now. So, their solution was to use 3D printed food in space.

For the group Tatuin I had the question: "Why is the sky blue?" The answer could not be found in the Document they got from me; the point was to use the internet to find it. To my surprise none of the student could find the right answer. They found the same web page from the 3 million results, but they did not understand what they read. They copied quotes from famous poets who described the sky in their view. I concluded that the students have serious problems in information processing and finding a relevant answer to a question. We have to find a solution to this problem to stop the spread of hoaxes and fake news among youngsters. Also it is important that the students be made familiar with the English language as early as possible, because much useful and up to date, correct information can be found in English on the Internet.

VI. SUMMARY

To summarize the experience of the students about our unusual class, it was positive, and what we saw was that the children are open-minded about STEM and space exploration in general. If we can present these themes interactively and entertainingly, they will enjoy it and have an interest in it. We have to popularize space exploration in their language and should not be afraid to use new methods to spark interest in them and introduce them to a new, interesting and ever-changing world to get out of the rut even if only for a short time.

We would like to finish with this interesting quote from Larry Niven.

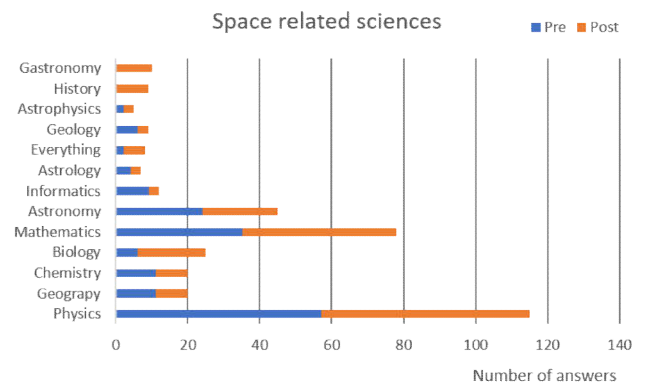


Fig. 3 Diagram of the space related sciences

“The dinosaurs became extinct because they didn't have a space program. And if we become extinct because we don't have a space program, it'll serve us right!”

ACKNOWLEDGMENT

This study was funded by the Content Pedagogy Research Program of the Hungarian Academy of Sciences.

REFERENCES

- [1] M. Pető, Space research and mini-satellites in secondary high school. *International Journal of Astrophysics and Space Science*. Vol. 5, No. 5, 2017, pp. 71-78. doi: 10.11648/j.ijass.20170505.11
- [2] M. Pető, Robotics, CanSat, Arduino – physics at Székely Mikó Science Club, In: A. Király and T. Tél (eds.): *Teaching Physics Innovatively – New Learning Environments and Methods in Physics Education*, e-book, ELTE Eötvös Loránd University, Budapest, Hungary, 2016, ISBN 978-963-284-815-0, pp. 169-174, available at: <http://parrise.elte.hu/tpi-15/proceedings.php> (last accessed 09 January 2019)
- [3] A. Komáromi, Space mishap as a stimulus context for thermal conduction exploration in secondary school. In: *e-Proceedings of International Conference GIREP-ICPE-EPEC-2017*, 2017. July 3-7., Dublin, Ireland., in press.
- [4] A. Komáromi, Space science in thermodynamics, In: E. Dębowska, T. Greczyło (eds.): *Proceedings of International Conference GIREP-EPEC-2015*, Wrocław, Poland, 2016, ISBN: 978-83-913497-1-7, pp. 207-211, http://girep2015.ifd.uni.wroc.pl/files/GIREP_EPEC_2015_Proceedings.pdf (last accessed 09 January 2019)
- [5] Cs. Fülöp, Zs. Horváth, Discover a black hole in the classroom: the “Pear-Star” Project, In: G. T. Orosz (ed.), *11th International Symposium on Applied Informatics and Related Areas (AIS 2016)*, Óbudai Egyetem, Budapest, 2016, ISBN 978-615-5460-92-0, pp. 45-49.
- [6] Zs. Horváth, Earth’s twins? Searching for Exo-Earths, In: A. Király and T. Tél (eds.): *Teaching Physics Innovatively – New Learning Environments and Methods in Physics Education*, e-book, ELTE Eötvös Loránd University, Budapest, Hungary, 2016, ISBN 978-963-284-815-0, pp. 175-180, available at: <http://parrise.elte.hu/tpi-15/proceedings.php> (last accessed 09 January 2019)
- [7] S. Bell, S. Harkness, and G. White (eds.), *Storyline – Past, Present and Future, Enterprising Careers*, University of Strathclyde, 2007., ISBN 978-0-947649-16-6
- [8] P. J. Mitchell, M. J. McNaughton (eds.), *Storyline: A creative approach to learning and teaching*. Cambridge, Cambridge Scholars Publishing, 2016.
- [9] M. Michelini, Building bridges between common sense ideas and a physics description of phenomena to develop formal thinking, in: L. Menalube, G. Santoro (eds.) *New Trends in Science and Technology Education*, Bologna, CLUEB (2010) 257-274.

Satellite Fading Classification with Artificial Intelligence for 5G

László Csurgai-Horváth

Budapest University of Technology and Economics
Department of Broadband Infocommunications and
Electromagnetic Theory, BME_HVT, Budapest, Hungary
csurgai@hvt.bme.hu

Boldizsár Márton

Budapest University of Technology and Economics
Department of Broadband Infocommunications and
Electromagnetic Theory, BME_HVT, Budapest, Hungary
martonboldizsar@gmail.com

Abstract—In this phase of the constantly changing and developing mobile telecommunication networks, the fifth generation (5G) networks are the future. In the components of the network, which are using satellite communication, it is a great issue to handle the prescribed low latency because of the great distances and some weather-related disturbances in the channel. Participation in the Alphasat scientific experimentation, allows us to gather lots of measurement data and therefore information on the atmospheric impact on radio wave propagation in the Ka/Q frequency band. Measurements are showing that a different type of precipitation in the air has a significant impact on increasing the atmospheric attenuation. When it is raining, we can see a well recognizable pattern in the fading of the channel. In the ongoing work, we are trying to use artificial intelligence to recognize and classify the pattern caused by rainfall events. This paper describes the fundamental method, that we are using and the problems that we had to solve so far.

Keywords—rain; millimeter wave; radiowave; propagation; neural networks

I. INTRODUCTION

In 2013 the Alphasat satellite was placed into orbit in the collaboration of the European Space Agency (ESA) and Inmarsat, a world-leader company in global, mobile satellite communications. Amongst other scientific experiments, the Aldo Paraboni propagation experiment [1] transmits unmodulated beacon signals at 19,701 and 39,402 GHz.

The main goal of this experiment is to study the atmospheric effects in Ka and Q-band in order to develop new propagation models and improve the existing ones. At BME-HVT, we receive these signals and measure the received signal power every second. This way we get long time series of data, which we can further work with. An important preprocessing step of the measured data is the conversion of received power to attenuation. That work can not be efficiently automated and still a significant amount of human effort is required. The main goal of this paper is to develop a computer-based algorithm that may support this work by using artificial intelligence.

By plotting a long enough part of this time series of data (Fig. 1.), we can see that the graph is not a flat line, it has basically two kinds of disturbances in it. Many smaller bumps usually with daily periods, and fewer bigger ones that are the fade events caused by the atmospheric effects. The smaller ones are due to the changing of the days and nights, which causes temperature deflection, and at day, the Sun is also a significant source of radiation. The other reason is that the satellite has a geosynchronous orbit, therefore the direction of the antennas are always changing with a period of a day.

The bigger deviations are caused by the channel, more specifically the different types of precipitation in the air, but the atmospheric gases like water vapor and oxygen are also affecting the channel.

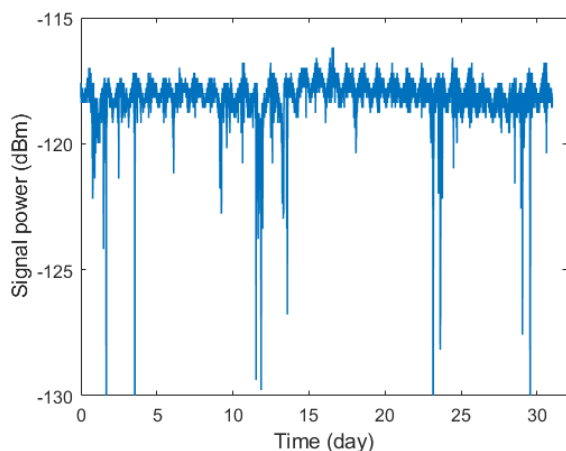


Fig. 1. Received signal power from May 2016

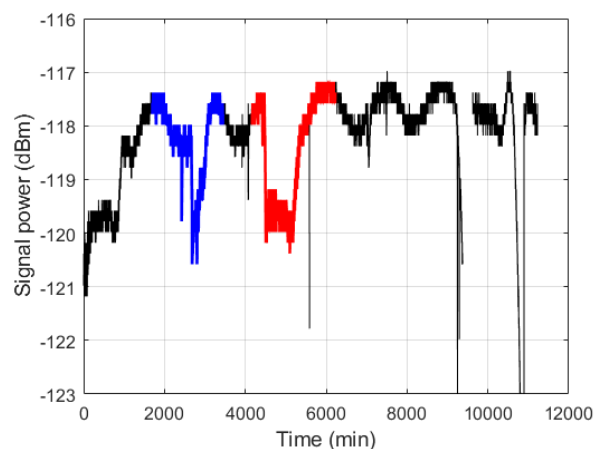


Fig. 2. Marked rain events

When it is raining, the received power is significantly smaller in comparison with the measurements on a sunny day. The attenuation of the humid, rainy atmosphere is bigger than the attenuation of the relatively dry air. Therefore only by seeing the plotted graph of the measured time series of data, we can tell whether there was a rain event or not (Fig. 2.).

The goal of satellite propagation measurements is to develop new and improved channel models and provide accurate statistical description of the radio channel. ITU-R [2] has a recommendation for this purpose and the development of the models is always an ongoing activity.

Satellite propagation receivers are usually measure the received signal power, like the Alphasat station at BME-HVT as well. For statistical purposes the attenuation distribution is required, therefore the received power to attenuation conversion is a critical part of the system. In order to achieve the best result attenuation events are selected manually, supported by a human inspection. Our goal is to support the selection of the events by using artificial intelligence that may speed up this process. We are trying to teach a neural network to learn to recognize and classify the rainfall events only by using the measured data. A final goal is to substitute as many human effort as possible with the power and efficiency of a computer.

II. THE METHOD

There are many uses of neural networks and so there are many kinds of them as well. In order to reach our goal, we would need a type that is capable of learning to classify the input samples by sorting them into different categories according to the samples of the training sets and categories.

According to the available literature the classification of the atmospheric-induced attenuation events has not so much historical background in the field of artificial intelligence; therefore we started our work with a research period. After we looked into the literature, we found that the latest release of MATLAB, a software toolset of MathWorks company has significant support and an optimal environment [3], [5] to achieve our goal, also providing numerous examples, descriptions and case studies that can be a big help to us.

To train a neural network for a specific task several preparatory activities are needed. The first step was to consider, how many event categories we needed. For the first attempt, we settled on having only two categories symbolizing “rain events” and “non rain events” (Fig. 3.). Of course, we could have had more categories, for example “starting to rain”, but first we wanted to see, if this method works, and after that we could do the next step. So we had to prepare the samples for the training. By cutting out the well recognizable rain events, what is left is necessarily the non rain events part. We divided the non rain events part into smaller segments, with a length corresponding to the length of the rain events.

Now that we had the training set of data, we had to configure our networks inner structure. We used a network configuration based on the one that was used in a very similar problem [3].

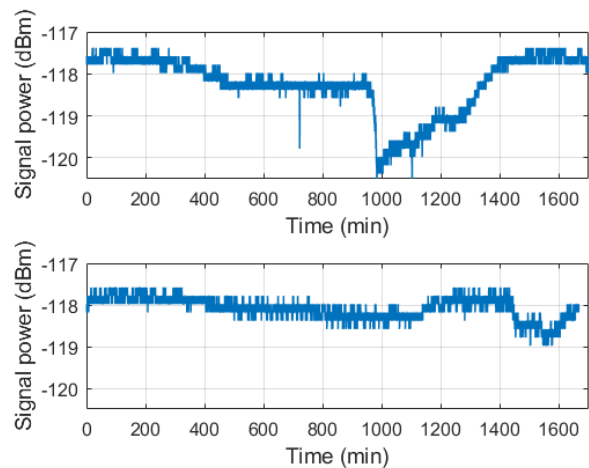


Fig. 3. Rain event (up) and not rain event (down)

There they wanted to recognize the speaker based on the two Japanese vowels that the nine speakers recorded before. It is similar to our problem in a way, that in both cases the data is a time sequence varying in length and the network has to decide based on the nature of the time series.

For processing this kind of data, the scientific literature suggests [4]-[5] that we use a network that contains a layer called LSTM, that stands for Long Short-Term Memory layer. LSTM is recurrent neural network architecture, where the connections between the nodes are forming a directed graph and the dynamic behavior of the process is handled by the internal memory of the network. It learns long-term dependencies between the time steps in time series and sequence data. To see whether the training period was successful and the network learned to classify the input samples, we had to prepare a testing set of data as well. The testing set also included samples for both category, but it is important, that they are not the same previously used in the training period. After the tests show that the network is performing fine, we can improve, introduce new categories, create a sliding window that travels through the whole sequence of the data collected during the years and marks the rain events.

III. APPLYING THE METHOD

As mentioned before, we had several steps to make to train a neural network. But before we tried our method on the actual measured data, we wanted to see whether it is a working theory.

Therefore we prepared lines and parabolic curves as training data representing the two actual categories: rain events (parabolas) and non rain events (lines). The lines varied in both the gradient and the point where they met the y-axis. The parabolas varied in the coordinates of their focus point and their “openness”. We added white noise to the curves, so they would be more similar to the actual data they were representing (Fig. 4.).

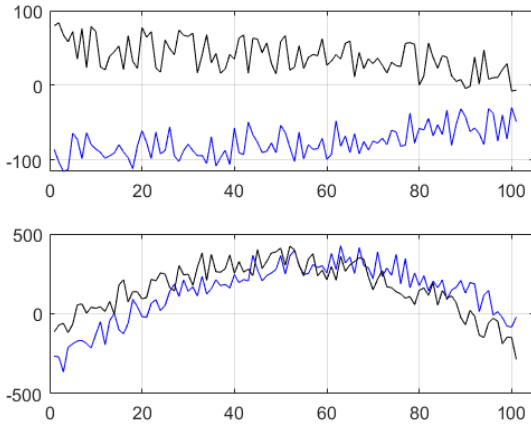


Fig. 4. Lines (up) and parabolas (down)

By using these generated samples, we trained a network to learn to distinguish between them. Then we tested it and we found that the learning period was successful. The network performed really well on the test, over 98% of the cases it guessed the category of the sample correctly. This confirmed that it is the right way to go, so we could get to preparing the training sets from the measured data. As mentioned before the rain events were easy to find and mark, the non rain events were collected according to the consideration that everything is a non rain event, which was not previously marked as rain event. When we had the training sets, we started to train a network. After waiting more than 35 hours we stopped the training when it was only at one fifth of the whole process because we found that it would take a really long time to complete. We figured out, that the cause of this may be that the data we were using has too high resolution, as it was a time series with measurements for every second. It made the samples really big and therefore slowed down to process. The possible solution was that we keep the measurements only for every minute. It made the samples more easy to handle, and as we can see on the illustration, it has not have a significant effect on the nature of the time series of data (Fig. 5.).

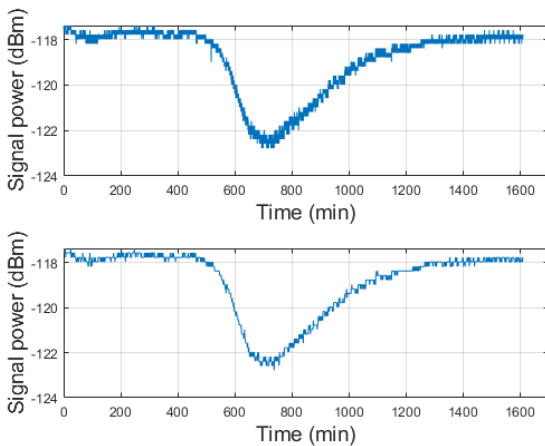


Fig. 5. Rain event sampled by seconds (up) and by minutes (down)

We trained the next network with these shortened samples, and now the training period finished in rationally acceptable time. After that, we tested the network, but the test results were unfortunately unacceptable. The network guessed almost always that the sample was a non rain event. We supposed that the cause of this may be that during the training period the numbers of the samples in the two categories were unbalanced. We had 91 samples of rain events and 427 of non rain events. In order to fix that, we created a set with equal numbers of the training samples from the two categories. Nevertheless after training a network with these balanced training set, the performance on the tests were not improving.

The thing, we figured, could cause this was that the samples from both categories were fluctuating with relative high frequencies, which could hardened the network to learn to distinguish between them. So we filtered the samples with a low pass filter, similarly as it is described in [6], using the Fast Fourier Transform methodology. This way we have got much cleaner graphs by not effecting significantly the nature of the time series (Fig. 6.).

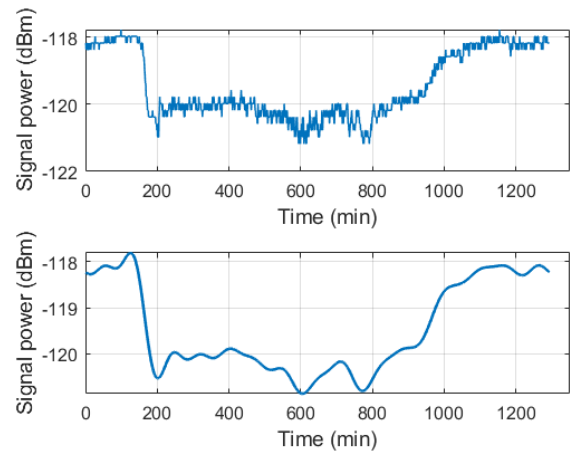


Fig. 6. Rain event before (up) and after (down) filtering

After the training period with these filtered samples, we tested the network, but the problem was still present, the network's guess was almost every time that the sample belonged to the non rain event category.

This is the point we have gotten so far, but our work continues until we reach our goal. The main reason of the false event detection may be resulted by the non-proper selection of the training data. The difference between the rainy and non-rainy data were probably not significant enough that prevented the correct decision.

IV. SUMMARY

Our original goal was to train a network to learn to distinguish between the two categories of input series of data whether they were rain events or non rain events. To do that we investigated the basics of how neural networks work, tested the method with our own generated data and it showed that it could work for us. After that we started to use the original

measurements to train our networks. During that we had some problems that we tried to solve, and we have to continue our work to achieve our goal.

V. FURTHER PLANS

As for the next step, we think that we have to look deeper into the inner structure of our networks in order to come up with a configuration that is more effective on the task we need them to do. It is also important to prepare more of the training samples for both categories.

Another approach that worth considering is that we not only use the time series of the measured data as it is, but we calculate some additional property of them, for example the difference between the higher and the lower point of the section of the sequence. The literature suggests [7] that giving these additional properties as another dimension to the samples, it can ease the network to complete its function.

While continuing our work we will make these steps and see which one helps the best. As mentioned above the long-range goal would be to introduce new categories and eventually totally automatically recognize the different kinds of atmospheric fading events in the radio channel.

ACKNOWLEDGEMENT

The results presented in this work were established in the framework of the professional community of Balatonfüred Student Research Group of BME-VIK to promote the

economic development of the region. During the development of the achievements, we took into consideration the goals set by the Balatonfüred System Science Innovation Cluster and the plans of the "BME Balatonfüred Knowledge Center", supported by EFOP 4.2.1-16-2017-00021.

The project was funded by the European Union, co-financed by the European Social Fund (EFOP-3.6.2-16-2017-00013).

REFERENCES

- [1] C Riva, L Castanet, L Csurgai-Horvath, O Fiser, F Lacoste, F S Marzano, F P Fontan, J M Riera, A Arocha, M Schoenhuber, "The Aldo Paraboni Scientific Experiment: The Preparation and Plans for an European Measurement Campaign," 20th Ka and Broadband Communications, Navigation and Earth Observation Conference, Salerno, Italy, 1-3 November, 2014.
- [2] Recommendation ITU-R P.618-13, "Propagation data and prediction methods required for the design of Earth-space telecommunication systems," ITU, 2017.
- [3] Mathworks, "Sequence Classification Using Deep Learning," Deep Learning Toolbox Documentation, 2018.
- [4] Hochreiter, S, and J. Schmidhuber, "Long short-term memory. Neural computation," 9(8), pp.1735–1780. 1997.
- [5] Mathworks, "Long Short-Term Memory Networks," Deep Learning Toolbox Documentation, 2018.
- [6] A. Martellucci et. al. "Cost Action IC0802. Handbook of Microwave Propagation Measurements for Satellite and Terrestrial Links," ESA/ESTEC, Noordwijk, The Netherlands, 2012. v. 2.0.
- [7] M. Kudo, J. Toyama, and M. Shimbo, "Multidimensional Curve Classification Using Passing-Through Regions," Pattern Recognition Letters. Vol. 20, No. 11–13, pages 1103–1111.

UltimaSpace Experiments on the ISS

Hungarian Astro Pi Contributions

Florian Vamosi, Peter Posa
 Student Science Laboratory
 Mihaly Tancsics Grammar School of Kaposvar
 Kaposvar, Hungary
 ceo@ultimatemedi.hu, coo@ultimatemedi.hu

Abstract— The UltimaSpace Experiments started in 2016, when the First European Astro Pi mission was launched by ESA and The Raspberry Pi Foundation [1]. Teams of students from all ESA member states could join the competition to design and code their space experiments that could be selected to run on the ISS. The codes had to be written in python and had to match the mission rules, so they could be executed on the Astro Pi computers already placed on the station. In 2017 our code was selected as the only Hungarian entry to run aboard the station. Our experiment’s main goal was to find the weakest points of the Earth’s magnetic field. It was very successful. Last year we were planning on measuring the light pollution over Europe with the Astro Pi’s Infrared camera, the use of which was prohibited the previous year. Our main goal was to see whether we can distinguish dark sky protection areas from cities at night. Unfortunately, due to the massive number of submissions we hadn’t been selected. This year we have put the additional goal of proving the Earth is globular into our submission. We are in phase two now, we will find out if our experiment gets executed in April.

Keywords— *education, Astro Pi, space experiments, research-based teaching, space generation*

I. INTRODUCTION

The UltimaSpace Experiments started in 2016, when the First European Astro Pi mission was launched by ESA and The Raspberry Pi Foundation in 2016 following the success of the UK Astro Pi mission in 2015 [1]. The UK mission’s goal was to get more students involved in programming by giving them a chance to get their coded experiments up in space. The selected experiments were run on the Astro Pi computers aboard the ISS.

A. What Is an Astro Pi?

An Astro Pi is a small computer enclosed in a flight case, with many different sensors that can be used to collect data. Each Astro Pi on the ISS has a camera module; Ed has a visible camera and Izzy has an infrared camera. They are based on the very popular Raspberry Pi mini PC [2]. Ed and Izzy have been sent to the station in 2015 for the UK challenge and Tim Peake was the British astronaut who deployed them.

II. OUR INVOLVEMENT

We are members of a team of Student Scientists from Kaposvar, Hungary. We are students of the Mihaly Tancsics Grammar School of Kaposvar. We do our research at the Student Science Laboratory of the institution.

We first heard about the UK mission in July 2016, when on vacation in Great Britain. We bought the then current issue of the Mag Pi magazine and read about the mission there. After our vacation, in October 2016 we saw the announcement of the European Astro Pi mission in the Raspberry Pi Weekly newsletter. We were excited and jumped on the opportunity immediately.

We had to submit our initial idea by the end of October. Our idea was to find out if the region of the “South Atlantic Anomaly” can be detected with a magnetometer. In December we received an Astro Pi hardware kit and a letter in the mail, saying we have been selected for Phase 2 of the competition, which is writing the code and submitting it for judging.

In the second phase we had two missions, we had to write code to sense the presence of crew members in the Columbus module of the station in addition to our own experiment.

A. Our code had to comply with numerous rules:

- At least one sensor per mission has to be used;
- The LED matrix has to be used;
- Data has to be collected and stored with a timestamp for later analysis on the ground;
- Codes must be written in Python 3.4 or 2.7;
- The total time of execution for both the primary and secondary missions combined cannot be more than 3 hours.
- Considering the busy schedules of the astronauts, the Astro Pi on the ISS will be controlled from the ground without the involvement of the crew. For this reason:
- Astronaut interaction with the Astro Pi through the joystick and the buttons cannot be considered in your mission design and execution code;

- The Astro Pi cameras cannot be used;
- The Astro Pi cannot be moved from and around its fixed position in Columbus.

B. Our Experiment

Our code detected the presence of crew members by using the temperature sensor of the Astro Pi. We have used 2 weeks of prerecorded data to set up a baseline temperature above which a crew member must be present.

The second part of the mission was to gather data for our experiment. Our experiment's main goal was to find the weakest points of the Earth's magnetic field. We did this by collecting magnetometer readings along with latitude and longitude information of the space station. We used the PyEphem ephemeris module to calculate the position of the ISS above the Earth's surface using the TLE (two-line element set) provided by ESA containing the orbital elements of the station. We collected all the data in a CSV (comma-separated values) file for later analysis on the ground.

We had to submit our experiment for judging by the end of February 2017. After the submission we have received a letter saying "Congratulations! Your code has been qualified to fly and run on the International Space Station.". Our code could run aboard the ISS for 3 hours.

We have received our CSV file with the collected data on 17 May 2017. After receiving the data, we have made a visualization of our measurements on our website [3]. The visualization is a Google Geochart showing the 100 lowest measured magnetic field strengths as data points on the world map. When you hover over the data points you can see the exact values in microteslas.



Fig. 1. Measured Data Geochart

Our code can be found on our GitHub repository [4].

III. LAST YEAR'S MISSION

The Second European Astro Pi Mission was Announced by ESA and The Raspberry Pi Foundation in October 2017. This time around students could compete in two categories Mission Zero and Mission Space lab, 0-14 and 15-19 years old respectively.

Teams in mission zero had to use the online Astro Pi Sense Hat web emulator to code a greeting message and ambient air temperature display for the crew, that would be guaranteed to run in space.

We are participating in Mission Space lab. This Mission has two Themes, Life in space and life on Earth. Teams that chose to investigate 'Life in space' had to make use of the Astro Pi Ed, which is located in the Columbus module and features a visible camera, to run their investigation.

Teams that choose to investigate 'Life on Earth' had to make use of the Astro Pi Izzy, also featuring an infrared camera and located at one of the ISS windows, looking down to Earth [5].

IV. OUR INVOLVEMENT LAST YEAR

We chose the theme of 'Life on Earth' and we have submitted our experiment involving light pollution of large cities in Europe.

We would have liked to measure the level of light pollution over populated areas of the world and compare it to scarcely or non-populated areas light pollution levels. Our main goal is to see whether we can distinguish dark sky protection areas like the "Zselic Park of Stars International Dark Sky Park" [6] and the "Møn and Nyord International Dark Sky Community" [7]. We also intended to detect the percentage of LED streetlights compared to traditional incandescent. Our results would have been a world map showing the lowest and highest light pollution areas and a graph showing the percentage of LED lights in our observed regions. Our observation prioritized Europe, but was not limited to it, so we would have need to conduct the experiment when the ISS flies above Europe at night.

We were planning on using the camera of Astro Pi Izzy to capture blue filtered infrared shots of the earth. From the pictures we could have determined light pollution levels. We then would have calculated the location of the ISS when the picture is taken with the python module pyEphem. The filenames, location, and timestamp would have been logged in a csv file. We would have used ground analysis to determine the light pollution levels and the color of street lights across the world.

Our experiment was selected to continue in phase 2. It was coded and sent for evaluation. Unfortunately, due to the massive number of entries, our experiment wasn't selected to run on the station. This could have been due to a number of things. The most probable is that our code didn't include any in-flight analysis and in consequence wasn't complex enough.

V. THIS YEAR'S EXPERIMENT

In the fall of 2018 the third, now yearly Astro Pi Mission was announced. [8] There are only minor changes to the mission rules, but they are very similar to last year's rules. All codes are required to be written in Python 3 now, every code has to terminate itself before the dedicated time ends, and all exceptions should be handled.

This year we have decided to continue with the theme of measuring light pollution and the percentage of LED streetlights. In addition, this year we are trying to prove the Earth is round, by showing the night and day ratio is approximately 1:1.

We have completely rewritten our code to use the latest version of Python 3. In flight analysis for mean brightness, and day/night logging were also added. We have also tested our code on multiple versions of flight software.

As of now we know that it is not possible to specify when the experiment runs, so we might not get a good coverage of Europe. If we get selected, we will only have two orbits to capture pictures, so we will not be able to make a global map of light pollution, but hopefully we will be able to distinguish dark sky protection areas from large cities anywhere it happens to be nighttime when our experiment runs even if it is daytime in Europe.

If our experiment runs in space, this year's challenge also includes analyzing the flight data and submitting the results which will be judged, and a final winner will be chosen.

If our code is selected, we will use python libraries and photometric software to process and analyze our data. If this is the case the new results will also be published on our site. [4]

VI. ASTRO PI'S PLACE IN EDUCATION

The best way to teach students is to show them how to learn. The Astro Pi Mission gives a great opportunity for students to learn about space and the importance of coding and logic at the same time. It makes students solve their own problems and answer their own questions. Therefore, combines the greatest of skills needed in real life.

Learning programming is a necessity for today's scientists. The reason behind this, is that a programmer doesn't understand the science behind a piece of software needed for scientific research. This makes it a lot harder to write efficient and usable code. It is a lot easier for everyone to code their own experiment than it is to explain the experiment to a programmer, who doesn't have any scientific background.

For this purpose, most of all universities teach science students programming. In Hungarian High Schools unfortunately this is not the case. Astro Pi however brings scientific programming to the High School level in a very exemplary way. For this reason, Astro Pi needs to be supported.

Our school now runs a dedicated workshop to coding based scientific research. We are big supporters of this, because children are getting into citizen science at a very young age.

REFERENCES

- [1] Astro Pi Website, <http://astro-pi.org>
- [2] Raspberry Pi Website, <http://raspberrypi.org>
- [3] UltimaSpace Website, <http://ultima.space>
- [4] UltimaSpace GitHub, <https://github.com/ultimatecompany/ultimaspace-anpd>
- [5] Astro Pi 2017-18, http://www.esa.int/Education/AstroPI/The_2017-2018_European_Astro_Pi_Challenge_begins
- [6] Zselic Starry Sky Park on the IDA's website, <http://darksky.org/idsp/parks/zselic>
- [7] Mon and Nyord International Dark Sky Community and International Dark Sky Park on the IDA's website, <http://darksky.org/idsp/parks/monandnyordpark>
- [8] Astro Pi 2018-19, https://www.esa.int/Education/AstroPI/The_European_Astro_Pi_Challenge_2018_2019_run_your_experiment_in_space

Developing Balloon-Borne Payload for Remote Sensing Applications

Zsófia Bodó , Bence Dávid Góczán

Simonyi Karoly College for Advanced Studies

Budapest, Hungary

bodo.zsofia@simonyi.bme.hu, goczan.bence@simonyi.bme.hu

Abstract—For remote sensing and earth observation purposes the usage of satellite technology means a common solution. It is a widely used technique to obtain useful data in several fields of interest for research, environmental and industrial key players. With these methods we can gather data about landmarks, patterns, crops, forests, minerals, water and various other resources.

Remote sensing from stratospheric balloons is not yet a widely spread and thoroughly researched idea. There have already been proof-of-concept launches, which show significant research and industrial opportunities in this area. The technology is relatively cheap, easily accessible and can be developed, integrated and launched quickly if needed.

This paper focuses on the development of a low cost, small size, balloon-borne remote sensing payload using COTS (Commercial off-the-shelf) components and how stratospheric balloons could be used to perform localized, small scale remote sensing missions.

The UPRA Project (Universal Platform for Robotics and Aerospace) is a student project with an aim to develop a reliable, widely configurable, low maintenance, high altitude balloon platform for university research groups. The development team consists of the members of the Simonyi Károly College for Advanced Studies at the Budapest University of Technology and Economics.

The aim of the project is to build a proof-of-concept multi-spectral remote sensing hardware and using open source and self-developed software to analyze data provided by the payload to demonstrate that high quality and relevant remote sensing can be achieved for a comparably low price.

The remote sensing payload is planned to have two identical images sensors with a pixel resolution of 1600x1200px. The selected sensor has a wide spectral sensitivity in visible and near-infrared range (420nm – 980nm). Applying different optical filters on the sensors would lead to near identical images in different spectral range. Using infrared-pass filters, the payload will be able to collect data on vegetation and urbanized thermal footprints.

With a stratospheric balloon large areas could be covered during a flight and balloons could be launched in a frequent manner. The collected data could help authorities to organize

protection or salvage during floods, after hails or storms. Also valuable information could be provided to the agriculture on vegetation covered areas and inland waters from sowing to harvest.

If this proof-of-concept project would be successful it could be the foundation for regular scientific remote sensing balloon missions in Hungary.

Keywords—*high altitude balloon, remote sensing, earth observation, agriculture*

I. INTRODUCTION

Remote sensing provides crucial information in agricultural applications. Monitoring vegetation health and open water surfaces like inland-water or flooded areas could improve prognosis on crop yields and help planning actions in crop management.

Besides already available and widely used remote sensing platforms, balloons could provide frequent data coverage for a reasonable cost.

This paper covers the benefits of small balloons in remote sensing and the development of a balloon-borne multispectral remote sensing payload.

II. REMOTE SENSING PLATFORMS

For gathering remote sensing data multiple platforms can be used. Common method is the usage of data provided by remote sensing satellites. For smaller areas different airborne methods are used as well, such as aircrafts (manned or unmanned aerial vehicles) and/or drones. These data gathering methods differ significantly in many parameters - such as area covered, modularity, scalability or cost effectiveness - that can be enhanced in selecting the right method to the right application purposes. However there is a way of data gathering that has a different characteristic regarding the technological and business parameters but is relatively unresearched in this field of application. The usage of high-altitude balloon platform for remote sensing applications is still mostly in the proof-of-concept phase in the research domain worldwide.

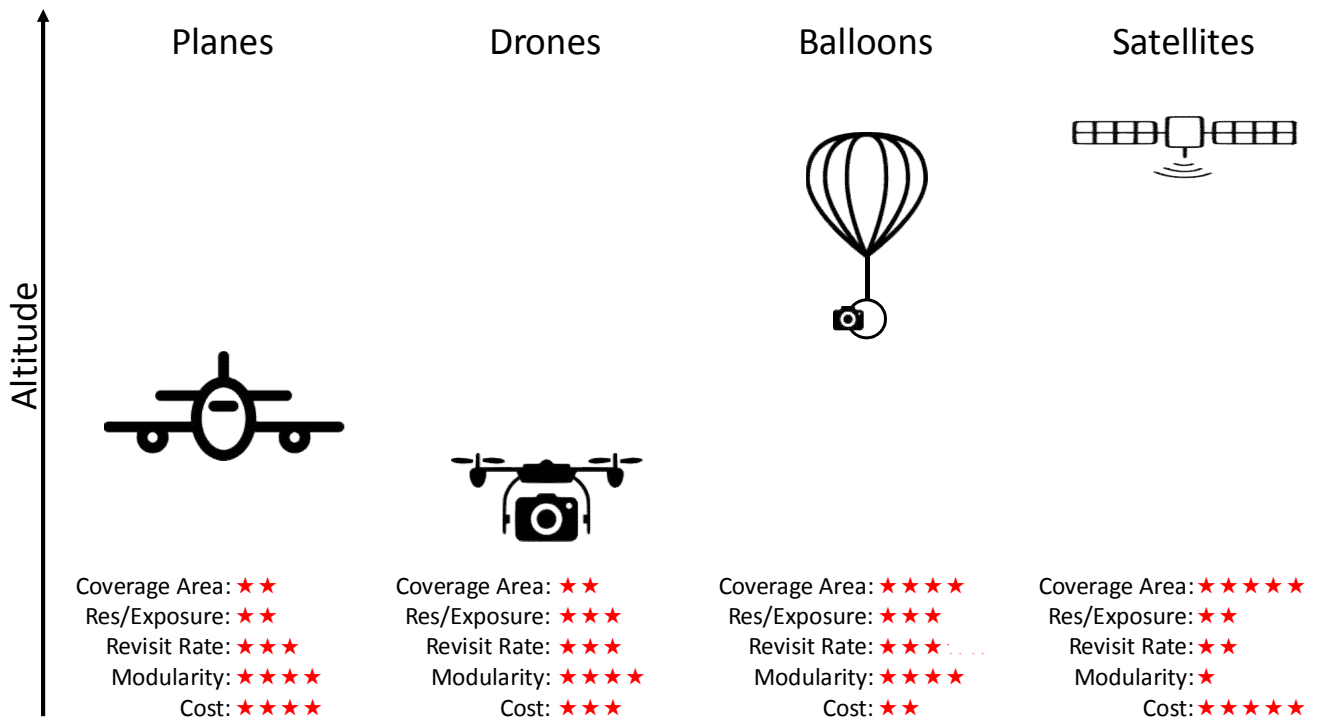


Fig. 1 Comparison of remote sensing platforms

As we can see in Fig. 1 in the parameter of covered area, satellite platforms are highly effective, while drones or commercial aircrafts are on the lower side of the scale. However with the peak height of 30000 meters (reaching the stratosphere region) high-altitude balloon platforms can also cover a significant area during its flight.

If we are looking at the cost effectiveness of the different carrier objects, we can see that drones and commercial aircrafts can be regarded as cost effective. However even if we count on a longer lifecycle for a remote sensing satellite, the planning, development, validation, launch and control activities will sum as a significantly high amount of cost. The usage of balloon platform is again in the positive side of the scale. A full development, validation and launch cycle for one flight can be solved from as little as 350-400 EUR.

III. REHAB BALLOON PLATFORM

ReHAB – Reusable High Altitude Balloon-platform is developed by the Universal Platform for Robotics and Aerospace (UPRA) Team of Simonyi Karoly College for Advanced Studies. The platform is developed and manufactured by students and designed to carry small science payload up to 30 km to the stratosphere.

The goal of the UPRA Team is to support university research groups with affordable launch opportunities providing the platform, launch and recovery service and flight planning.

The avionics system of the platform provides two way radio communication, live tracking and data storage. It is also possible to monitor and control the science payload.

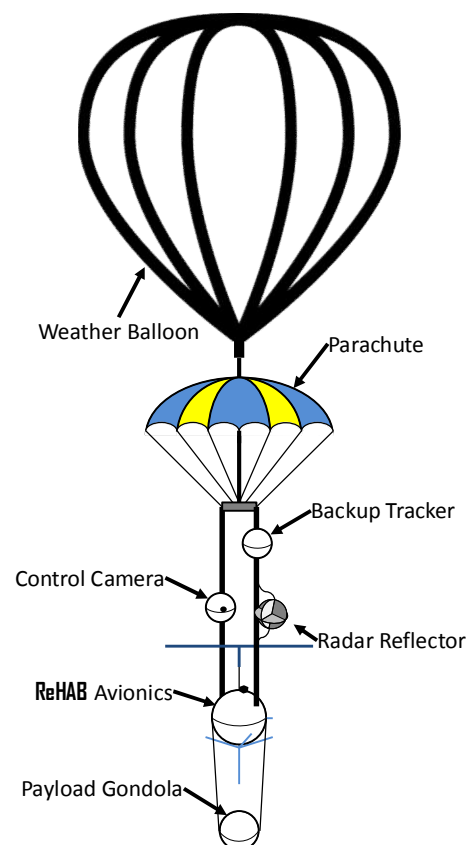


Fig. 2 ReHAB flight configuration

The platform is highly configurable to meet the mission demands. It is planned that a standardized payload gondola to be provided but also custom made payloads are acceptable. The flight configuration of the platform can be seen in Fig. 2.

IV. REMOTE SENSING PAYLOAD

Detecting vegetation covered and open water surfaces can be performed using near-infrared (NIR) imaging combined with visual (VIS) image data. To provide consistent data multispectral cameras should be used which capture images in different wavelengths at the same time.

A. Remote Sensing Concept

Plants reflects green wavelengths in the visible spectrum and a large amount of near-infrared (680-900nm) waves while open water surfaces reflect very little or no waves in the near-infrared spectrum. Using a NIR image sensor makes possible to detect both vegetation and water reservoirs.

Processing composite images generated from NIR and visible spectrum images can provide information on vegetation health, composition of plant life and proportion of vegetation and water covered areas. This information can be used to measure inland-water and flood-water impact on crops.

B. Hardware Implementation

The multispectral camera is built around two identical OV2640 image sensors. This sensor is selected because of its large spectral sensitivity in both visible and near infrared light (Fig. 3). To provide clear images lens filters are used on both sensor modules. For visible light a 650nm short pass is applied to cut the higher wavelengths. For the NIR imaging a 680nm long pass filter is used to eliminate the higher frequency (visible and UV) lights to reach the sensor.

The current prototype (

Fig. 4) is built with two ArduCAM Mini 2mpx modules as sensor boards. Each module has an OV2640 sensor, M12 (S-Mount) lens mount and an image buffer for temporary storage. The separate image buffers makes it possible to take pictures at the same time with both cameras and permanently store the visible and NIR images on the same storage.

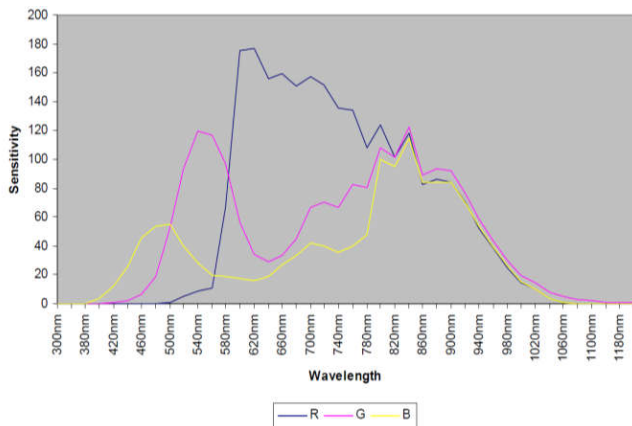


Fig. 3 OV2640 Spectrum Response [1]

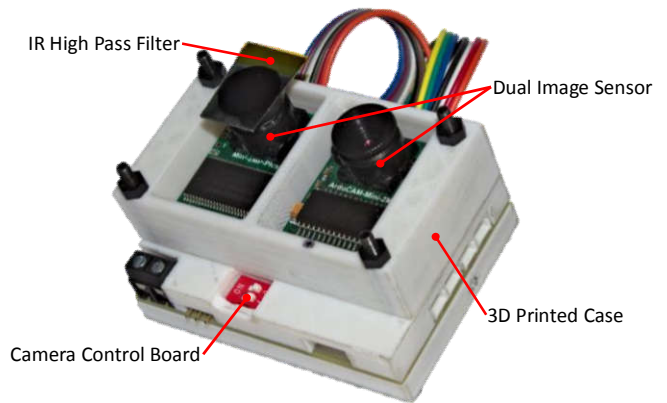


Fig. 4 Remote sensing camera prototype

The camera is controlled a Microchip Atmega328p Arduino compatible microcontroller which configures and controls both of the camera modules, handles the non-volatile storage and file system and provides connection to the platform. The microcontroller provides an intervalometer function for autonomous operations.

The non-volatile storage for the images is an SD Card with FAT filesystem. This provides easy access to the images taken during flight. The pictures are saved with a running number and an indicator. The indicator shows if the image is in visible light spectrum or NIR spectrum.

With a configuration file on the SD Card makes it possible to set different options of the camera payload like the intervalometer period. The running number of the next image is also saved on the SD Card to prevent file overwrite in case of microcontroller restart.

The camera payload can be connected to the balloon platform via RS232 serial port. Through this port housekeeping data can be downloaded from the camera, image properties can be set and exposure can be triggered. The data bus also makes it possible to transfer low resolution images from the camera to the On-Board Computer storage and download them via radio link during flight.

V. IMAGE PROCESSING METHODS

A. Overlapping

The images taken by the twin sensors have some offset due to the distance between the camera lenses. This effect becomes less significant as the distance grows from the target, but still needs to be dealt with. The images could be overlapped by hand but with the large amount of data gathered during a flight it could be painstaking. To automate image overlapping calibration pictures should be taken prior to flight. This process is needed to compensate lens distortion and sensor offset.

Automated overlapping is still under development in the time this paper is written. For image processing OpenCV libraries are used.

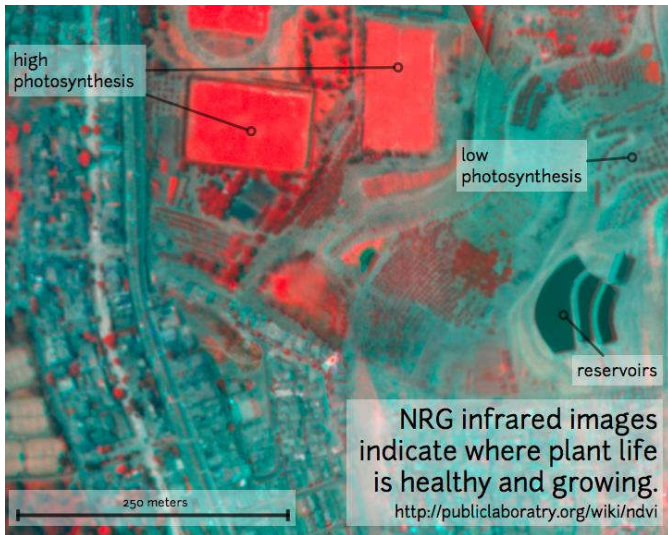


Fig. 5 NRG False color image [2]

B. NRG False Coloring

NRG False Coloring swaps color channels of the image using the red and green channels of the visible light and adds the NIR information as third channel (Fig. 5). The blue channel of the visible spectrum image is discarded since higher frequency waves are not carrying useful information in this case.

This false coloring method helps visualize the NIR data as an addition to the visual light information.

C. NDVI Heatmap

Normalized Difference Vegetation Index (NDVI) is used to measure vegetation health and density. NDVI is calculated by equation (1) and varies between -1.0 and +1.0 where the more positive value indicates healthy, dense vegetation. Since open water surfaces reflect very little or no NIR light values close to -1.0 usually represents water or snow covered surfaces.

$$NDVI = \frac{NIR - VIS}{NIR + VIS} \quad (1)$$

NDVI computation is a pixel wise transformation and can be visualized as a heatmap (Fig. 6)

More accurate results can be achieved by using only particular wavelengths of the visual image practically using band filters on different VIS image sensors.

Both NRG false coloring and NDVI Heatmap calculation can be done using OpenCV libraries to automate the process.

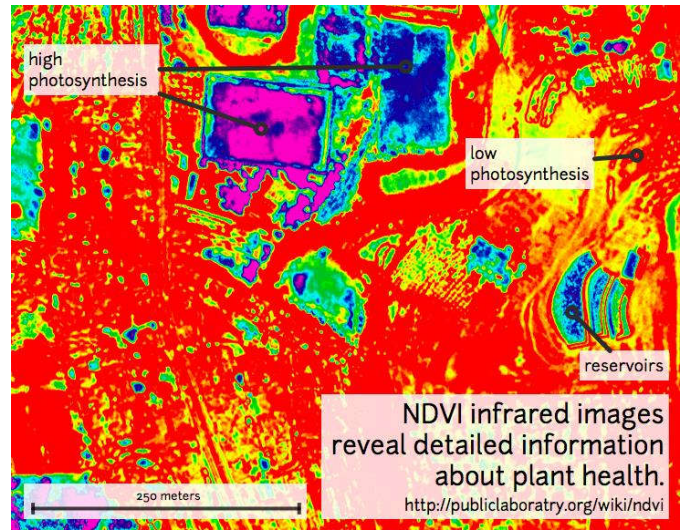


Fig. 6 NDVI Heatmap [2]

VI. SUMMARY

With a stratospheric balloon large areas could be covered during a flight and balloons could be launched in a frequent manner. The collected data could help authorities to organize protection or salvage during floods, after hails or storms. The domain offers lots of possibilities for enhancing the capabilities of the remote sensing platform. The long term development and validation plan for the balloon platform provides us guidance for gradually adding features and functions to the remote sensing payload while still keeping the platform safe, scalable and modular.

REFERENCES

- [1] OMNIVISION, "OV2640 Datasheet," OmniVision Technologies, Inc., 1341 Orleans Drive Sunnyvale, CA USA, 2006.
- [2] J. Warren, „Public Lab Wiki - NDVI and NRG,” 2018. [Online]. Available: <https://publiclab.org/wiki/ndvi>

The technology of CanSats, which can involve secondary school students in space

András Illyés

Budapest University of Technology and Economics,
Mechatronics Engineering
Budapest, Hungary
illyesandris@gmail.com

Levente Dudás, András Gschwindt

Budapest University of Technology and Economics,
Department of Broadband Infocommunications and
Electromagnetic Theory
Budapest, Hungary

A CanSat is a can-sized minisatellite used to teach space technology & science. It features very similar technologies like real minisatellites, which leave the atmosphere and orbit the Earth. They also have to perform atmospherical experiments. CanSats are often serve as a payload for sounding rockets/research rockets. Building a CanSat is a great opportunity for every student to begin with when they are interested in space, especially in space technology

Keywords: *minisatellite technology, education, spectrum analysis, satellite landing mechanism*

I. INTRODUCTION

Various space organizations, agencies organize CanSat competitions with slightly different educational purposes. The CanSat Competition of the European Space Agency (ESA) [1] aims to give secondary school students and teachers a space-experience.

The space-related student organization of Budapest University of Technology, called Cosmos Society [2] is willing to organize the next year's Hungarian CanSat Competition with the Hungarian Astronautical Society (MANT) with the same goals and also in order to select the Hungarian teams for the European CanSat Competition from year to year.

This paper contains a summary of the technical achievement of Team HunSat [3] in the 2018 CanSat Competition. More details about our project can be find in our CanSat Final Paper. This report was selected as one of the three best final papers in the Competition. ESA's post about this and our paper can be find on the website of ESA. [4]

II. ABOUT OUR TEAM

We were the official Hungarian CanSat team in the 2018 ESA CanSat Competition, named Team HunSat (András Illyés, Benedek Tomka, Domonkos Cseh, Domonkos Dessewffy and our teacher, Levente Dudás).

We won a special prize with our technical achievements. The finals were at the Azores Islands, Portugal in June 2018.

III. TECHNICAL INTRODUCTION TO OUR MISSION

We built our CanSat to be a small planetary probe, which is able to land and do measurements anywhere - on another planet as well, according to our science-fiction vision.

Our CanSat is able to do telecommand via our very well impedance-matched communication link at 434.800MHz. It ensures proper communication for more than 250km of distance, and a forward error correction algorithm helps receiving all data. This algorithm also helps our CanSat to communicate with the Ground Station via an encrypted channel. Our radio can be tuned to different frequencies, different transmit powers, and different duty cycle.

We integrated many sensors on a single PCB, thus leaving space for other experiments inside our CanSat. This PCB, the main board also does many measurements by itself, not just the obligatory measurements in the competition. There is no need to have a battery charger, or a USB-Serial converter, because everything (charger IC, FTDI chip) is integrated on this board right next to the main microcontroller, the sensors, and the radio.

The chassis and the parachute of our CanSat are also designed and made by us: they are from durable materials; the chassis can protect the CanSat, and the parachute assures that it lands safely. The chassis is SLS 3D printed, and the parachute is from a special parachute polyamide material with a special shape.

Our CanSat also has a targeted landing system, which helps it land to a desired GPS coordinate. This (sub)system is separate from the main system to ensure stability of data collection and communication with our CanSat, even in case of failure of the targeted landing system. This system consists of a microcontroller and a servo, which controls the parachute. The parachute is similar to a paraglider, thus it can be controled. The microcontroller works as a finite-state machine, but also with a sense of intelligence. It calculates the speed and direction of the wind from previous data of turnings and the previous controlling data.

The main measurement of our CanSat is the radio frequency (RF) spectrum analyzing. It analysis the GSM spectrum, thus we

have data about how polluted our environment is with RF radiation. This is useful on a different planet (maybe not in the GSM band), but on the Earth as well. The needlessly radiated RF signals means money loss, but pollution as well.

The communication link, the telecommanding, and the advanced telemetry succeeded perfectly during the competition.

We had some difficulties with the targeted landing system because of the big wind. We didn't have the change to test our system in winds like those on the Azores, but now we are working on a solution to this.

Our main measurement, the spectrum analyzing was successful, we collected data according to this problem. We already started to work on our updated spectrum analyzer.

IV. TECHNICAL DESCRIPTION - HARDWARE

Our mission was to design and build a CanSat to be launched and deployed from a rocket at an altitude of about 1000 meters. The CanSat is to descend no faster than 11m/s.

In the actual experiment the CanSat was deployed at an altitude of about 850 meters, and had approximately 5-6m/s descent speed.

The key devices on the board of the CanSat were:

- Data collecting subsystem
 - Temperature & humidity sensor
 - Pressure sensor
 - Optical dust concentration sensor
 - Acceleration & gyroscope sensor
 - GPS
 - RF spectrum analyzer
 - Communication transceiver
 - Microcontroller, power supply
- Targeted landing subsystem
 - GPS
 - Servo
 - Microcontroller, power supply
- Parachute
- Chassis

A. PCB and electronics

The main PCB gives place to our sensors, so it needs to be from a durable material: our PCB is a professional printed board. We saved space by integrating every sensor and communication system on one unit. The PCB board is depicted on Fig. 1.

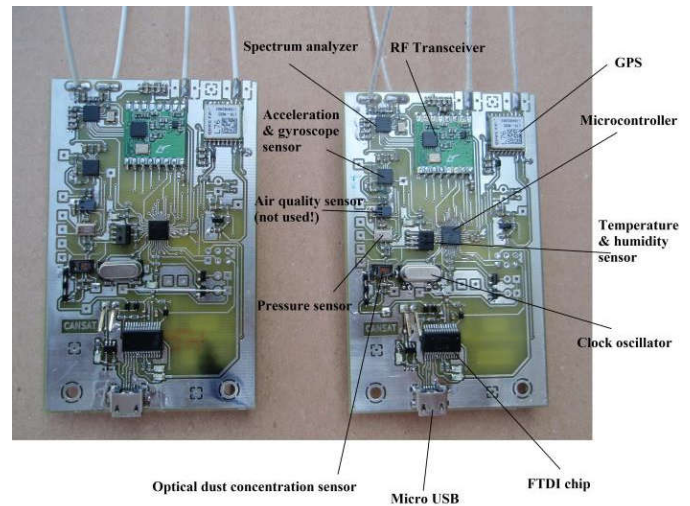


Fig. 1. Main PCB board of the HunSat CanSat

B. Chassis

The main task of the chassis is to absorb the impact of the collision. It was a challenge to find a place for every component and also protect them. Another challenging task was to find a way how all the sensors on our board can get enough air inside a closed chassis. This is why we decided to design our own chassis from scratch. The chassis is 3D-printed with SLS technology.

C. Parachute & servo

We chose to make our own parachute instead of buying a parachute to make our CanSat more controllable. We worked with a polyamide-silk material of the NZ Aerosports parachute manufacturing company. This means our CanSat is very strong and durable. We also designed the shape of the parachute after many tests. With pulling the rigging we are able to control our CanSat's flight and realize a targeted landing.

The task of our servo is to control the parachute: it has to be fast and accurate. It is controlled based on the GSP data and former controlling events by an Arduino Pro Mini. Although the servo's main task is controlling, it also have to fix the parachute, and be strong enough (its arms as well), to control the parachute.

D. Sensors' calibration

Most sensors were pre-calibrated by the manufacturer, although we had to introduce a couple of modifications in the calibration functions.

The spectrum analyzer was calibrated by us, because it has to measure a wide radio frequency band, but it only has one antenna with only one resonance frequency, so we had to compensate the values according to our calibration. The process was done in an anechoic-chamber with a log-periodic antenna.

E. Ground Station

The ground station of HunSat was based on a Raspberry Pi 3 single board computer running Linux operation system. A PCB containing the same RFM26W radio module (hardware radio) as the CanSat was connected to the Raspberry.

V. TECHNICAL DESCRIPTION - SOFTWARE

The software environment consists of three parts:

- The CanSat system has two subsystems: CanSat subsystem and Flight control subsystem, written in AVR C with extensions from Arduino
- The Ground Station system, written in standard C
- Client system, written mainly in JSCanSat

A. CanSat

When the microcontroller starts, it looks for external devices, and it initializes all the sensors. After the system initialization, it enters a never-ending loop. The software uses the GPS data input as a system clock: the module is configured to send data every second to the microcontroller. When this data is available, it gets processed, other data from the sensors get collected, converted, then sent to the ground in an encrypted packet which checks for bit errors. As we have a huge amount of data (especially with the spectrum data), and we do not use a big bandwidth for communication, nothing is processed on-board, everything is sent down to the Ground Station.

B. Ground Station

The software of the Ground Station is composed of multiple programs and scripts. Adjusted to the Raspberry-philosophy, there are different 'tools' written mostly in python (one tool for crc checking, another for decoding, etc.): each output data is piped to another tool's input. At every boot the Linux cron starts up our software to manage the ground activities.

A forward mode is implemented in the converter script: it simultaneously sends all data to Budapest, Hungary to the servers of Budapest University of Technology, which relays it to local followers of the competition. The jQuery-simplewebsocket equipped client is able to connect to this.

C. Flight Control

We attempt to land the device within a restricted neighborhood of a pre-selected ground position using the built-in GPS and the maneuvering capabilities of the parachute.

Selection of the position can be indicated to the device via a radio signal to the main PCB, which indicates the selection with pulling a pin down on the controlling Arduino. There is a vertical, round 'wall' defined, inside which the program controls the CanSat. An important challenge to be tackled is accurately modeling the speed and direction of the wind from GPS measurements alone, since wind influences the precision of turns and thus ultimately impacts the chances of successfully landing within the prescribed area. Calculations are made by the program to model the wind from the distribution of actual speeds in different directions, and from observing how these speeds diverge from the default coasting speed of the device.

D. Client

The flow of the client program is as follows: it waits for new data on the WebSocket (which is hosted on the Ground Station),

and if there is some, it appends it to the end of the rolling graph. We used a plotting library (ChartJS) to visualize all significant data in real-time. The page is autorefreshed when a packet arrives. Since the JavaScript is parallel, another thread will process the telecommanding of the CanSat.

There Ground Station itself can also host a webpage, which is easier to be used by us (it has all the necessary functions and more), but has a less responsive design.

VI. TECHNICAL DESCRIPTION - TESTING

Apart of our tests and/or calibrations are already mentioned. We would like to emphasize here two more tested areas: communication tests and tests related to the parachutes.

A. Communication

We tested the communication between the HunSat flight model and the ground station in real in-situ environment. The distance between our CanSat and Ground Station during the test was 1.25km. (1)

$$a_0 = 20 \lg \frac{4\pi d}{\lambda} = 87 \text{ dBm} \quad (1)$$

, where: d is the distance, λ is the wavelength ($\sim 70\text{cm}$).

The HunSat flight model transmits 16dBm radiated RF power level. The received signal level is $16 - 87 = -71 \text{ dBm}$ (not only calculated but measured data). In case of 50 kbit/s data rate with GMSK modulation, the used bandwidth is 75kHz. So the thermal noise level is: (2)

$$P_n = kTB = -125 \text{ dBm} \quad (2)$$

, where: k is the Boltzmann constant, T is the equivalent noise temperature, B is the bandwidth of the receiver.

The realized signal-to-noise ratio is (3)

$$\text{SNR} = \frac{P_s}{P_n} = -71 - (-125) = 54 \text{ dBm} \quad (3)$$

During the test, we put more than 43dB additional attenuation to the radio link, which means that the realized radio link can be 200 times higher: distance can be 250km is line-of-sight propagation.

B. Parachute

We tested our parachutes to ensure the required descent speed. The spherical parachutes had to be changed a little bit: we cut holes on them to make sure they can guarantee the stability. With the paraglider we had to work with its rigging.

We did our highest drop test from a gyrocopter next to Budapest, Hungary before the competition. It was the final test of our parachute and chassis. Both of them succeeded!

VII. SCIENTIFIC RESULTS

In this section our measurement data can be found. We use 'time' as an 'x' axis on many of the following graphs. In our log files, time starts at the point of turning on the CanSat, but on our graphs the time only starts 48 seconds before the rocket launch.

The launch point has been determined with the usage of the acceleration-time and height(pressure)-time graphs. The landing of the CanSat is approximately at 170 seconds on this scale.

A. Temperature

The measured temperature data is visualized on Fig. 5.

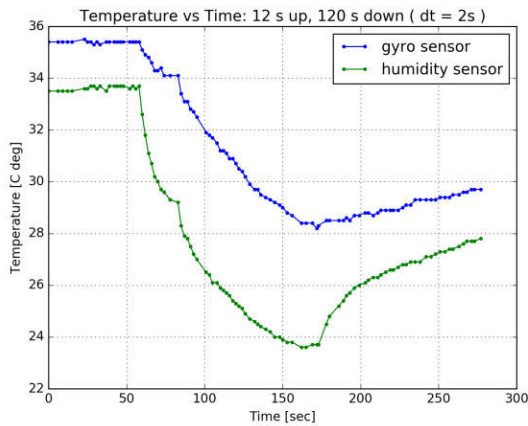


Fig. 5. The measured temperature data in time

Two curves are present on Fig. 5. One is from the temperature sensor of the acceleration & gyro sensor, the other is from the temperature sensor of the humidity sensor. The gyro sensor has a microcontroller built-in, which is needed for the calculations done by the chip itself. This microcontroller consumes electricity, thus it heats. This is the reason, why it shows us higher temperature with approximately 2°C at the beginning, and reacts slower to the change in temperature.

B. Pressure & height

Fig. 6. depicts the measured pressure data, and Fig. 7. visualizes the altitude data of our CanSat.

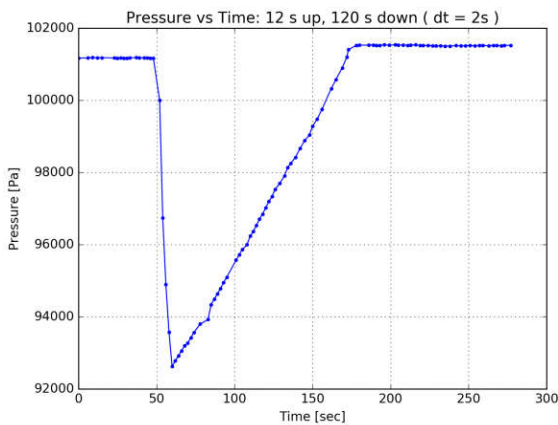


Fig. 6. The measured pressure data in time

We used the pressure data to determine the current altitude of the CanSat, because it is far more accurate, than the altitude data from the GPS. The launch point also can be determined with the help of pressure, thus height data.

These graphs are useful, important data can be determined without the usage of the acceleration diagram: The rocket accelerated between 49-51 seconds, just for 2 seconds - as it was expected. (The one-second sampling rate makes a big uncertainty.) After that its speed decreased, but it still climbed. The moment of the burst of the nosecone can also be determined: the CanSat sinks after that. This was around 840m of height.

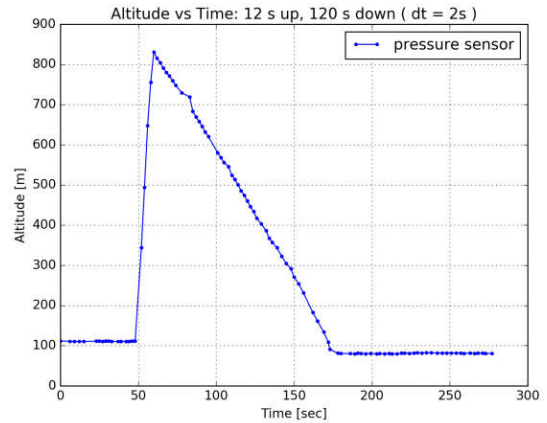


Fig. 7. The calculated altitude data

C. Acceleration & angular velocity

Fig. 8. And Fig. 9. shows the acceleration and angular velocity data.

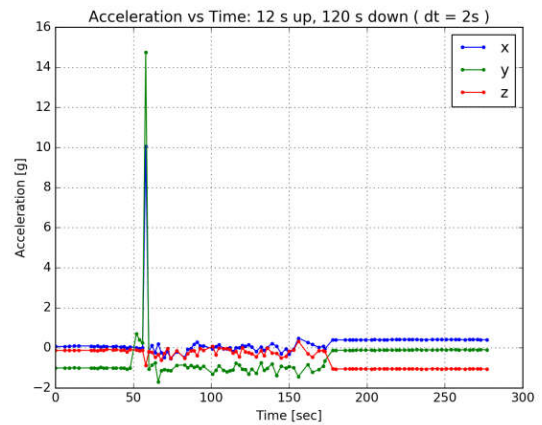


Fig. 8. The measured acceleration data in time

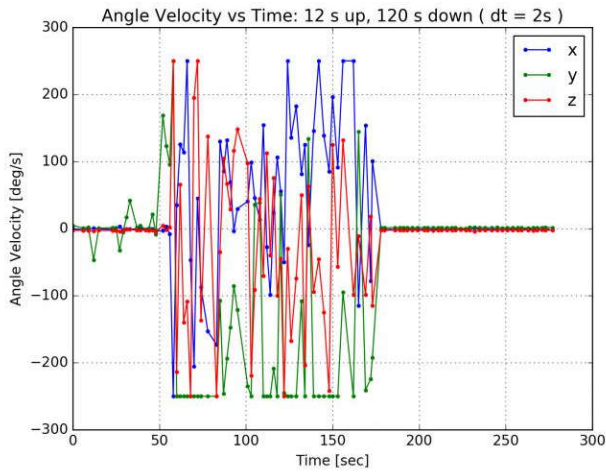


Fig. 9. The measured angular velocity data in time

According to Fig. 8. the CanSat accelerated for approximately two seconds, and around the highest point of its orbit, there is an acceleration pic: it was caused by the explosive detachment of the nosecone of the rocket.

It can be noticed that the data of the gyrosensor (Fig. 9.) had been cut: the CanSat spun around its axis very fast.

D. GPS data

We saved the data from the GPGGA and GPRMC GPS sentences. One important data is the horizontal speed of our CanSat, which is shown on Fig. 10.

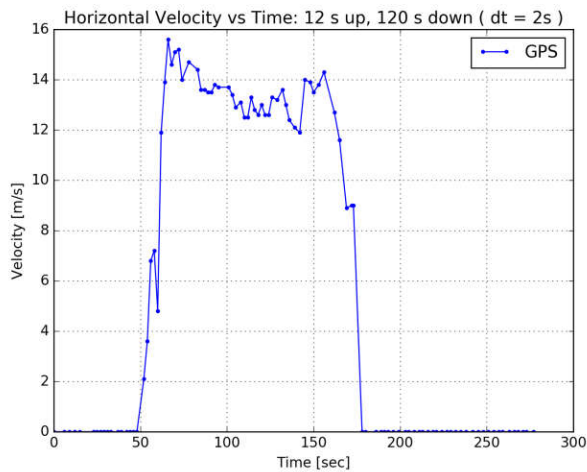


Fig. 10. The measured horizontal velocity data in time

Our CanSat at the Azores moved with more than 50km/h of speed according to Fig. 10. The weather is very windy thanks to the ocean climate.

For this reason it was very hard for the targeted landing system to control the turns of the CanSat. According to the software logs, the software functioned well, but the hardware, the CanSat itself couldn't turn, because of the big winds.

E. Spectrum analyzer

The spectrum analyzer data is depicted on Fig. 11.

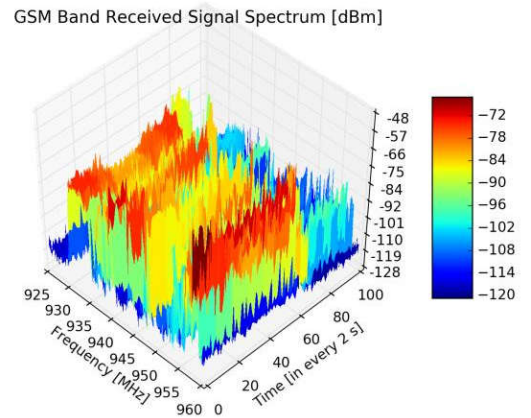


Fig. 11. The measured spectrum data in time

It could be hard to interpret 3D images, thus it is easier to use the 2D-projected visualization of this data depicted on Fig. 12.

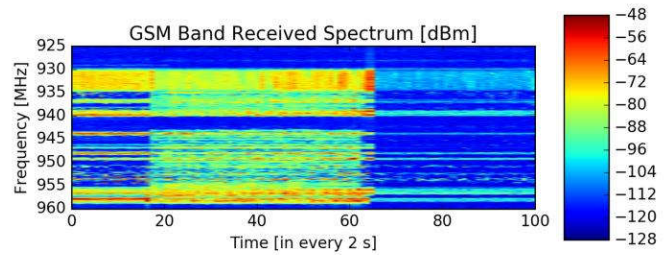


Fig. 12. Frequency vs. time graph colored with RSSI values

Our spectrum analyzer analyzed the GSM (more precisely the E-GSM-900) spectrum of the downlink (the signals coming from the base to the mobile phone).

On the 2D graph the horizontal stripes (parallel with the time axis) are different bands, channels used for different types of communication. The data in one vertical streak is from one scanning. The time scale is different here. Fluctuations can be seen during the whole descending (40-60s on this scale): stronger and weaker signals can be noticed. This is because of the characteristic of the base transceiver. We successfully measured that phone calls can also be realized where they are unnecessary.

REFERENCES

- [1] <http://www.esa.int/Education/CanSat/>
- [2] <http://kozmosz.space/>
- [3] <https://gnd.bme.hu/cansat/>
- [4] http://www.esa.int/Education/CanSat/Best_CanSat_final_reports_2018_Congratulations/

Educational Aspects of Developing a High Altitude Balloon Platform

Zsófia Bodó , Bence Dávid Góczán

Simonyi Karoly College for Advanced Studies

Budapest, Hungary

bodo.zsofia@simonyi.bme.hu, goczan.bence@simonyi.bme.hu

Abstract—Space industry struggles to find qualified engineers with hands-on experience in space-related technologies. Even though the higher education in Hungary has a broad spectrum for engineering students, it lacks aerospace or space engineering courses available in the country. This educational gap means a shortage of experienced employee and thus a high amount of personnel costs for the space companies. This paper focuses on the possibilities of enhancing and combining the higher educational studies with student-led projects aiming to teach skills and competencies that are necessary in the space and aerospace domain.

The UPRA Project (Universal Platform for Robotics and Aerospace) is a student project with an aim to develop a reliable, widely configurable, low maintenance, high altitude balloon platform for university research groups. The development team consists of computer science and electrical engineering students, who are members of the Simonyi Károly College for Advanced Studies at the Budapest University of Technology and Economics. Besides the scientific goals of the project- such as providing a frequent flying opportunity for university experiments to the stratosphere - the educational aim is to provide an easily accessible hands-on experience for university students with a high variety of tasks in a space related project's lifecycle. With the mentorship of the Hungarian space industry, the team develops most of its workproducts internally, from the project management processes, the electronics schematics, the launch and recovery procedure.

During the development phase, the students have the opportunity to learn system engineering skills, quality management in the space domain, embedded software engineering for flying modules and ground station development and management. Also, since the project is delivering flight opportunities to experiences from other universities and organizations, it provides system integration knowledge for the participants. Another important aspect of the space industry is the difficulty of testing. We can make several simulation, unit and hardware-in-the-loop testing but the field testing can only be done during the launch. One of the strengths of the project is a thorough retrospective section. After each launch and recovery sessions the team holds a series of meetings to collect the lessons they learned during the development, validation and launch.

During these events it is important that the team members learn important aspects about system engineering and effective project management. There are many possibilities for the project for further growing. A closer cooperation with the key industry players and the universities can hold several aspects for further enhancing the educational value.

Keywords—*high altitude balloon, remote sensing, earth observation, agriculture*

I. INTRODUCTION

Remote sensing provides crucial information in agricultural applications. Monitoring vegetation health and open water surfaces like inland-water or flooded areas could improve prognosis on crop yields and help planning actions in crop management.

Besides already available and widely used remote sensing platforms, balloons could provide frequent data coverage for a reasonable cost.

This paper covers the different skillsets and areas a student can learn while taking part in the research, development and validation activities.

II. PROJECT MANAGEMENT

Although the System Engineer overviews the technical work, there is more to the world than engineering. Students who would like to develop their soft-skills and project management skills also have the opportunity to benefit from the project. There is a lot of non-engineering work around a space project like organizing regular progress meetings, workshops, keeping track of the schedule and budgets, communicating with clients, suppliers and supervisors and supervising documentation and legal paperwork.

The development of the platform is organized similar to a typical space project. Students can gain experience in project management work-flow, learn how to use different tools. They can also improve their presentation and negotiating skills. Thanks to our industrial connections and alumni members students can acquire the know-hows from professionals.

Handling these tasks can be a valuable experience both engineering and non-engineering students and open different kind of opportunities to join the space industry.

III. REHAB BALLOON PLATFORM

ReHAB – Reusable High Altitude Balloon-platform is developed by the Universal Platform for Robotics and Aerospace (UPRA) Team of Simonyi Karoly College for Advanced Studies. The platform is developed and manufactured by students and designed to carry small science payload up to 30 km to the stratosphere.

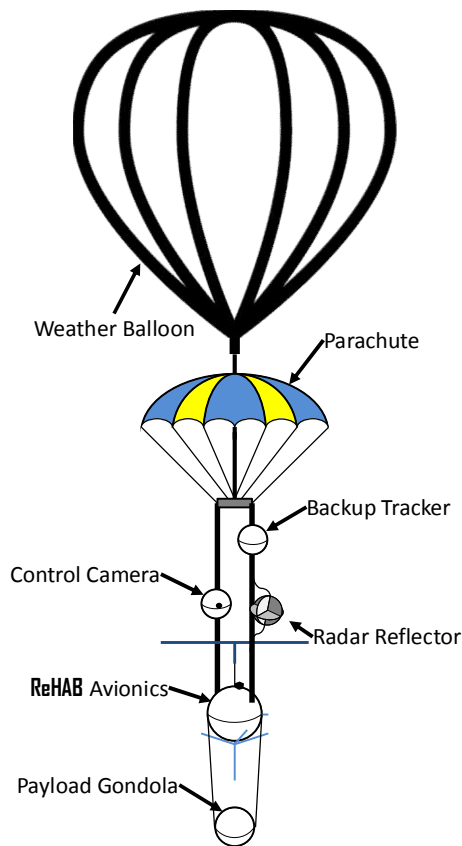


Fig. 1 ReHAB flight configuration

The goal of the UPRA Team is to support university research groups with affordable launch opportunities providing the platform, launch and recovery service and flight planning.

The avionics system of the platform provides two way radio communication, live tracking and data storage. It is also possible to monitor and control the science payload.

The platform is highly configurable to meet the mission demands. It is planned that a standardized payload gondola to be provided but also custom made payloads are acceptable. The flight configuration of the platform can be seen in Fig. 1.

IV. ON-BOARD COMPUTER (OBC)

While working on the On-Board Computer (OBC) students can learn how to design and develop microcontroller based, reliable embedded systems. Getting familiar with digital electronics, communication protocols and fault-tolerant software is a valuable experience for students planning their career in space industry.

Our flight computer is built around a system bus that connects the avionics subsystems and third party payloads.

The subsystems are developed with COTS components thus students have to learn how to test digital hardware and embedded software elements to validate the reliability of the system.



Fig. 2 On-Board Computer Flight Model

The current OBC (Fig. 2) has an Arduino compatible Atmega328p microcontroller with Arduino Bootloader. This provides the opportunity to develop the embedded software in the Arduino IDE and to use off the shelf Arduino boards during development. The compatibility with the Arduino environment provides a fast learning curve for students who just started their study in the fields of embedded electronics.

Further development of the On-Board Computer contains an upgrade to a more powerful ARM based microcontroller thus students on the project could be introduced a wide variety of controllers used in the industry.

V. POWER DISTRIBUTION SYSTEM (EPS)

Students can learn how to design analog circuits through the development of the power supply and environmental sensors of the flight computer. Designing a sufficient power supply for a balloon or a satellite takes preliminary calculations, knowledge in power distribution and power management. During the development process students gain experience in testing and fine-tuning analog circuitry, getting familiar with different type of power-sources and analog sensors.

The power distribution system is the backbone of every spacecraft, possessing knowledge in analog circuit design is a great asset for students planning their future in space industry.

VI. COMMUNICATION MODULE

Communication with the balloon is vital. Students who take part in the development of the radio communication module can learn the principles of digital wireless data-transfer and how to design high-frequency circuitry.

Our communication subsystem provides bidirectional radio communication between the balloon and the ground station to provide live telemetry data and to receive control commands. The goal is to provide a wireless link for third party payloads to download scientific data during flight.

The current COM module (Fig. 3) is using Hope RF off the shelf radio transceiver modules and Arduino compatible microcontrollers.

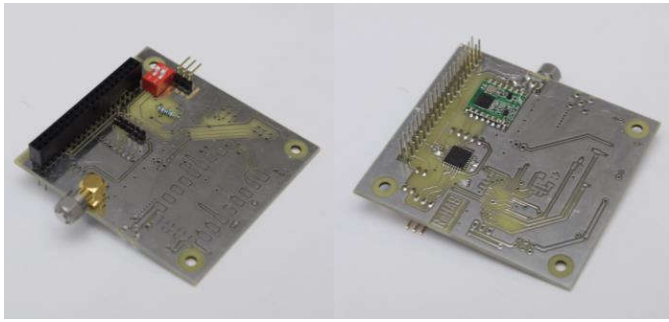


Fig. 3 UHF Communication Module Flight Model

A further development on the Communication Module includes the improvement of the RF circuitry by designing better filters and amplifiers. It is also planned to introduce hot redundancy by adding a beacon transmitter to the design. These improvements will require to update the microcontroller and will require embedded and RF engineers to work together.

VII. GROUND STATION (GND)

Beside the on-board communication subsystem, development of a sufficient ground station (GS) is also in progress. Installing an antenna rotator, planning tracking methods and developing the ground station user interface give a chance to join the project not only for students who interested in RF development but also for software developers and control engineers.

The current ground station hardware is based on the same transceiver used on the balloon. This provides great compatibility with the COM module but low configurability for later missions. As further development on the ground station hardware experiments have been conducted with software defined radio (SDR) based solutions. To improve ground station performance installation of an autonomous antenna rotator is in progress on the roof of Schönherz Dormitory which is the headquarters of the balloon development.

The ground station software is a web based application with Python backend and JavaScript frontend. The GS software is designed to be easily configured, handle different radio modems and has the ability to display different datasets on different workstations.

Further development on the GS software contains the plan to handle different radio stations simultaneously and to integrate flight path predictor to provide live simulations based on telemetry and meteorological data.

VIII. BACKUP

Designing fault-tolerant hardware is one of the main principles in space engineering. Achieving reliability through testing and validating is not always enough. Vital subsystems usually have a redundant pair or a backup system.

In high altitude ballooning recovering the payload after landing is the key objective. Considering this, the payload train contains an independent Backup GPS Tracker and a redundant radio downlink to provide valid position information all time.

Students involved in the project have to learn how to make their subsystem reliable either through fault-analysis or implementation of redundant pairs. Acquire this kind of point of view in hardware development can be advantageous in the space industry.

IX. STRUCTURE(STRU)

Electronics cannot fly without sufficient mechanical structure. Mechanical parts of a high altitude platform have to withstand vibration, large temperature range and the impact of landing. Students involved in the development of the structure can gain experience in Computer Aided Design, mechanical and thermal simulations, they can learn how to prepare their design for production and how to plan the mechanical integration process of the capsule. It is also important to learn the communication between students from different engineering fields.

Currently the avionics gondola is a spherical capsule with an internal frame to support the electronic components. While this version of the gondola is already in use the design of an updated avionics module is in progress. The new version will be fit in the 1 unit CubeSat form factor and will be using 3D printed frame elements (Fig. 4). This will help students to gain experience in working with space industry standards and prepare them for small satellite missions.

Our workshop provides 3D printing and CNC milling capability with a complete mechanical workshop. This way students gain hands-on experience in manufacturing and payload integration.

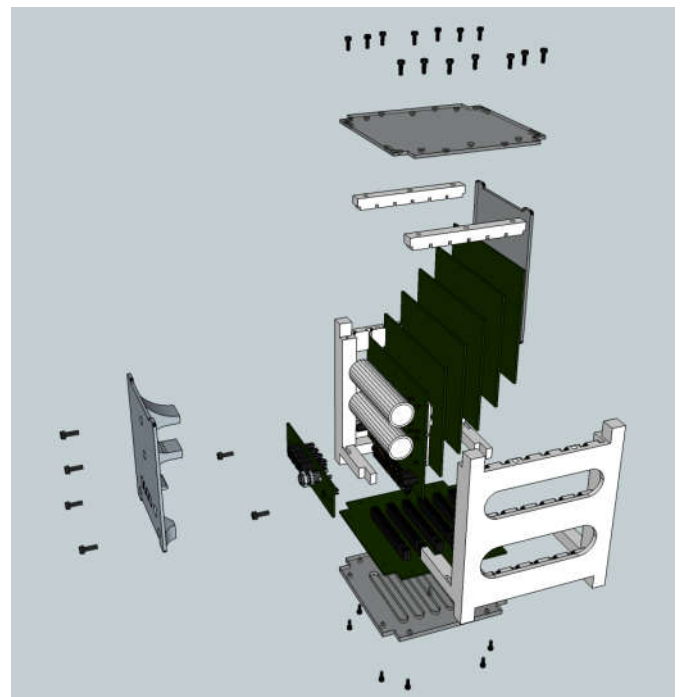


Fig. 4 Exploded CAD drawing of the CubeSat like avionics module

X. INSULATION

During a high altitude flight the platform has to withstand low temperatures down to -60°C . In the flight computer COTS components are used which are usually graded to a minimum of -40°C . For providing a proper operational environment inside the capsule, insulation is needed.

Students involved in the design of the insulation can learn thermal calculations and simulations. They can rely on previous flight and test data to develop the most sufficient insulation for the payload. Validation of the system for low temperature environment involves testing in thermal chamber which provides a valuable hands-on experience for students.

Our workshop provides a small thermal chamber where students can practice the process thermal testing and learn how to operate such equipment.

XI. FLIGHT PLANNING

Flying a high altitude balloon without active control is based on predictions rather than precise planning of the flight path. Although the goal is to eliminate the luck factor. Students involved in flight planning can learn how to use the available balloon flight predictors and how to develop new ones. They get familiar with the calculations, weather data and the capabilities of the platform to specify the flight parameters most fit for the mission goals.

Flight planning includes the specification of the target altitude, prediction of the possible landing sight, determine a flight window and organize the recovery. During the flight Mission Control and the Recovery Team relies on these information and organize their work accordingly.

A. Launch event

Launch events are usually open for the public where observers can follow the work of the launch team on location.

The launch team follows a checklist to prepare the launch site and equipment, filling the balloon and start up the payload train (Fig. 5). Being part of the launch team requires the ability of on-the-spot problem solving and knowledge on operating both the payload train and launch equipment.

The launch team is in live contact with the ground station personnel to ensure the stable communication between the payload and the radio station. The launch itself is approved by the flight director according to information from the launch team and the ground station personnel.

B. Recovery

Recovery of the payload is organized according to flight predictions and live balloon telemetry. The recovery team departs soon after the launch to the predetermined landing site. Their route is occasionally updated according to live telemetry data and on the fly simulations.

During the chase the recovery team and mission control is in contact to exchange information. Mission control has the ability to track not only the balloon but also the position of the recovery team.



Fig. 5 Launch preparations

Recovery team is formed by skilled drivers and hikers with good navigation skills. They usually have experience in HAM radio ‘fox-hunting’ and climbing too. At least one recovery team member has to have knowledge on operating the payload and avionics to properly shut down the recovered payload train.

It is the responsibility of the recovery team to document the landing site by taking photos and tracking their path. The recovered modules are not opened by any means by the recovery team. The payload train is transferred to the headquarters and modules are opened in a controlled environment.

XII. SUMMARY

Projects with hands-on experience are great addition to academic studies and help students to gain knowledge and further their horizon in their field of studies.

Working with high altitude balloons is a great entry to space related projects and gives the opportunity for students to gain the skillset needed for the space industry.

Our experience is that students who participated in the project had positive effects both on their academic progress and later on their professional carrier.

REFERENCES

- [1] Shane L. Larson et. al. - The first frontier: High altitude ballooning as a platform for student research experiences in science and engineering
- [2] [2] Jeremy Straub et. al. - A Design for Inspiring Students with Near-Space Exploration